2018

Functionalization and Characterization of Chemical Vapor Deposited Graphene Sheets Towards Application in Chemical Vapor Sensing

Nicholas Alexander Engel
Wright State University

FUNCTIONALIZATION AND CHARACTERIZATION OF CHEMICAL VAPOR DEPOSITED GRAPHENE SHEETS TOWARDS APPLICATION IN CHEMICAL VAPOR SENSING

A thesis submitted in partial fulfillment of the
requirements for the degree of
Master of Science in Materials Science and Engineering

By

NICHOLAS ALEXANDER ENGEL
B.S.M.S.E. Wright State University, 2015

2018
Wright State University

WRIGHT STATE UNIVERSITY

GRADUATE SCHOOL

July 25, 2018

I HEREBY RECOMMEND THAT THE THESIS PREPARED UNDER MY SUPERVISION BY Nicholas Alexander Engel ENTITLED Functionalization and Characterization of Chemical Vapor Deposited Graphene Sheets Towards Application in Chemical Vapor Sensing BE ACCEPTED IN PARTIAL FULFILLMENT OF THE REQUIREMENTS FOR THE DEGREE OF Master of Science in Materials Science and Engineering.

_____

Hong Huang, Ph.D.
Thesis Director

_____

Joseph C. Slater, Ph.D., P.E.
Chair, Department of Mechanical and Materials Engineering

Committee on Final Examination

_____

Hong Huang, Ph.D.

_____

Yan Zhuang, Ph.D.

_____

Shin Mou, Ph.D.

_____

Barry Milligan, Ph.D.
Interim Dean of the Graduate School

ABSTRACT

Engel, Nicholas Alexander. M.S.M.S.E. Department of Mechanical and Materials Engineering, Wright State University, 2018. Functionalization and Characterization of Chemical Vapor Deposited Graphene Sheets Towards Application in Chemical Vapor Sensing.

Chemical/biological sensors serve many purposes in protecting machinery, the environment, and human life/wellness. Graphene, a two-dimensional (2-D) material made up of carbon atoms in a honeycomb-like lattice, is promising for applications to chemical/biological sensing due to its unique properties. Functionalization of graphene by surface decorating with nanoparticles and increasing interior adsorption sites can tailor its catalytic activity and electrical properties, and hence, important for detecting and distinguishing trace hazardous gases.

This research introduces two different approaches to functionalize graphene towards enhanced sensitivity and selectivity of graphene-based sensors. The morphologies, structures, and electrical properties of the functionalized graphene are systematically characterized. The first approach is to decorate graphene surface with gold and platinum nanoparticles using air-spraying technique. It is determined that the sheet resistance nearly linearly increased as the nanoparticle concentration on graphene increased. Both metals resulted in the increase in sheet resistance due to reduction of charge carriers. The resulted difference in electrical properties can be utilized to tune

graphene sensing capabilities. The second approach is to modify graphene via oxygen doping or partial oxidation under oxygen plasma or thermal treatment. Evolution of structure and changes of electrical properties at microwave frequencies were qualitatively analyzed. The width of electrically inactive layer near micro-pattered graphene resulting from oxygen plasma etching is determined with the help Raman spectroscopy and scanning microwave microscopy (SMM.) The effects of annealing temperature on structural and electrical parameters are also analyzed. It is found that graphene annealed at and above 350°C shows distinct structural and electrical changes, which is not suitable for sensor recovery. These two insightful observations will provide critical guidance for processing optimization and recovery control of graphene-based sensors.

TABLE OF CONTENTS

LIST OF FIGURES

LIST OF TABLES

1 Introduction

Chemical vapor sensors serve many purposes in protecting machinery, the environment, and human life/wellness. Monitoring dangerous gases is important for military personnel as well as the public. Ideally, a sensor will be able to identify and quantify the target species in real-time, be easily interpreted, and be portable. The recent use of chemical warfare agents (CWA) by rogue nations against civilians emphasizes serious implications of inadequate sensing capabilities of current sensing technologies. Sensing of ammonia (although not as deadly as CWA) for environmental and human health using sensor designs also encounters the issues listed above.

1.1 Danger of Chemicals and Demands for Chemical Sensors

1.1.1 Ammonia

Ammonia (NH_3) is a chemical compound found both in nature and produced on an industrial scale. In high concentrations, ammonia can be poisonous, causing irritation of the skin, respiratory system, eyes, and throat [1]. Due to the ease of availability and the possibility of use in a chemical attack, ammonia is considered a toxic industrial compound (TIC) [2].Though it is produced in low concentrations by the body via metabolism of nucleic acids, ammonia is removed from the body by means of sweat and urine [3]. During extreme exercise, ammonia tends to build up due to processes explained in [4], thus, high levels of ammonia may be an indicator of exhaustion and fatigue. By

sensing the amount of ammonia in sweat, it may be possible to determine an individual's fatigue level. If the individual's fatigue level is above some pre-determined level, that individual may not be able to work at peak performance in terms of physical exertion and mental capacities. Monitoring this statistic over time is expected to give the highest, most reliable performance out of each person. This type of monitoring can be most important to individuals in high-stress environments such as pilots.

Ammonia is used in the production of fertilizers such as ammonium sulfate and ammonium nitrate, when it reacts with sulfuric acid and nitric acid respectively. However, these two ammonium compounds have a more sinister use as the oxidizer in improvised explosive devices (IEDs) [5]. When combined with high surface area (and thus high surface energy) metal powder, ammonium nitrate (AN) reacts explosively, oxidizing the metal powder, potentially having 75% of the explosive power as trinitrotoluene a.k.a. TNT [6]. Another implementation of ammonium nitrate in IEDs is when mixed with fuel oil, together called ammonium nitrate fuel oil (ANFO) [5]. According to [7], if ammonium nitrate is with more than 0.2 percent combustible substance, it is considered by the Department of Transportation to be an explosive. Ammonia is one of the decomposition products of AN allowing the detection of dangerous IEDs by means of sensing the ammonia given off by the oxidizer [7]. Being able to detect the IED from a distance is important to the safety of civilians and/or military personnel.

1.1.2 Chemical Warfare Agents

Chemical warfare has been used since 10,000 B.C. In ancient times, many of the chemicals were used to incapacitate or drive-out opposing forces with smell or irritants. Poison was added to arrows to increase mortality rates from a wound. Sulfurous smoke burnt from coal, brimstone, and pitch was used to besiege cities in ancient Greece driving away the inhabitants [8]. The Chemist's War (World War I) marks a shift toward the wide-spread use of modern chemical weapons on the battlefield. Chemicals that were used include elemental chlorine, hydrogen cyanide (HCN), cyanogen chloride (U.S. designates cyanogen chloride as CK), carbonyl chloride (designated CG), and mustard agent (HS and HD in a purified form). An estimated 1.2 million soldiers were wounded from gas and approximately 91,000 died [8]. After World War I, chemical warfare was used world-wide: Spain used mustard on the Riffians; Italy used mustard, chlorine, and tear gas on modern-day Ethiopia; Japan used mustard, carbonyl chloride, tear gas, and others on the Chinese; and the U.S.S.R. used chemical weapons to quell a peasant revolt [8], [9].

G-series chemical agents represent a family of nerve agents developed after World War I. A compound called Trilon-83, now known as Tabun or "GA" under the U.S. convention, is the first known lethal nerve agent. A single drop of this colorless, slightly fruity smelling liquid was enough to cause asthmatic behavior and constriction of the pupils which made working under artificial light impossible for several days [8], [9]. Further testing would prove Tabun to be toxic to warm blooded animals (including humans) and lethal in 20 minutes or less [8].

The second nerve agent is Sarin (GB) which is both colorless and odorless, making the detection of the toxic nerve agent impossible to human senses until the symptoms arise. Sarin liquid is the most volatile of the G-series nerve agents evaporating from a sandy surface in approximately two hours even at 10°C [10]. The volatility allows for two forms of exposure, inhalation and penetration of the skin, although the effects of Sarin exposure via skin are diminished dramatically [11]. According to animal testing results, Sarin is about ten-times more effective than Tabun, though the two are chemically similar [8]. The symptoms of Sarin exposure are caused by acetylcholine build-up and cholinergic toxicity. These symptoms include excessive tear production, sweating, salivation, vomiting, constriction of the pupil (as mentioned with Tabun poisoning), rhinorrhea, seizures, paralysis, changes in heartbeat, and difficulty breathing [12], [13]. These symptoms are the likely result of low-dose Sarin attack, with the upper-limit obviously being death, typically by asphyxiation. Threshold doses are summarized in Table 1.

One of the major concerns with Sarin is how easily and cheaply it can be made. Though nerve agents are the deadliest chemicals known to man, many of the precursors to produce them are common chemicals which, when purchased in small quantities, would not trigger any attention due to their use in fertilizers and pesticides [12]. There is no specialty equipment needed for production, making financial tracking of nerve agent production more difficult to detect. There are also statements which argue a standard chemical production facility could shift from producing fertilizer to large-scale quantities of nerve agent in weeks to days [12], [14]. This makes Sarin a prime candidate for rouge nations and/or terrorist organizations to implement [15].

Table 1: Threshold doses of Sarin

Threshold	Dose of Vapor Exposure		Source	
LCt_{50}	100 mg min m^{-3} (~17.5 ppm min)*	60 mg min m^{-3} (10.5 ppm min)**	[16]	[11]
No Death	10 mg min m^{-3} (~1.7 ppm min)		[16]	
NNM	4 mg min m^{-3} (~700 ppb min)		[16]	
ECt_{50} (miosis)	2-4 mg min m^{-3} (~350-700 ppb min)		[16]	
NOAEL	0.5 mg min m^{-3} (~43.6 ppb min)		[16]	
MSC for 1 h exposure	0.001 mg m^{-3} (~0.17 ppb)***		[16]	
MSC for 8 h exposure	0.0003 mg m^{-3} (~0.02 ppb)***		[16]	
IDLH	0.2mg m^{-3} (~34.9 ppb)	0.1 mg m^{-3} (17.5 ppb)	[16]	[13]

LCt_{50} = dose which is lethal to 50% of a population, NNM = no neuromuscular effect, ECt_{50} = dose which causes a particular effect on 50% of a population, NOAEL = no observable adverse effect level, MSC = maximum safe concentration, IDLH = immediately dangerous to life and health

*Reports as low as 35 mg min m^{-3} have been proposed [17]

**estimated

***According to [16], there is a safety factor of 0.1 for the specified time indicating that one tenth of the dose shown is the "acceptable" limit.

While there do exist methods of removing nerve agents from the body, many are pseudo-reactive to an attack [15]. One of these methods includes using a bio-scavenger to breakdown the agent prior to influencing the individual. In order for this approach to work, the bio-scavenger must have a long blood half-life, be inactive in the absence of the nerve agent, and be present at (or immediately after) a chemical attack. The latter criterion can be a problem if the population was not prepared for an attack. At very low concentrations, it is unlikely that the attack would be detected prior to the symptoms of exposure. Gundavarapu et al. have observed that mortality upon high-dose Sarin

exposure can be reduced using epinephrine due to the drug's ability to dilate the bronchial muscles, mitigating the constriction caused by the nerve agent [12].

This emphasizes the importance of quickly detecting a chemical attack: to save the lives of those affected by the attack and to have more time to implement the procedures required to do so. Apart from detecting Sarin prior to an attack, it may also be useful to know after an attack whether Sarin had been used. This enables nations to help regulate other nations and keep them accountable to any chemical weapons treaty that was agreed to. A common way to determine if a population has been exposed to GB is to measure the concentration of isopropyl methylphosphonic acid (IMPA) in bodily fluids. IMPA is a metabolic byproduct of Sarin which is unique to Sarin (when compared to other nerve agents which have their own unique metabolites) as the body breaks down the toxin [18]. Highly sensitive sensors could be used to support the IMPA results.

1.2 Representative Sensing Materials Used in Chemical Vapor Sensors

Chemical sensors are, in general, made up of two main components: a sensing material (acting as a transducer) and a detector. The sensing material is specifically chosen such that at least one physical (measurable) property changes in the presence of a target species. A transducer is a component that converts a measurable physical property into a detectable signal. The detector is able to measure and output the signal given by the transducer. This section will be limited to chemi-resistive sensors which use a charge transfer from the target gas to the sensing material to control electrical resistance of the sensing material. It is important to note that other styles and configurations of sensors

exist with varying sensing mechanisms based on optical properties, mass of the target gas, etc.

Figure 1 shows schematically what a chemi-resistive sensor looks like with two different sensing materials, namely carbon nanotubes and graphene. The outermost pads inscribed “Au” are the electrical contacts where probes can be placed for measurement. The detector in this case is the ammeter shown as a circle with and inscribed “A” on the wire connecting the two electrical contacts. In this particular detector schematic, there is a constant, direct current voltage source used to drive the current in the system. The current change (due to change in electrical resistance of the sensing material) is the detectable parameter. Molecules of gas (represented by the larger red sphere intersected with the smaller yellow spheres) are responsible for this change in current (resistance).

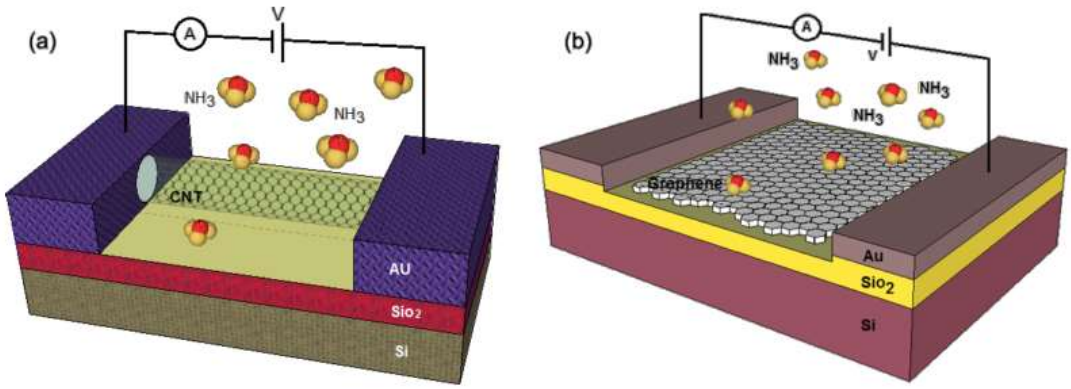

Figure 1: Schematic of basic chemi-resistors based on CNT (a) and graphene (b) [19]

Sensing materials used for detection of vapor include, but are not limited to: metal-oxides, conductive polymers, and carbon nanotubes (CNTs). Typically, sensors must be non-insulating in order for the transduction mechanism to be measured as most measurement and displays require electronic signal, save color-changing indicators. In

principle, any adsorbed gas will either add or remove (donate or accept) electrons from the sensing material, resulting in a change of electrical behavior due to a change in the band structure of the sensing materials [20]. Assuming that the rate of adsorption is proportional to the concentration of the target gas, a sensor is able to quantitatively determine the presence of the gas. This assumption is true for any sensor.

Examples of these sensing materials are described throughout this section. The sensing vapor is limited to ammonia, nerve agents, and nerve agent simulants. As stated to this point, Sarin is very dangerous, even in low concentrations. Therefore, for early stages of sensing research, a simulant is used. Dimethyl methylphosphonate (DMMP) is an organophosphate which is typically used to simulate Sarin [21].

1.2.1 Metal-Oxide Sensors

Metal-oxide semiconducting sensors work by interactions of the gas species with the grains (bulk-conduction), electrode-oxide interface (metal/oxide junction controlled), and/or chemisorption at the surface (intergranular controlled) [22]. Typically, one of these mechanisms will dominate, leading to measurable changes in the material properties. Bulk conduction is controlled by the oxygen partial pressure and the temperature of the oxide, as well as the partial pressure of the gas species [22]. Junction controlled ceramic sensors rely on voltage changes caused by the adsorption of a gas at the electrode-oxide interface represented as a diode barrier height. Surface conductive sensors use the effects of chemisorption to locally alter the carrier concentration of the material resulting in conductivity changes for varying concentrations of adsorbed gas [22].

For both bulk-conduction and intergranular controlled sensors, temperatures must be high enough for the ceramic to become conductive [22]. Temperatures to cause conduction in ceramics is often in the hundreds of degrees Celsius rendering the device of no use in wearable and room temperature applications. Consistent temperature is required due to the temperature dependence of the conductivity of the sensing material. In the case of surface conduction, the temperatures must remain low enough that gas can adsorb to the surface. Upon saturation, the devices must be heated at high temperatures to desorb or oxidize the gases to "regenerate" the device for a reusable design. This is both time consuming and requires significant energy consumption [23].

Silva et. al. developed an ammonia sensor based on a ZnO sensing material. The device was able to detect ammonia at high concentrations through a resistance measurement [5]. Upon increased ammonia concentration, the resistance changed proportionally. This demonstrates the ability for ZnO to be a sensing material, capable of quantitatively detecting ammonia in ideal conditions. However, when placed in a realistic gas solution containing ammonia, CO_2 and air, the response of the CO_2 was similar to that of ammonia implying the selectivity toward ammonia was low, as is stated for general metal-oxide sensors. The authors suggest adding a CO_2 filter to improve selectivity, increasing the complexity of the system [5].

Tin oxide can also be used as a sensing material for ammonia, however, even with a more sensitive polypyrrole (PPy) surface, the detection is limited to concentrations above 1ppm [23]. Apart from relatively low sensitivity, the amount of time that the gas is present, but not sensed, is relatively high, making real-time measurements difficult [23].

1.2.2 Conducting Polymers

For polymers to conduct, a chain of carbon atoms must have a conjugated (alternating) -single-double-single- bond scheme. This allow the electrons to transfer in π-π bonds [24]. The geometry of the polymer is also important to the overall sensing capabilities as higher surface area-to-volume ratios (SAV) increase the sensitivity of the material [20]. In general, this is valid since a higher surface area indicates a larger active surface for the target gas to be adsorbed. The higher the sensing area, the more likely gas molecules will be adsorbed and thus, the more likely the sensor will respond.

Polymer systems that have been used include polyaniline and polypyrrole. Polyaniline has been shown to be sensitive (and selective) to ammonia with a lower detection limit reported to be ~1ppm when the material was conformed into nanowires which have a relatively high SAV compared to that of a polyaniline thin film [20]. Organic sensors tend to be useful due to the ability to functionalize, that is change the characteristics of a base material by adding functional groups to the material. This type of functionalization, when performed properly, allows a preferential selectivity of particular species specified by size, shape, polarity, and/or chemical reactivity [23].

Conducting polymers have been fabricated into nanotubes to increase the sensing area of the polymer. Effectively, nanotubes are a one-dimensional (1-D) structure, allowing for high charge transport in the longitudinal direction of the nanotube [21]. Hydroxylated poly(3,4-thylenedioxythiophene) was fabricated into nanotubes (HPNT). The nanotubes were decorated with other nanostructures, namely “nanonodules” and “nanorods” to increase the SAV in an effort to increase the sensitivity of the material. The addition of nanorods to the surface of the polymer nanotubes increases the specific

surface area by a factor of two from 31 m^2g^{-1} for smooth walled nanotubes to 62 m^2g^{-1} for nanorod decorated nanotubes [21]. SEM and TEM images of the nanotubes combined with the nanonodules and nanorods are shown in Figure 2. The group also took advantage of the hydroxyl groups present in the polymer. These functional groups act to improve charge transfer from the target gas to the sensor, increasing sensitivity and, likely, response time. To have controls, the group used non-decorated and decorated nanotubes in both random and aligned arrangements to show the effects of each condition. Figure 3 shows the results of the experimentation. (Explanation of the response vs. time plots are available in Appendix A.) As expected, the higher surface area (decorated) nanotubes outperformed the non-decorated nanotubes (Figure 3b) and the aligned nanotubes outperformed the randomly oriented nanotubes (Figure 3d). The decoration geometry also played a part in the sensing capability. The response was higher with the nanorod decoration than the nanomodule (Figure 3b and e). With the nanorod decorated nanotubes, the material could sense DMMP at 10 ppt (<1% response.) This system also exhibits a recovery capability which is highly desirable. The system was able to remove the adsorbed gas in less than 25 s. The decoration using nanorods increased the sensitivity of the HPNT around 500 fold.

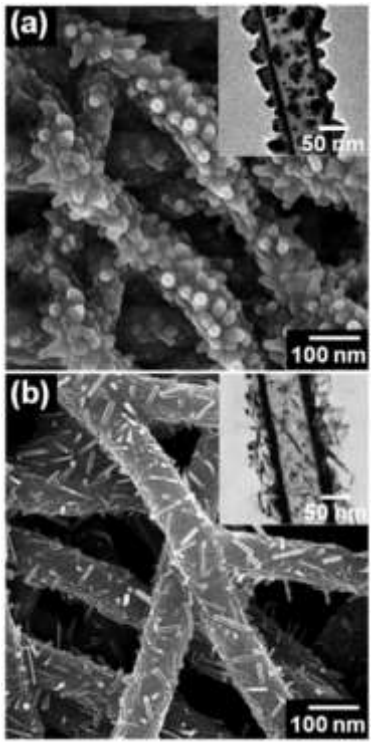

Figure 2: SEM (TEM inset) images of HPNT with nanonodules (a) and nanorods (b) attached to the surface. [21]

The same group also took advantage of the hydroxyl groups present in the polymer. These functional groups act to improve charge transfer from the target gas to the sensor, increasing sensitivity and, likely, response time. To have controls, the group used non-decorated and decorated nanotubes in both random and aligned arrangements to show the effects of each condition. Figure 3 shows the results of the experimentation. The higher surface area (decorated) nanotubes outperformed the non-decorated nanotubes (Figure 3b) and the aligned nanotubes outperformed the randomly oriented nanotubes (Figure 3d). The decoration geometry also played a part in the sensing capability. The response was higher with the nanorod decoration than the nanomodule (Figure 3b and 3e). With the nanorod decorated nanotubes, the material could sense DMMP at 10 ppt (<1% response). This system also exhibits a recovery capability which is highly

desirable. The system was able to remove the adsorbed gas in less than 25 s. The decoration using nanorods increased the sensitivity of the HPNT around 500 fold.

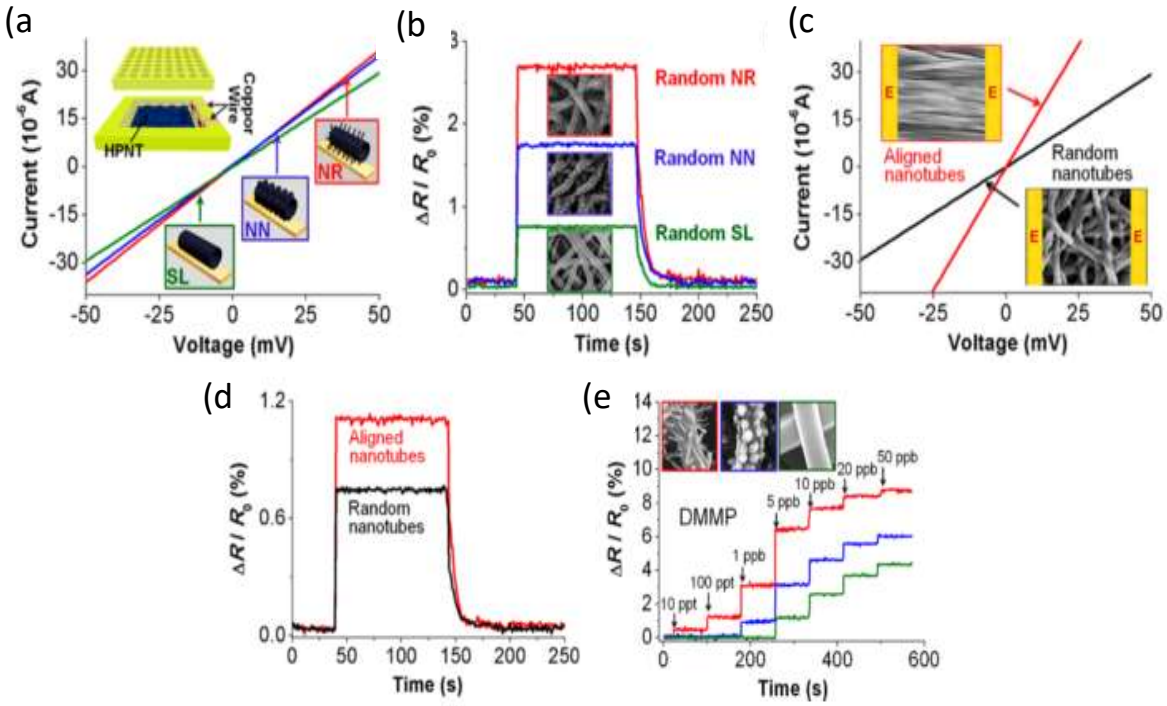

Figure 3: Sensing results of HPNT with (NN and NR)/without decoration (SL) and aligned or random nanotube orientation [21].

With regard to typical conducting polymer sensors, desorption of the target gas occurs rather slowly causing the devices to interact irreversibly with the gas. Over time, the reliability of the measurements decrease due to this interaction making the polymer sensor unusable after a certain amount of time [23]. While the gas is adsorbed to the surface of the polymer, there is a swelling effect due to interaction of the adsorbed gas that changes the resistivity of the material which can be difficult to predict, and therefore is often omitted from the measurement considerations [23].

1.2.3 Carbon Nanotubes

There are two categories of CNTs, the single-walled and multi-walled (SWCNT and MWCNT respectively.) This refers to the number of concentric, atomically-thin tubes present in each structure. CNTs are typically referred to as a one-dimensional (1-D) form of carbon when the length-to-diameter ratio is high. Both categories of CNT have the conjugated-polymer style bond structure allowing for electronic conduction. For this reason, the sensing mechanisms are similar to those of conducting polymers.

The advantages of the CNT to the conducting polymer is the higher total amount of surface, functionalizability, and higher conductivity. According to calculations in [25], MWNT with less than 20 walls are expected to have specific surface areas of greater than 100 m^2g^{-1}. This value is nearly twice that presented in [21], where the authors created decorated HPNTs. The higher total surface area allows for more sensing surface and higher probability of sensing dilute vapor. Functionalizability allows for tailoring the sensing mechanisms to specific compounds. Higher conductivity allows for higher sensitivity across all concentrations.

1.2.4 Graphene

Graphene is an allotrope of carbon containing, in its perfect state, only sp^2 hybridized orbitals [26]. The carbon atoms form a lattice on a plane with a repeat unit containing two inequivalent atoms (in terms of lattice symmetry.) When the two-dimensional (2-D) lattice is extended, a honeycomb pattern of atoms emerges. Figure 4 shows how graphene (light blue) can be used to generate buckyballs (green) with zero-dimension (0-D), CNTs in 1-D (purple), and layered to form three-dimensional (3-D)

graphite (dark blue) [27]. In fact, some use graphene to model CNTs meaning that the sensing mechanism is, again, similar to conducting polymers and CNTs.

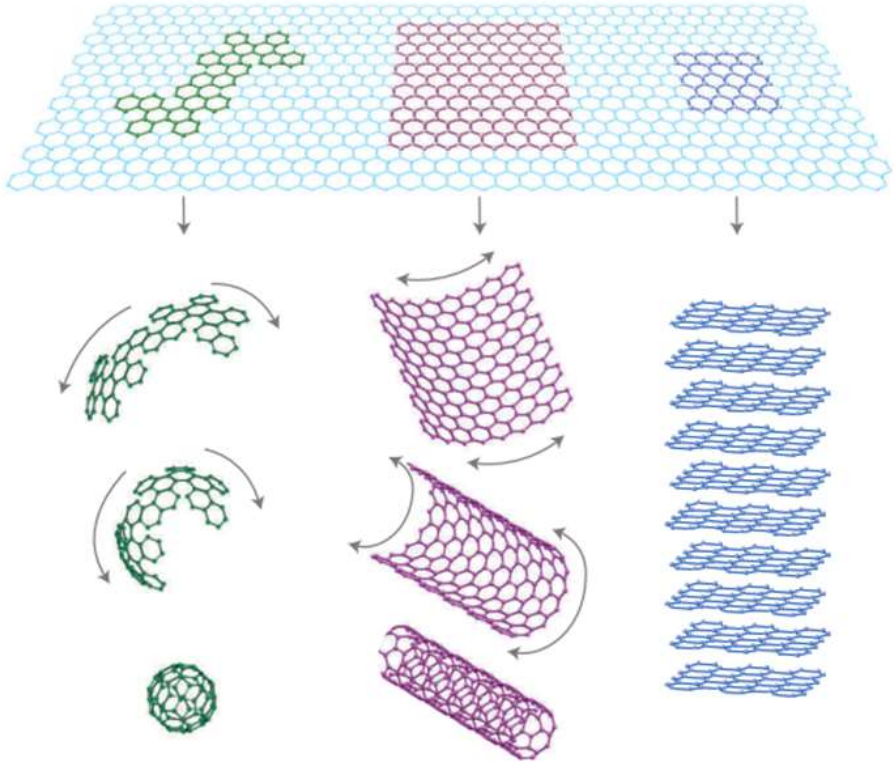

Figure 4: Graphene as building-block of other dimensionalities[27]

Graphene is distinguished by the number of layers present. With additional number of layers, the properties begin to converge toward bulk graphite. Single layer graphene (SLG) is notably different from bi-layer graphene (BLG) and few layer graphene (FLG) which is commonly understood to be from 3-10 layers (beyond 10 layers, the film has properties similar to graphite thin films [27].) Orbitals form two types of bonds: σ-bonds and π-bonds. The σ-bond is considered stronger, with larger volume of orbital overlap as two orbitals overlap (in graphene two sp^2) on the virtual lines which

connect adjacent atoms. The weaker π-bond is formed by non-hybridized *p* orbitals which are normal to the plane of atoms. These π-bonds are the key to graphene's electronic properties [28].

The method of obtaining graphene remains of high importance to the structural quality and therefore the properties of the material. Mechanical exfoliation of graphite was the first method to obtain graphene. This method produces highly oriented, high-quality graphene, however, the shape and size of graphene that is produced is on the order of microns and has an unpredictable shape. This method is useful to examine high-quality graphene in small scale experiments; however, the process is not easily scalable. Graphene can also be produced by thermal decomposition of carbon-containing compounds such-as SiC. According to [26], the thermal decomposition of SiC creates either few layers of graphene with low mobility carriers or several layers with higher mobility carriers. Depending on the use of graphene, this method can be useful.

Chemical vapor deposition (CVD) is a scalable method for the production of graphene. Typically, hydrocarbons like methanol or ethanol are decomposed into carbon and hydrogen gas. The carbon is deposited on a metal foil (typically Cu or Ni are used to best match the graphene lattice at low cost) which can be removed. Applying a hydrophobic polymer to the surface of the graphene allows the film to float in an etchant which removes the foil. The graphene can then be transferred to an appropriate substrate. The CVD process is scalable allowing commercial products to be efficiently produced.

The concept of graphene being used as a chemical sensor was first realized in 2004 by Geim and Novoselov when the hole concentration in the sheet was unintentionally changed due to ambient water content [29]. Further investigation showed

that the graphene could be doped with ammonia as well and the electron carrier concentration increased. From this discovery, it was apparent that graphene could be a potential sensing material. As stated previously, a sensing material should have fast response to the target species (such as CWA or environmental hazardous gases), ability to detect sufficiently low concentrations of the species to maintain safety and will ideally be reusable to mitigate repeated cost to the user. Graphene shows promise in these aspects with the possibility of single molecule detection [30], low electrical noise (resulting in reliable fast detection and contributes to high sensitivity) [30], [31], and has many mechanisms to make devices reusable [32]–[35]. Further, gases larger than helium are unable to penetrate graphene [28]. This property ensures that target gases will not pass through the material without interaction, thus without detection.

1.3 State-of-the Art Graphene-based Chemical Sensors

Desirable sensing materials are highly-sensitive to analytes, reusable, selective, have large-sensing area, and are cheaply and easily manufacturable. With proper care in the manufacturing procedure, it is possible to obtain these properties from graphene. For instance, Schedin et al. report graphene is capable of detecting a single molecule of gas [30]. This same report describes the possibility of reusing the graphene by heating the material in vacuum at 150°C.

As previously mentioned, the method that graphene is obtained plays an important role in the sensing capabilities of the material. Many current sensors use a graphene-oxide powder as a graphene source due to its low cost. Once reduced, the reduced graphene oxide (rGO) has properties between graphene and graphene oxide as the

graphene is not entirely reduced. The graphene flakes that result from both mechanical exfoliation and reducing graphene oxide powder tend to have poor electrical response over large areas compared to CVD graphene. Flakes do not constitute a continuous film, imposing limits on the geometry of the devices that can be produced. Further, exfoliated graphene tends to have fewer adsorption sites due to a very high-quality lattice structure, which implies that there are few defects in the graphene to act as adsorption sites. However, due to the growth procedure in CVD graphene, while the film is a continuous film, it is made-up of polycrystalline carbon in the form of adjoining domains. The edges of these domains are considered high-energy locations which can act as adsorption sites [36]. CVD provides a relatively large area with consistent electrical properties making this method of production beneficial for sensing and the manufacture of sensors in mass quantities.

Yavari et al. created a four-probe van der Pauw configuration using CVD grown graphene [35]. The graphene was grown on a copper foil using hexane as the carbon precursor. The material was then transferred to a Si substrate with an approximately 300 nm layer of SiO_2 and patterned using standard photolithography techniques. Four Ti/Au contacts were deposited at the four corners of the graphene using an e-beam evaporator. Each contact could then be used to monitor various material properties throughout exposure. Sheet resistance was determined before exposure and compared to the real-time sheet resistance during exposure. The saturation point represents the maximum response of the sensor. For example, at 100 ppm, the overall, saturated change in sheet resistance was approximately 90%, while at 500 ppb, the response was about 3%. The response time ranged according to NH_3 concentration from ~120-300 min. The proposed benefit to

this device was the small size, implying that many devices could be made from a relatively small amount of graphene. Upon complete saturation, the device could be recovered by heating at 200°C in vacuum.

Another group was able to measure the presence of NH_3 down to the detection limit of 83.7 ppb [37], [38] also using CVD graphene deposited on a copper foil and transferred to a SiO_2/Si substrate. The graphene had thin Au/Ti contacts deposited using vacuum thermal evaporation [38].

Gautam et al. used $Cu_{(500nm)}/SiO_{2(300nm)}$/Si stacked substrate instead of standard copper foil to catalyze the graphene deposition using a 1:19 CH_4 to Ar flow [39]. After the graphene deposition, a wet chemical etchant (dilute ammonium persulfate) was used to preferentially consume copper. This process allowed the graphene layer to adhere to the SiO_2 layer beneath the copper layer eliminating the need for PMMA layer. The complete process is summarized in Figure 5 where step 1 is the Cu deposition, step 2 is the graphene deposition and step 3 is the copper etching: the honeycomb pattern represents graphene.

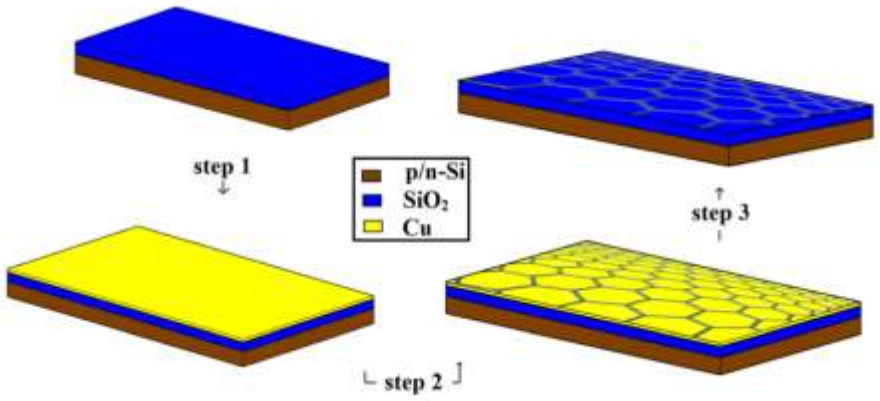

Figure 5: Graphene deposition and transfer schematic used in [39]

A 50 nm layer of gold was deposited on the graphene surface using a vacuum evaporation technique. The gold was then patterned using standard photolithography techniques in a field-effect transistor configuration after which, the device was heated at 400°C for 1 hour in a N_2 flow to remove any adsorbed organic material from the sensing surface. This approach led to a primarily 1-3 layer graphene sensor. This particular sensor used a shift in voltage from the gate to the surface before and after exposure to detect NH_3 in concentrations from 6-200 ppm. Due to system constraints, the group could not produce concentrations <6 ppm. Even at 6 ppm, the group reported a change in voltage of 2.5-5 V, where this value was >35 V for 200 ppm NH_3 exposure.

One important note from this research to this point is that few reports exist which describe the effects of functionalizing CVD graphene sheets for its use in chemical sensing. Based on the improvements that functionalization allows in other material systems, its use in CVD graphene may further improve the sensing capabilities of the material. A more in-depth review reveals that CVD graphene can indeed be improved by use of functionalization.

1.4 Graphene Functionalization

Since graphene shares many attributes with other organic materials, it is expected that some properties may be similar. One aspect of this similarity is the ability to functionalize the surface for various purposes. Functional groups tend to change the adsorption mechanism to the graphene. This can be done by adsorption catalysis or by increasing the number of adsorption sites, both of which will improve the sensitivity of the sensor. If well chosen, the functional groups can take advantage of preferential

adsorption allowing for an improved selectivity which has been an issue in pristine (especially exfoliated-) graphene sensors. This section will focus on the importance of proper functionalization, thermal treatments, and metal nanoparticle decoration along with their influence on critical sensing response.

Early experimentation with graphene as a sensing material demonstrate the possibility of its use in detection of water, ammonia, NO_2, etc. Concerns of contamination during the manufacturing process of the sensor were investigated. Poly(methyl-methacrylate) (PMMA), a chemical used in the process of the device fabrication, was said to exist in a ~1nm thick layer on the graphene after the process was completed [40]. In [40], the authors demonstrate a device with and without the PMMA contamination layer. The PMMA layer was removed in an H_2/Ar environment at 400°C for a period of 1 hour, after which, the same device was used to measure the same gases as before. The group determined that the sensitivity of the graphene was less than the graphene with a PMMA layer. Sensitivity to the tested gases decreased to nearly zero implying that the contamination layer had increased the sensitivity of the sensor. It was determined that the contaminant unintentionally functionalized the graphene, allowing for improved charge transfer mechanisms and higher rate of adsorption to the exfoliated graphene. It was reported that the exfoliated graphene was only able to detect ammonia at 1000 ppm with a response of ~1% [40]. This research underscores the importance of proper functionalization as even standard processing procedures can modify graphene unintentionally.

There are essentially two forms of functionalization that can be performed on graphene. Covalent functionalization generally breaks the graphene lattice and removes

some of the better qualities of the material and, in high concentration, is thus less desirable for gas sensing. However, in low concentrations, functional groups such as oxygen can improve selectivity without significant harm to the electrical properties [41]. Non-covalent methods tend to retain the symmetry and lattice of the graphene, allowing the benefits of the functionalization as-well-as the benefits of pristine graphene [41], [42].

Very often, oxygen and oxygen-containing groups are used to functionalize graphene. This is mainly observed when graphene oxide (often GO) is partially reduced to "reduced graphene oxide" (rGO.) While the oxygen content is still much higher than that of graphene, some electrical properties of graphene are observable. Oxygen is used due to its ability to bond to known polymers which can act as functional groups.

1.4.1 Graphene Functionalized with Metal NP

While graphene can be highly sensitive to gases, the low number of dangling bonds reduces the likelihood of sorption the target molecules. Li et al. proposed metal nanoparticles to improve the number of adsorption sites [43]. While this work is performed on CVD graphene intended for a surface acoustic wave sensor, the mechanism is likely to be independent of the sensing mechanism since the number of adsorption sites is increased in all cases. This group used $HAuCl_4$ in various concentrations to immerse CVD graphene (still on the copper foil) for a set time. The $HAuCl_4$ acts as a gold (Au) source for the decoration of the graphene with gold nanoparticles (AuNPs.) The decorated graphene was then transferred and incorporated into a sensor. It was determined that the concentration and time of the immersion changed the properties of the sensors due to the distribution and geometry of the particles. The response time and

recovery time were monitored as related to the concentration of the AuNP. Three sensors were made from 0.5 mM $HAuCl_4$ immersions at 1-, 5-, and 10 s. The morphology of the NPs on the graphene are shown in Figure 6.

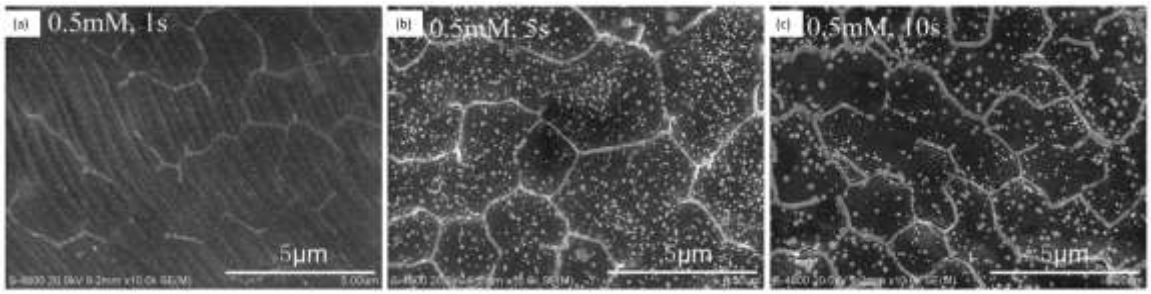

Figure 6: SEM images of AuNP on CVD graphene using various immersion times in $HAuCl_4$ [43]

The sensor response is compared in Figure 7. The longer immersion time produced the proper morphology to have repeatable and nearly 100% recoverable sensing. Optimization of the morphology for particular properties appears essential to proper performance. In Figure 7, the red arrows represent the time at which NH_3 is introduced at a concentration of 2620 ppm. The blue arrows represent the time at which the NH_3 source is removed and the sensor is permitted to recover. The morphology of the AuNPs, developed by a 5 s immersion, do not allow for full recovery in the specified time period given by the change in insertion loss from exposure cycle to exposure cycle. At 10 s immersion, the sensor is able to fully recover shown by the nearly identical cyclic behavior.

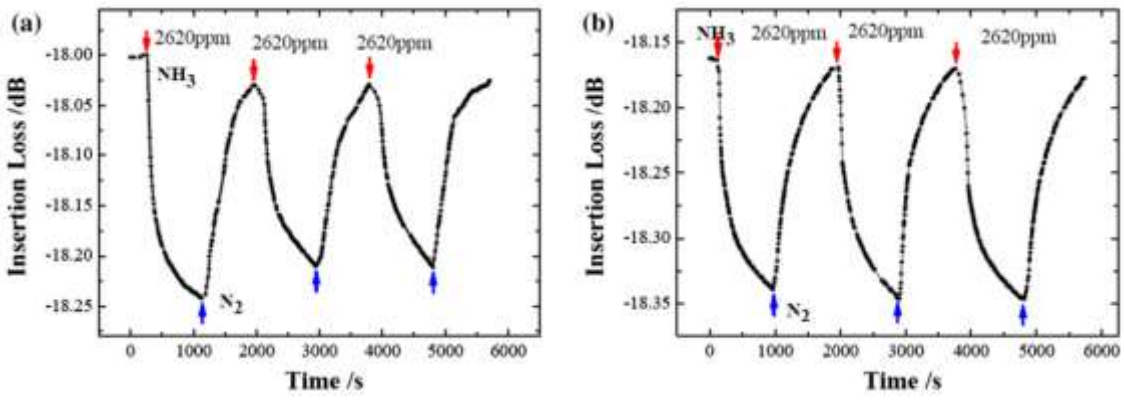

Figure 7: Surface acoustic wave sensor response to NH_3 with 5 s (a) and 10 s (b) immersion in 0.5 mM $HAuCl_4$ [43]

Gautam and Jayatissa experiment with gold and platinum nanoparticles in two separate works, [44] and [45] respectively. AuNP deposition was carried out on graphene grown on copper foil after transfer to the desired substrate using a wet copper etching procedure [44]. $HAuCl_4 \bullet 3H_2O$ was used with KBH_4 as a reducing agent. The platinum nanoparticles (PtNPs) were deposited using a thermal evaporation of Pt at 10^{-7} Torr with an approximate deposition rate of 10 Å/s [45] To reduce agglomeration of the NPs, the samples were heated to 400°C in H_2 for 1 hour. The resistance (normalized to the resistance at 330 K) of the AuNP decorated graphene was reduced at temperatures above ~370 K when compared to pristine graphene at the same temperatures. The normalized resistance (to resistances measured at 310 K) of the PtNP decorated graphene also showed a lower value above ~350 K. Decoration of graphene with Au- and PtNPs increased the recoverability of the gas sensor. The sensors with decoration show repeatability within 2% for both metals. This recovery is shown in Figure 8.

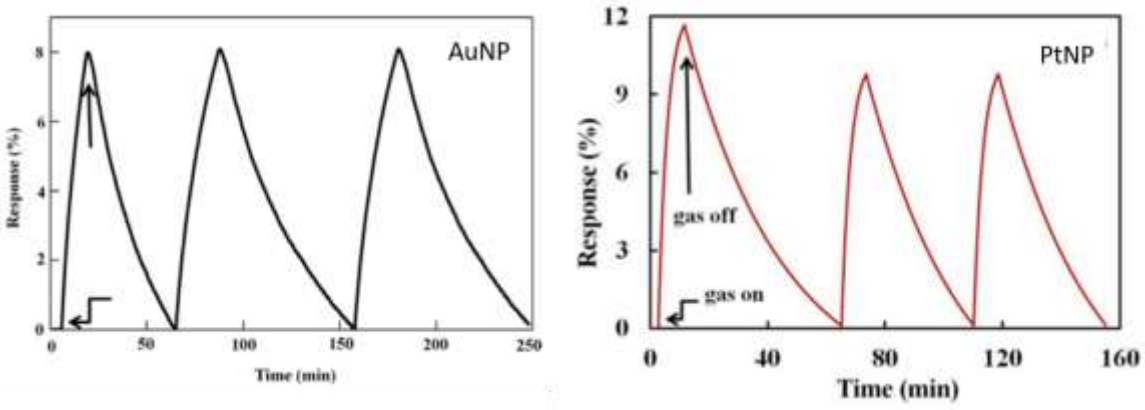

Figure 8: Response and recovery of graphene sensors decorated with AuNP (left [44]) and PtNP (right [45])

1.4.2 Graphene under Thermal Treatments

Temperature is used on occasion to change the properties of materials. In the case of graphene and graphene-based materials, temperature can be used to anneal graphene and reduce stresses by reducing wrinkling. Elevated temperatures can be used in atmosphere or under vacuum. One effect of exposing graphene to higher temperatures is desorption of vapor species that have been adsorbed to the surface, however, an unintentional doping effect has also been reported [46]. This unintentional doping was noticed when heating graphene in vacuum then exposing the sample to ambient air. Initially, the graphene is expected to have gaseous species on its surface. When heated, the added thermal energy is enough to desorb the species. When the graphene is re-introduced into ambient air, there is oxygen and water vapor that can interact with the now-vacant adsorption sites. These species dopes the graphene through charge transfer, changing the electronic response of the layer [46].

Experimentation shows that 30 s of graphene annealing in nitrogen has different effects based on the temperature [47]. The temperature range explored in [47] started

with a control sample (marked as 25°C annealing) followed by rapid thermal processing at 200°C increments from 200-1000°C. The results show a decrease in graphene roughness measured using atomic force microscopy (AFM) root-mean-square (RMS) averaging for all temperatures less than 1000°C when compared to the control sample. The roughness was least for samples treated at 200°C while 400- and 600°C treatments show a similar roughness ~2-times that of the 200°C sample. A treatment of 800°C shows a roughness only slightly less than that of the control. At 1000°C the sample had more roughness than the control. As most CVD graphene is grown at ~1000°C, it is assumed that CVD graphene will be stable at temperatures less than the growth temperature and under vacuum.

Another group used air to observe the thermal stability of graphene [48]. Samples of CVD grown graphene, grown on Cu foil at 1000°C, were heated in a tube-furnace for 5 minutes at temperatures above 200°C. As areas of the CVD graphene were 2-layer, the effects of single-layer and bi-layer graphene could be evaluated side-by-side. The results show that a second layer of graphene tends to stabilize the first layer of graphene to withstand higher temperatures. The critical temperature of 500°C was determined to be the starting point for the onset of defect formation in single-layer graphene. Even temperatures as-low-as 200°C show a change in graphene edge structure resulting in the inhomogeneous reaction rate with oxygen [48].

Pitting was observed upon thermal treatment in exfoliated single-, double-, and tri-layer graphene [49]. This group heated single layer graphene for two hours at temperatures ranging from 200-600°C in the presence of O_2/Ar. There was not any reported oxidation or pitting at temperatures at or below 400°C. Hole doping, however,

was reported at temperatures at and below 400°C. Pitting was said to begin at 450°C. Higher temperatures tended to increase the size and decrease the number of the pits by coalescence of smaller pits. The authors also describe the possibility of curvature and defects having higher reactivity. This is especially important to understanding the reactivity of CVD graphene due to processing defects during growth and/or transfer.

1.5 Objective of This Research and Overview of the Thesis

Based on the information discussed to this point, there is no doubt that portable chemical sensors capable of identifying and quantifying the target species in real-time are highly desired. Among various sensing materials, graphene is promising for applications to chemical/biological sensing due to its unique properties. Graphene, similar to conductive polymers and carbon nanotubes, can be functionalized to enhance its catalytic activity and electrical properties for the benefits of detecting and distinguishing trace hazardous gases. This research effort is to functionalize and characterize graphene towards its application to chemical sensing with high sensitivity and selectivity. The scope of this research is limited to CVD graphene sheets modified using nanoparticles and oxidation via thermal annealing as well as oxygen plasma. The modified graphene was characterized using various approaches. Detailed experiments, results, discussion, and conclusions can be found in the following chapters:

Chapter 2 will discuss the general electronic properties of graphene as reported in other works, promising methods of functionalization of graphene sheets, methods for characterizing graphene sheets. These methods include Raman spectroscopy, Hall/ van

der Pauw measurements, radio-frequency (RF) characterization, and use of a scanning electron microscope (SEM).

Chapter 3 details experimental results of functionalizing graphene sheets with gold- and platinum-containing solutions.

Chapter 4 covers experimental results of functionalization/modification of the graphene sheet via annealing in ambient air using oxygen as a functionalizing agent.

Chapter 5 shows the results of indirect measurement of an electrically inactive layer of graphene formed by oxygen plasma etching, a standard processing technique via Raman spectroscopy.

Conclusions and future work are given in Chapter 6.

2 Graphene Characterization Approaches

The characterization approaches presented in this chapter were chosen to introduce and justify approaches which are used in this research for evaluating pristine graphene and functionalized graphene. These methods include measurement of the electronic properties of graphene with the Hall technique and radio-frequency scan; analysis of the Raman spectra; and use of the scanning-electron microscope for topographical and compositional analysis. These approaches are not exhaustive of all methods of characterization.

2.1 Graphene Electronic Properties

Ideal graphene is considered a "perfect semi-metal" as there is no bandgap between the valence and conduction bands of the sheet, along with the fact that there are no charge carriers at the Fermi energy. While the strong σ-bonds have a bandgap, the π-bonds have no bandgap. This zero-energy bandgap is due to the conjugated bond structure in the carbon atoms. Due to the general stability of the carbon-carbon bond, in well-oriented graphene, the electron mean-free-path can reach ~1μm. This implies high mobility and few electron collisions [26] resulting in fast response times for sensing.

The mobility of the charge carriers is effectively the speed at which the carriers travel per unit electric field. Conductivity (σ) is related to the product of mobility (μ), carrier concentration (n), and charge (q). When the charge carriers are electrons or holes,

the value of q is that of the elemental charge. Conductivity is the inverse of resistivity (ρ), both of which do not rely on the geometry of the material. With 2-D materials, the charge carrier concentrations are often given in values of cm^{-2} to emphasize the dimensionality. Sheet resistance R_s is therefore used to describe the resistance of 2-D materials. The value of R_s can be obtained by normalizing the resistivity to the thickness (t) of the sheet. Units for sheet resistance are Ω/□ to distinguish it from standard resistance. Equation (1) shows the relationship between conductivity (σ), mobility (μ), carrier concentration (n), and charge (q), resistivity (ρ), sheet resistance R_s and thickness (t).

$$\sigma = \mu \times n \times q = \frac{1}{\rho} = \frac{1}{R_s \times t} \quad (1)$$

As with most materials, properties in graphene are changed when defects are present. Defects constitute any change in the crystal lattice, namely: vacancies, interstitials, grain boundaries/edges, and inter-layer effects. Even the substrate can induce a change in the electronic behavior of the material. This is evident by the mobility results of graphene suspended in air (~10^5 $cm^2V^{-1}s^{-1}$) versus graphene supported by a substrate of SiO_2 (~8×10^3 $cm^2V^{-1}s^{-1}$) [50].

Graphene's electrical properties are also dependent on the number and relative orientation of the of layers making up the sheet. Layers are bonded through van der Waal's forces which are weaker than the primary σ-bonds. Layering schemes can be ABAB (Bernal), ABCABC (rhombohedral), or randomly oriented relative to the previous layer (turbostratic) [23]. A, B, and C represent the location of atoms relative to the previous layer. Figure 9 shows the superimposed possible layer arrangements by color

(e.g. A=black, B=green, C=red.) The atoms are represented by the vertices of the colored lines.

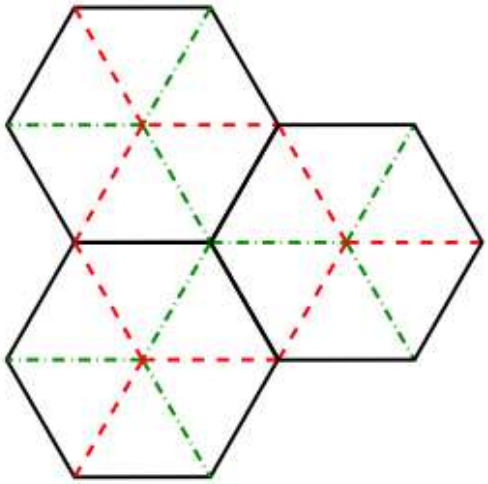

Figure 9: Multiple layer graphene structure [26].

2.2 Hall Effect and van der Pauw Measurement

One approach to measuring the electronic properties of graphene is the Hall technique. The Hall effect is caused by an applied magnetic field non-parallel to an electrical current. These measurements require four probes which can both measure *and* apply current and voltage. When the magnetic field interacts with mobile charge carriers, the charge carrier experiences a change in direction based on the current direction relative to the applied magnetic field and the sign of the charge. A change in potential is then experienced in the direction perpendicular to both the current direction and magnetic field direction aptly named the Hall voltage. The polarity of the Hall voltage signifies the majority charge carrier in the material. The sheet carrier concentration is related to the current I, the Hall voltage V_H, the magnetic field B, and the carrier's charge (for holes and electrons, this value is the elemental charge q.) These quantities are related in Equation

(2). The Hall mobility μ_H can be calculated using Equation (3) where R_s is the sheet resistance.

$$n_s = \frac{I \times B}{q \cdot |V_H|} \tag{2}$$

$$\mu_H = \frac{|V_H|}{I \cdot B \cdot R_s} \tag{3}$$

As sheet resistance is not given by a traditional Hall measurement, another technique must be used. Van der Pauw measurements can be used to determine the sheet resistance and mobility respectively. Probes are placed at the corners of square-shaped samples. The leads are to be as small as possible and minimally interior to the sample material to avoid significant error in sample measurement. A current is applied to two adjacent probes while the voltage is measured across the other two probes. This process is repeated with all combinations of adjacent corners. Further detail is beyond the scope of this paper but is detailed in [51].

2.3 Radio Frequency Characterization

A Smith chart is a visualization tool typically used to predict parameters associated with radio-frequency (RF) devices. Although initially intimidating, the Smith chart is quite useful and simple to interpret with practice. A series of circles of varying radius are made tangent at the right-hand side of the chart expanding with larger circles to the left. Each circle represents the real part of the normalized impedance (normalized resistance) of the RF device where the normalization factor is the characteristic impedance of the system. A second series of circles (both above and below the horizontal axis) represent the normalized imaginary part of impedance (normalized reactance) of the

device. This chart allows for quick visualization of both magnitude and phase of the impedance. Above the main horizontal, the reactance is positive relating to inductance; below the main horizontal, the reactance is negative showing capacitive nature. The far-left point of the main horizontal represents a short-circuit (zero resistance), the center of the chart is perfect match of the characteristic impedance to the device (normalized resistance is unity), and the right point represents an open-circuit (infinite resistance). The imaginary part of the impedance depends on the frequency applied. At low frequencies, capacitive devices act similar to open-circuits, while at high frequencies, they act similar to short-circuits. Therefore, increasing frequency will shift a point on the Smith chart from a point below the main horizontal to a second point below the main horizontal, shifted to the left. Inductive devices act opposite to capacitive devices in that reactance is positive (above the main horizontal), at low frequencies act similar to short-circuits, and at high-frequency act similar to open-circuits. Therefore, an inductive component will shift from left to right (not in a direct manner) when sweeping from low to high frequencies and would remain above the main horizontal on the Smith chart.

Figure 10 shows a non-truncated version of a simple impedance Smith chart. The parameter Γ is the reflection coefficient and is represented as a complex quantity. The red axes represent the pure real (Γ_r where the Γ_r axis is also referred to as the "main horizontal" in this text) and pure imaginary (Γ_i) components of Γ. In this chart, the green circles represent constant (normalized) resistance (R`.) The black circles represent constant reactance curves. When R` = 0 Ω, $|\Gamma| = 1$ which is shown as the largest green circle. $|\Gamma| = 1$ in Figure 10 is typically used as a boundary of the Smith chart; beyond this

boundary, there is no physical meaning. The black arrow is pointing to the open-circuit point, where R` = ∞ and represents pure reflection with the same phase.

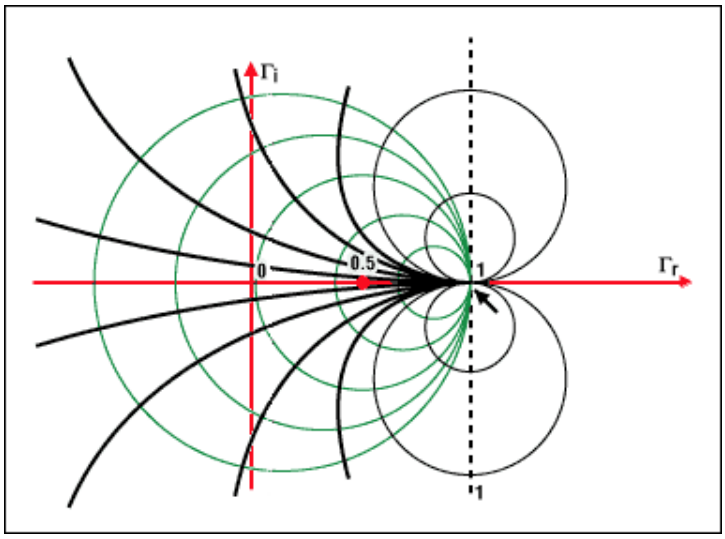

Figure 10: Expanded Smith Chart [52]

2.4 Raman Spectra of Graphene

The Raman process is related to the interaction between incident light and a sample. Most incident light will not interact with the sample and will have no change in energy (frequency) referred to as elastic or Rayleigh Scattering. However, a small quantity of the light will interact with the material and the frequency of the photon emitted will differ from the incident light. If the energy of the photon is *less* than the incident light, it is called Stokes scattering, while if the energy of the detected photon is *higher* than the incident light, it is called anti-Stokes scattering. Both Stokes and anti-Stokes scattering are forms of Raman scattering [53]. Typically the ratio of Rayleigh scattered photons to Raman scattered photons is ~10^6 [53]. As energy must be conserved, the amount of energy lost(gained) in Stokes(anti-Stokes) scattering process must be

directly related to the interaction of the specimen. For this reason, the underlying interaction can be characterized by Raman scattering. One of the greatest advantages of Raman spectroscopy is the non-destructive nature of the measurement. This allows the graphene to be probed at various times during the processing giving a one-to-one comparison using the exact same material to observe any changes [54].

In a typical Raman microscope, monochromatic laser light is focused through a microscope onto a sample using a series of optics. Filters are commonly used to reduce or eliminate the Rayleigh scattering events that reach the detector. A detector located near the laser is used to determine the energy gained or lost for scattering events sufficiently different from Rayleigh scattering. The detected events are plotted on a spectrum with intensity (in terms of event counts) on the vertical axis and Raman shift (a measure of the change in energy, typically in terms of cm^{-1}) on the horizontal axis.

2.4.1 Raman Peaks in Graphene

The Raman spectrum of pristine graphene consists of two prominent peaks in the Stokes regime. These two peaks are named the G peak found near[1] 1580 cm^{-1} and the 2D (some call this the G` peak) near 2700 cm^{-1} [54]–[56]. Figure 11 compares the Raman spectra of graphene and graphite. In this figure, the 2D peak in graphene is to the right and the G peak, to the left. In regions that have a broken symmetry, a third peak arises at 1350 cm^{-1}. This third peak is called the D peak and is often associated with structural

[1] Unless otherwise marked, the peak positions will be with an excitation energy of 2.41eV

defects in the lattice [57]. The vibrational mode associated with the D peak is a "breathing mode" of the carbon rings. With high symmetry, this mode is destructive and therefore, does not appear. However, when there are contributions by part of this ring which are not canceled out by symmetry, (i.e. where symmetry is lost) the D peak emerges [55], [57]–[59]. The 2D peak is an overtone of the D peak (~2700cm^{-1}) which is active even when there is crystal symmetry [54], [55], [57], [60]–[64]. Upon a certain degree of defects are present, the D` peak emerges near 1620 cm^{-1} [54]. It is important to note the excitation energy used for the laser when viewing Raman data for graphene. This is due to a dispersion of the response relative to the excitation energy. For instance, there is an approximate change in 2D peak position of 100 cm^{-1} / eV, meaning comparing spectra taken at different excitation energies will be impossible without correcting this dispersion [57]. The pristine and defective graphene Raman spectra are shown in Figure 12.

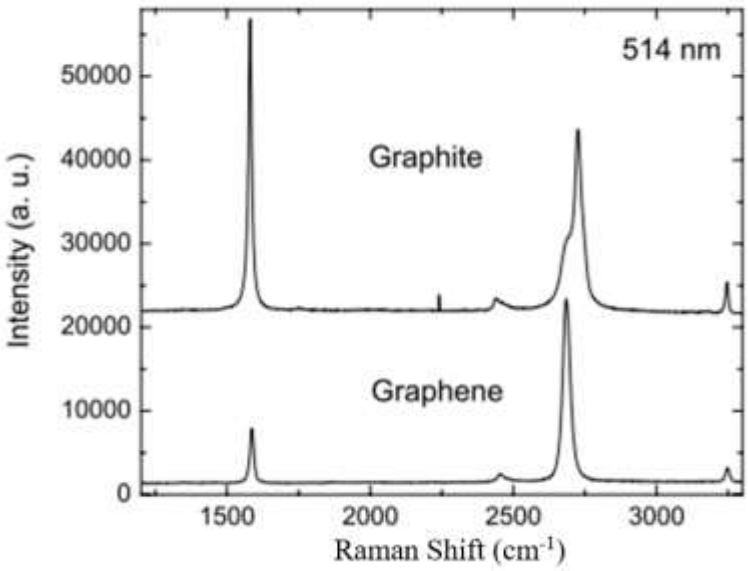

Figure 11: Raman spectra of graphene and graphite with 514 nm excitation energy [65]

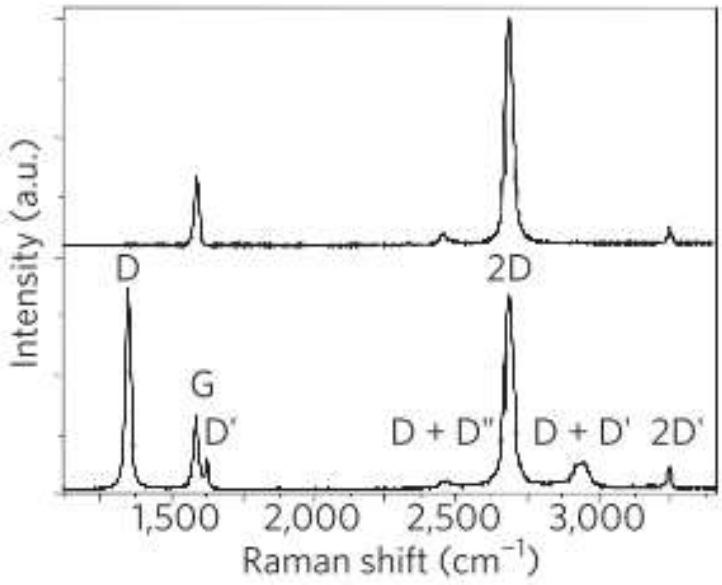

Figure 12: Raman spectra of pristine (top) and defective (bottom) graphene [57]

2.4.2 Obtainable Information

While the Raman spectrum is generally simple to obtain, the interpretation of results can become quite difficult [54]. This is due to a very low number of peaks in the Raman spectrum. Peak position, shape, width, and relative intensities, however, can be quite telling of the changes in the structure. Presence of the D peak for example is indicative of defects (grain boundaries, vacancies, edges, adatoms, etc.) Shifts in the G peak and 2D peaks can be linked to strain of the graphene film within the sheet [66] assuming the excitation energy is constant. Shifts in 2D and G peaks can also be related to the doping concentration of the sheet [66]. The number of layers can be predicted based on the shape of the 2D peak, and the intensity ratio of the 2D peak to the G peak [65].

Normalizing peak intensities to the G peak is typical. It is generally shown that 2D/G intensity ratio is greater than 2 and can reach values ~4 for single-layer graphene

[55], [65]. Another useful ratio is that of the D/D` which was initially generated from the slope of the D/G versus D`/G plot [58]. This ratio reaches particular values for different defects and can therefore be used to identify the type of defect present in the graphene. The presence of sp^3 carbon shows a D/D` ratio of ~ 13, vacancy-like defects show a value of ~7, and domain boundary shifting causes a value ~3.5 [48].

2.5 Scanning Electron Microscopy and Energy Dispersive Spectroscopy

The surface morphology of graphene was imaged with the help of scanning electron microscope and the nanoparticle element was identified using energy dispersive spectroscopy.

Scanning electron microscopy (SEM) uses an electron beam to probe the material. There are different interactions that can occur between the material and the incident beam: secondary electron generation, electron backscatter diffraction, or X-ray generation. For the purposes of graphene, backscattering diffraction will not be addressed, however, secondary electrons and X-ray generation can be used to characterize the material.

Secondary electrons are electrons that have been “kicked-out” of the material after an electron-beam (probe) impinges on the material. Typically, the topology of a material can be explored using the secondary electrons since secondary electrons from the peaks of a material are readily detected since there is no material between the material and the detector. Electrons emitted from flat or valley areas are mostly absorbed by material surrounding the probed point. For this reason, more electrons are detected from edge-like locations than from lower/flatter locations which are indicated by brighter areas

and darker areas in an image respectively. Figure 13 shows a schematic of secondary electrons from an arbitrary material. In the figure, the dark line represents the surface of the material, beneath which is the bulk material. The teardrop-shaped features represent the penetration depth of the impinging electron beam from the microscope. The higher the accelerating voltage, the larger volume of material is probed by the beam meaning a higher penetration depth. The arrows represent the emitted secondary electrons' directions and energy (length.) Arrows that do not break the plane of the surface are representative of electrons which do not reach the detector do to re-absorption by the material. From the schematic, it is apparent that more electrons are able to reach the detector (which would be at the top of Figure 13) from the edges of the surface when compared to the flat regions.

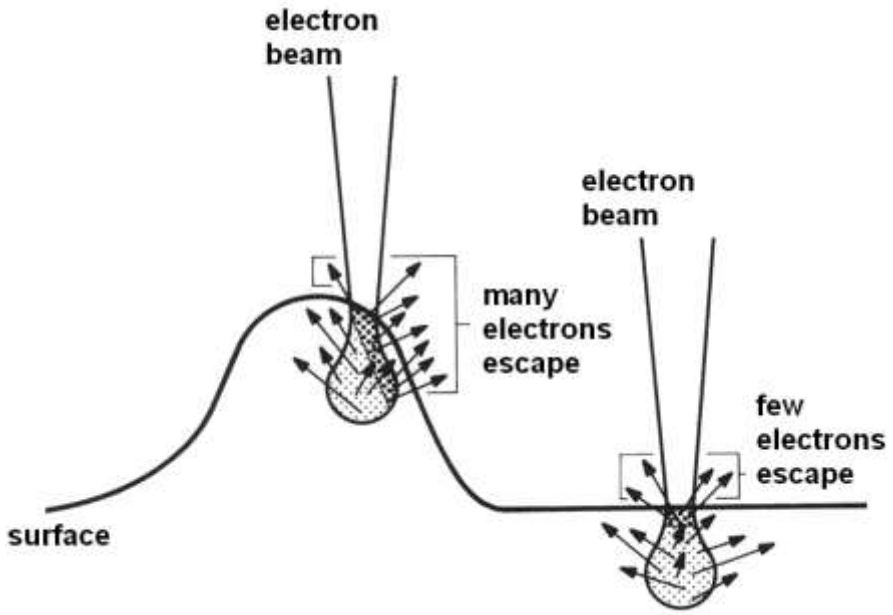

Figure 13: Secondary electron schematic for contrast in SEM imaging [67]

SEM images of graphene can be difficult to interpret. This is because the schematic shown in Figure 13 is not a good representation of graphene. Since graphene is only, at most, 10 atoms thick, the electron beam tends to penetrate the film when the acceleration voltage is relatively high, without much interaction with the material. Therefore, contrast comes from interaction of the secondary electrons generated by the substrate with the graphene rather than a direct interaction with the electron-beam and the graphene. A low voltage is necessary to obtain topological information for this reason [68]. Ref. [68] discusses that two types of wrinkles were observed in a CVD graphene sample which had been transferred to SiO_2. The two types are circled in yellow and blue in Figure 14b. The wrinkle in yellow is expected to have a higher peak than the type in blue based on the explanation in Figure 13 and Figure 14c. Higher peaks have a higher probability of having signal reach the detector resulting in higher intensity. The accelerating voltage for Figure 14a-b is 1kV at magnifications of 29,585X and 51,692X respectively. The scale bars represent 1μm. The lighter grey area to the bottom-left of Figure 14a is the contrast given by the SiO_2 substrate with no graphene.

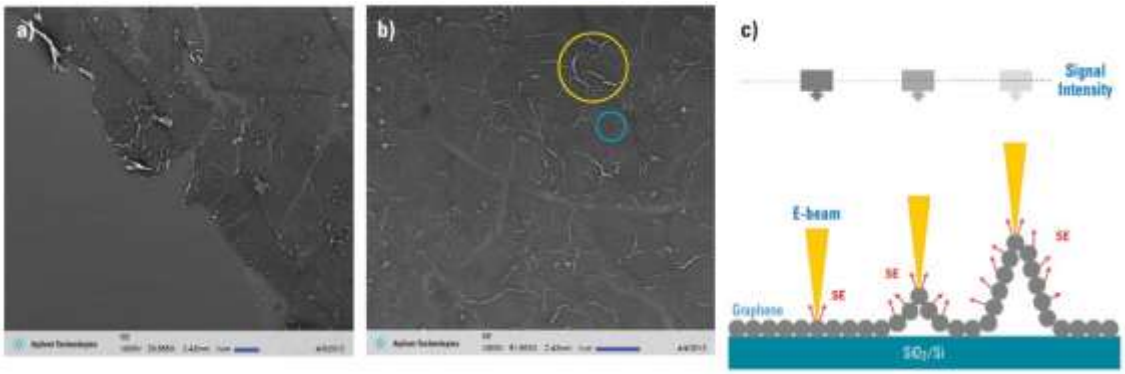

Figure 14: SEM secondary electron images of graphene (a) near edge of graphene, (b) interior regions of CVD graphene sheet. (c) is a schematic of secondary electron contrast. [68]

Darker contrast can also give insight to the thickness of the film. Thicker regions will have lower intensity since there is more material to absorb the secondary electrons generated by the bottom layers of graphene. Unfortunately, some researchers have also observed a contrast reversal based upon the acceleration voltage for graphene on SiO_2 substrates [69]. This is reportedly due to a larger number of electrons leaving SiO_2 than the electron beam delivers. Electrons from graphene then are transferred to the now-positive substrate. Therefore, more secondary electrons come from SiO_2 than graphene for accelerating voltages at or below 1 kV. The contrast reversal is shown to be at 3 kV where there is a minimum of electron transfer from graphene to SiO_2. Beyond 3 kV, secondary electrons come from graphene rather than the substrate.

When an electron from the beam strikes a lower-level electron within the material, it can be ejected from the material. To reduce energy, an electron from a higher energy level will fall to the ejected electron's (previous) state. Since the energy must be conserved, there is an emission of an X-ray as the high-energy electron falls to a lower-energy state. Due to the quantum nature of the atom, the energy of the emitted X-ray will be characteristic of a particular element on the periodic table. This energy change from the incident beam is used to identify (and in some cases, quantify) the presence of elements within the material. Generally, the energy change is taken over a period of time with either a rastering beam, or an isolated point being probed. The changes are binned into a histogram and the elements can be identified from this spectrum, where each element has peaks representing the different energy losses experienced by the electron. This technique is called energy dispersive spectroscopy and can be immensely powerful in characterizing materials. The basic principle is shown in Figure 15. Here, the yellow

arrow represents the electron-beam of the microscope, the blue arrow represents the expulsion of a core electron, and the blue circles are electrons. The solid red arrow represents the electron fall from K to L, where K, L, and M are possible energy states for this element. The red dashed arrow represents the X-ray that is characteristic of the L-K transition for this element.

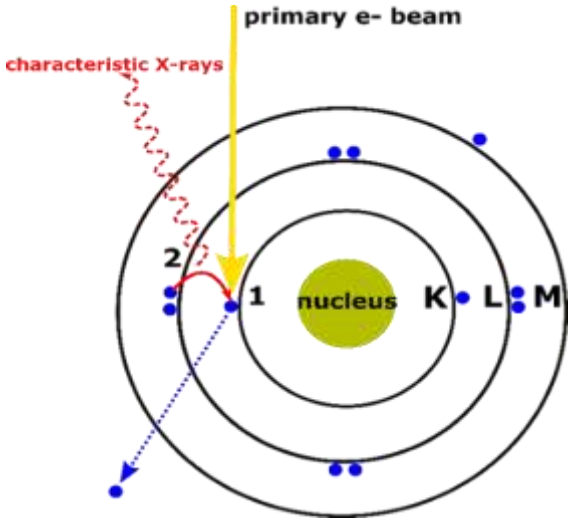

Figure 15: Schematic of X-ray generation for use in energy dispersive spectroscopy [70]

2.6 Summary

The techniques presented in this chapter have been widely used to characterize graphene and graphene-based materials. If multiple techniques are used in parallel, it may be possible to extract material properties such as conductivity/resistivity, number of charge carriers, mechanisms for electrical phenomena and so-on. Hall/van Der Pauw measurements in conjunction with SEM imaging can be used to observe changes in electrical properties. These two techniques could be further analyzed with RF results which can show a more complete picture of the electrical changes in the material. Use of Raman spectroscopy can be used to show many interesting properties or changes in

graphene. Information about structure, electronic properties, and even mechanical properties can be obtained from this non-destructive technique. Being non-destructive allows for process-induced changes to be monitored in a step-by-step analysis if needed. Relating these properties to the sensing capability of graphene may become possible, allowing new forms of modification to be explored to improve the sensitivity and/or selectivity.

The following research employs the techniques and characterization approaches presented in this chapter to help evaluate changes in graphene as functionalization is applied to the graphene system.

3 Characteristics of Graphene with Metal Nanoparticles

Metal nanoparticles have been shown to catalyze gas adsorption and dissociation processes. Gold and platinum have shown advantageous properties for gas sensing by making gas sensors repeatable and, in some cases, more sensitive (as addressed in Chapter 1). In this study, gold and platinum were each chosen to act as a functional catalyst/adsorbent on graphene. The electronic transport properties are obtained for graphene decorated with metallic nanoparticles (NPs) and deposited in-house.

3.1 Experimental

3.1.1 Pristine CVD Graphene

CVD monolayer graphene (~1cm by 1 cm) transferred to SiO_2 (300 nm)/Si substrates were purchased from ACS Materials.

3.1.2 Graphene decorated with Au Nanoparticles

The gold solution was 0.05 mg/mL of 10 nm diameter gold nanoparticles (AuNP) in citrate (NanoXact by nanocomposix). Acetone was used to dilute the molar gold concentration to ~1μM. The solution was deposited on graphene surface using an Air-Brush with a set pressure. The spraying duration was not measured as the spray nearly immediately covered the surface of the sample. The sample was allowed to dry in air. Multiple passes of spraying were performed to tune the AuNPs amounts on graphene.

3.1.3 Graphene decorated with Pt Nanoparticles

The platinum source was Pt (II) acetylactetonate (Pt (II)-acac, Sigma Aldrich). This salt is not soluble in isopropanol or water. As the acetylacetonate groups are known to dissolve in acetone, the salt was dissolved with an appropriate amount of acetone to nearly match the molarity of the gold solution in an effort to create a one-to-one comparison of the number of depositions to the concentration of the two metals. To act as a PtNP site initiator, the graphene was heated using a hot plate in ambient air at 300°C for 2 hours. This was done to create high-energy disturbances in the lattice to act as nucleation sites for platinum growth. The solution was, again, deposited using the same Air-Brush technique and settings as were used for the AuNPs.

3.1.4 Hall/van der Pauw Measurement

Hall measurement and van der Pauw measurements were performed using indium solder applied to the four corners of the graphene sheet to form the contacts for the probes. For these measurements, a 3 kG magnetic field was applied at room temperature. Each sample was measured three consecutive times under the same conditions and the data were averaged upon confirmation that the measurements were repeatable. This established a base-line for direct comparison from decorated and non-decorated graphene.

For NP decorated graphene specimens, the leads remained connected to minimize the discrepancy caused by differences in soldering. Pristine graphene was measured firstly, then NPs were sprayed on. After the Hall/van der Pauw measurement was complete of the graphene-NP, another spraying/deposition process was applied. The

measurement/spraying cycle was repeated until the resistances were too large to be measurable. A total of four depositions were measurable for gold and nine depositions for platinum.

The results are effectively a mobility-, a sheet resistance-, and a carrier concentration-plot as a function of NP deposition pass which is proportional to NP concentration, assuming that approximately the same number of nanoparticles are deposited during each deposition.

3.1.5 SEM/EDS Measurement

After the maximum NPs measurable via the Hall apparatus, the sample was imaged using a scanning electron microscope (SEM.) Further, metallic nanoparticles were analyzed using energy dispersive spectroscopy (EDS.) This was done with the help of the high-resolution Zeiss Gemini SEM 500.

3.2 Charge Transport Characteristics of Graphene-AuNPs

The Hall mobility is shown in Figure 16. The Hall mobility increased from ~1280 cm^2/Vs to ~1450 cm^2/Vs over the four depositions, an increase of ~15%. There appears to be an increase in mobility upon the first AuNP deposition followed by a decrease at 2 depositions. Excluding the first deposition, the mobility follows a smooth, increasing curve. This data was fit using linear model (y-intercept ~1278 cm^2/Vs and slope ~34.4cm^2/Vs per deposition).

The sheet resistance, measured in Ω/□ (Ω/sq), shows a nearly linear increase with the number of depositions and a change of ~2 times from the pristine graphene to the four

depositions. The experimental data and a linear fit (red) of the sheet resistance is shown in Figure 17. The linear fit shows a slope of 123.2 Ω/□ per deposition and a pristine sheet resistance of 662 Ω/□ (obtained from the y-intercept.)

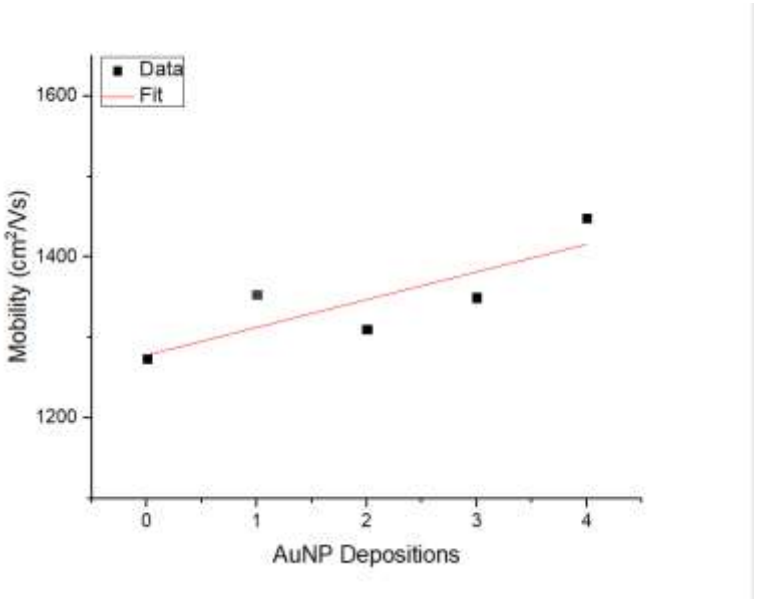

Figure 16: Hall mobility of AuNP decorated CVD monolayer graphene versus number of AuNP depositions.

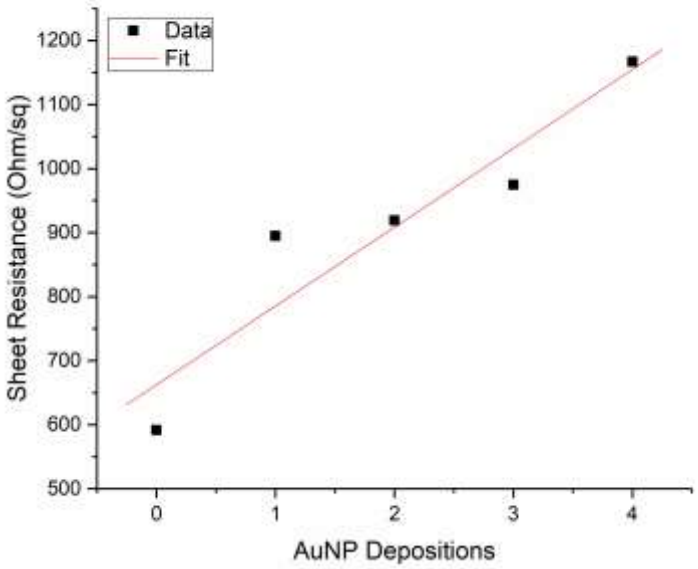

Figure 17: Sheet resistance of AuNP decorated CVD monolayer graphene versus number of AuNP depositions.

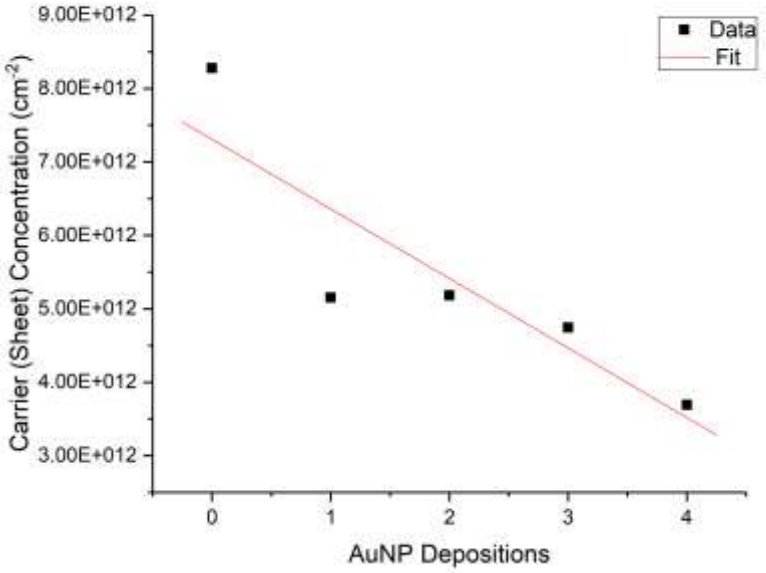

Figure 18: Sheet hole of AuNP decorated CVD monolayer graphene versus number of AuNP depositions.

From these two quantities the sheet carrier concentration was calculated. According to the Hall voltage, the majority carriers are holes in this sample. These values show a near-linear decrease in the hole concentration within the graphene sheet. The rate of carrier concentration decrease is approximately $9.48 \cdot 10^{11}$ (cm^{-2}) per deposition with a value for the pristine graphene at $7.31 \cdot 10^{12}$ (cm^{-2}) based on a linear fit of the data. The experimental data and the fitted curve are shown in Figure 18.

From these data, it is evident that the change in sheet resistance is dominated by the reduction in carrier concentration based on relative changes. The mobility increases by ~15% while the hole concentration decreases by ~50%. As the increase in sheet resistance is related to a combination of the reduction of charge carriers, and/or the reduction of mobility, both of which are directly related (with no proportionality constant), they contribute with equal weight (see Equation (1).) Though mobility

increased, the sheet resistance also increased, pointing to the reduction in charge carriers as the main contribution for the change. In fact, it is possible that the mobility was directly affected by the reduction in charge carriers. With fewer charge carriers, the likelihood of hole-hole scattering is reduced, therefore mobility can increase. This effect was not directly observed, though it is consistent with the results.

There are two likely causes for the reduction in hole concentrations with increasing AuNP depositions. One is due to electron transfer of the AuNPs to the graphene sheet. The increasing number of depositions is expected to increase the number of AuNPs on the surface resulting in larger (net) charge transfer. The second cause of lower hole concentration is due to a charge transfer of adsorbed acetone. Initially, when the sample was sprayed with the solution, the acetone was allowed to evaporate. However, it is possible that not all of the acetone was able to evaporate due to adsorption mechanisms on the graphene. This possibility was revealed during SEM imaging when the sample showed significant charging effects, indicating low conductivity. Acetone acts as a (weak) electron donor [36] which, when inserted into a p-type graphene sheet, will annihilate holes present, reducing their concentration. The sample was later heated at 300°C for 2 hours to remove any adsorbed organic species. After this desorption process, the sample was able to be clearly imaged in the SEM with little or no charging effects. For this reason, the possibility of acetone contribution to the decrease in hole concentration and the subsequent increase in sheet resistance cannot be ruled out.

3.3 Charge Transport Characteristics of Graphene-PtNPs

Mobility and hole concentration are fit with the empirical equation shown in Equation (4) due to the complex behavior of the system. In (4), y_0 represents the saturation value while A1 represents the difference in pristine and saturated graphene, and t1 represents the inverse of the coverage rate per spray.

$$y = A1 \times e^{\frac{x}{t1}} + y_0 \qquad (4)$$

Figure 19 shows the relationship between sequential depositions and the Hall mobility of the graphene-PtNP series. Similar to graphene-AuNPs, the Hall mobility increases with increasing Pt solution depositions. Starting from 1216 $cm^2V^{-1}s^{-1}$, the mobility follows a smooth curve until an apparent saturation of ~2000 $cm^2V^{-1}s^{-1}$ upon nine depositions of the Pt solution marking a ~65% increase from the pristine graphene. This is visible by an offset exponential fit of the data. Experimental data are the black data points and the red curve is a fit of the data using the empirical equation in the in-set table. The fit-parameters are also given in the in-set table.

The sheet resistance tended to increase with the number of Pt solution depositions. A linear fit was used to approximate the behavior (red curve in Figure 20.) The initial value of the sheet resistance was ~331 Ω/□, increasing to a maximum of ~431 Ω/□ at eight Pt depositions. This increase is ~30% (from initial to max.)

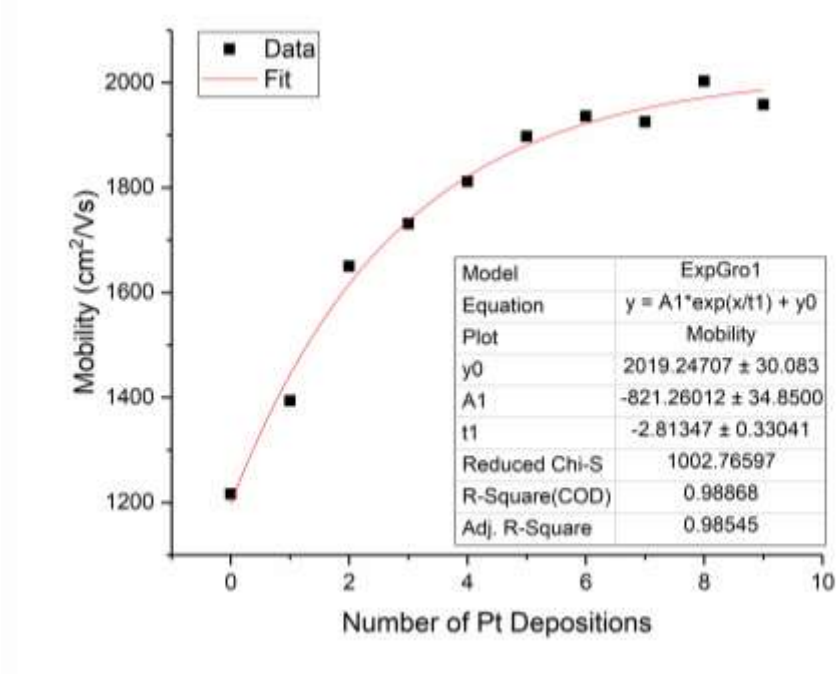

Figure 19: Hall mobility of Pt decorated CVD monolayer graphene versus number of Pt solution depositions

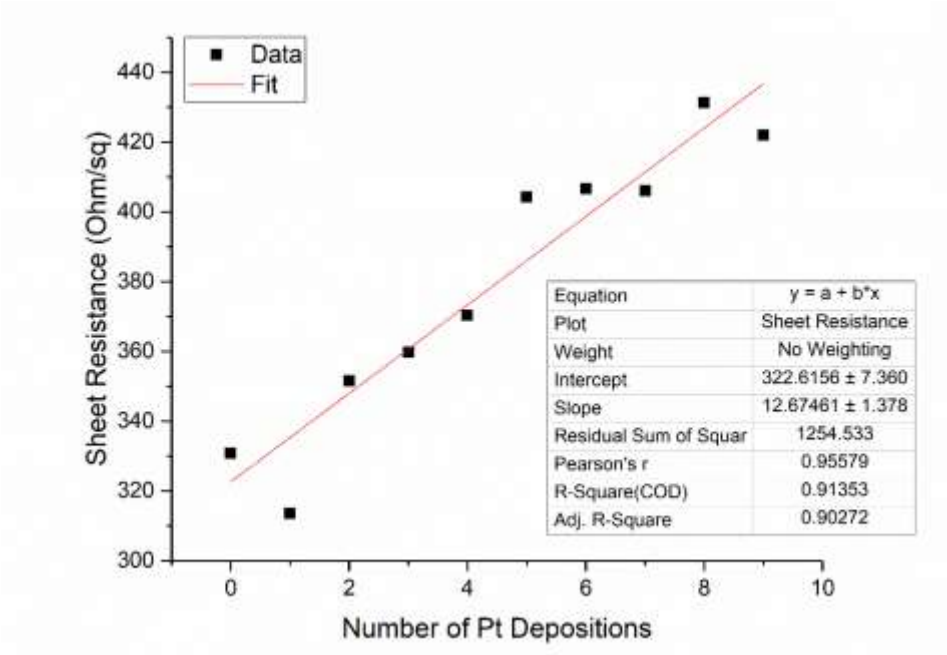

Figure 20: Sheet resistance of Pt decorated CVD monolayer graphene versus number of depositions

The mobility and the sheet resistance were used to calculate the sheet carrier concentration. The hole concentration in the pristine graphene started near $1.6 \cdot 10^{13}$ cm^{-2}. This value was reduced approximately exponentially to the lowest value of $7.6 \cdot 10^{12}$ cm^{-2} upon nine Pt solution depositions. This is approximately a 50% reduction in the number of holes from the pristine graphene to the graphene with the maximum number of Pt solution depositions. Figure 21 shows the experimental sheet (hole) concentrations versus the number of depositions of the Pt solution. The experimental data are represented by the black data points, while the red curve represents the fit of an exponential decay function to the experimental data. The fit parameters and equation of the fit are given in the in-set table.

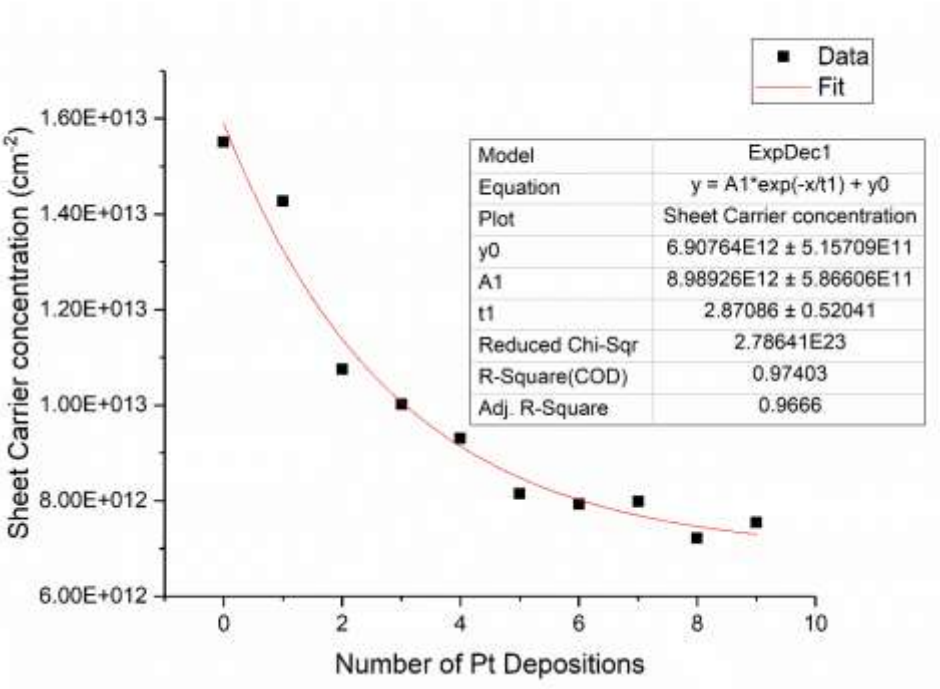

Figure 21: Hole concentration of Pt decorated CVD monolayer graphene versus number of depositions

The increase in sheet resistance is dominated by the decrease in hole concentration. This is made evident, as the in the case of AuNP concentration, by the fact that increase in mobility will decrease sheet resistance if carrier concentration and charge remain constant. A decrease in carrier concentration, with unchanged mobility and charge, will increase the sheet resistance. Since the sheet resistance increased with increasing mobility and decreasing carrier concentration, the dominant factor is the decrease in hole concentration. This is also the case for AuNP deposition. Again, the state of the Pt is unknown since the solution was formed from a salt. Platinum could exist as ions attached to negative species in the graphene, still in the form of a salt, or as platinum metal. The contribution of the organic residue, possibly from processing procedures, is also unknown.

In the case of this experiment, it is difficult to make direct comparisons based on data since the graphene sample used for the Pt decoration had been heated prior to deposition. There are many potential explanations for the increase in sheet resistance from the pre-Au deposited graphene to the pre-Pt deposited graphene. For instance, simple difference in handling of the graphene samples in different temperatures, at different humidity, or age of the sample could affect the electrical properties. Graphene is known to be doped by atmospheric oxygen and water in the form of hole doping. As is shown in Chapter 4.2-4.4, heating graphene in air in the manner used to prepare the graphene to accept the platinum solution, in-fact dopes the surface with holes and may cause the difference in carrier concentration. While this is not a quantitative study, the effects of annealing on the carrier concentration cannot be ignored. Further, the effects of

the different organic materials used for MNP stability and formation from the AuNP and PtNP samples may contribute to differences in behavior.

SEM images after the maximum concentration of platinum solution were unable to resolve features of the graphene due to charging effects. Upon a two-hour, 300°C desorption procedure using a hotplate in ambient air, the sample was re-imaged and clear images were obtained. The desorption is expected to have removed any organic residue allowing the hole concentration to replenish to a somewhat higher value. This was not directly observed due to the heat, which would be high enough to de-solder the leads used for the Hall measurements. The complication in soldering new leads to the sample is not repeatable indicating the need for subsequent measurements on the same sample without removing the leads. The near-linear response of the sheet resistance is consistent with the similar decay/growth rates of the exponentials within the constituent quantities of mobility and carrier concentration. These parameters are labeled as t1 with values of (-2.81) and (2.87) in the in-set tables of Figure 19 and Figure 21 respectively. It is assumed that domain boundaries will be the first adsorption sites preferentially occupied. The hole concentration is expected to be lower at the domain boundaries due to the injection of electrons by the PtNPs allowing for recombination. Further, a decrease in carrier concentration may also explain an increase in mobility due to less hole-hole scattering. Upon saturation of the domain boundaries, the physisorption of PtNPs on the surface of the pristine domains will not contribute electrons into the lattice, making the presence of PtNPs on the domain surface negligible to the electronic properties justifying Equation (4).

The SEM image given in Figure 22 is expected to contain graphene, SiO_2 (substrate), and platinum. Since platinum is expected to be on the surface of the graphene and also have the highest degree of curvature, it should be the highest intensity in the secondary electron image according to information in Chapter 2.5. Further, due to the decoration technique, the platinum is expected to be somewhat uniform on the surface. This is verified with EDS data. The coverage of the platinum NPs is approximately 2%. Appendix B has more details of this calculation.

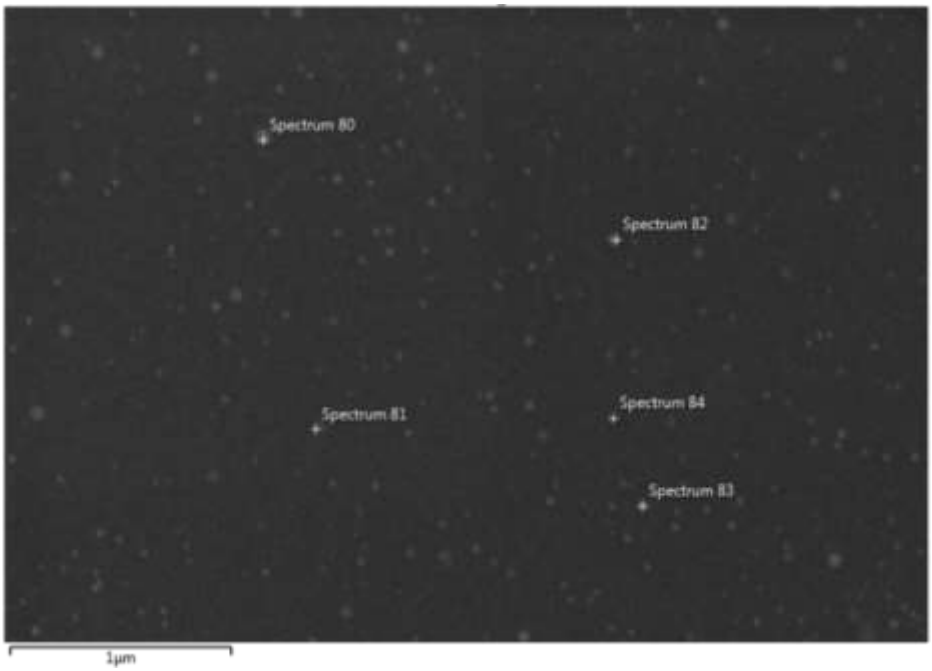

Figure 22: SEM image showing the point locations for individual EDS spectra obtained on graphene decorated with Pt solution

All EDS data for the sample sprayed with platinum were taken from Figure 22. Spectra marked 80-83 are purposely placed on the high intensity features which are expected to contain Pt. The last spectrum (84) is intentionally placed in the darker region of the sample where no Pt is expected. The spectrum at point 80-83 share many of the

same features, hence, only “spectrum 80” is presented in Figure 23a. There is a signal related to the Pt-Mα line (~2.05 keV) indicating the presence of Pt. There is also strong signal from carbon (graphene), silicon and oxygen (SiO_2 substrate). The small peaks for copper and sodium could be related to contamination of the solution or water used throughout the process. Copper may be remnant from the growth substrate as-well. Peaks lower than the carbon peak are typically not used for analysis. The peak at 0 keV represents a zero-change in energy from the electron-beam. The inset figure in Figure 23a is a close-up of the Pt peak.

The spectrum 84 is shown in Figure 23b. As is shown in the inset of this figure, there appears to be no Pt-Mα signal. From this data, it is clear that the bright features in the image (Figure 22) are related to the deposition of platinum on the graphene surface. The ionic-state of the platinum is still unknown. It is interesting that the copper and sodium peaks are also missing from Spectrum 84. For this reason, the copper and sodium are expected to be attracted to the same high-energy sites as the platinum.

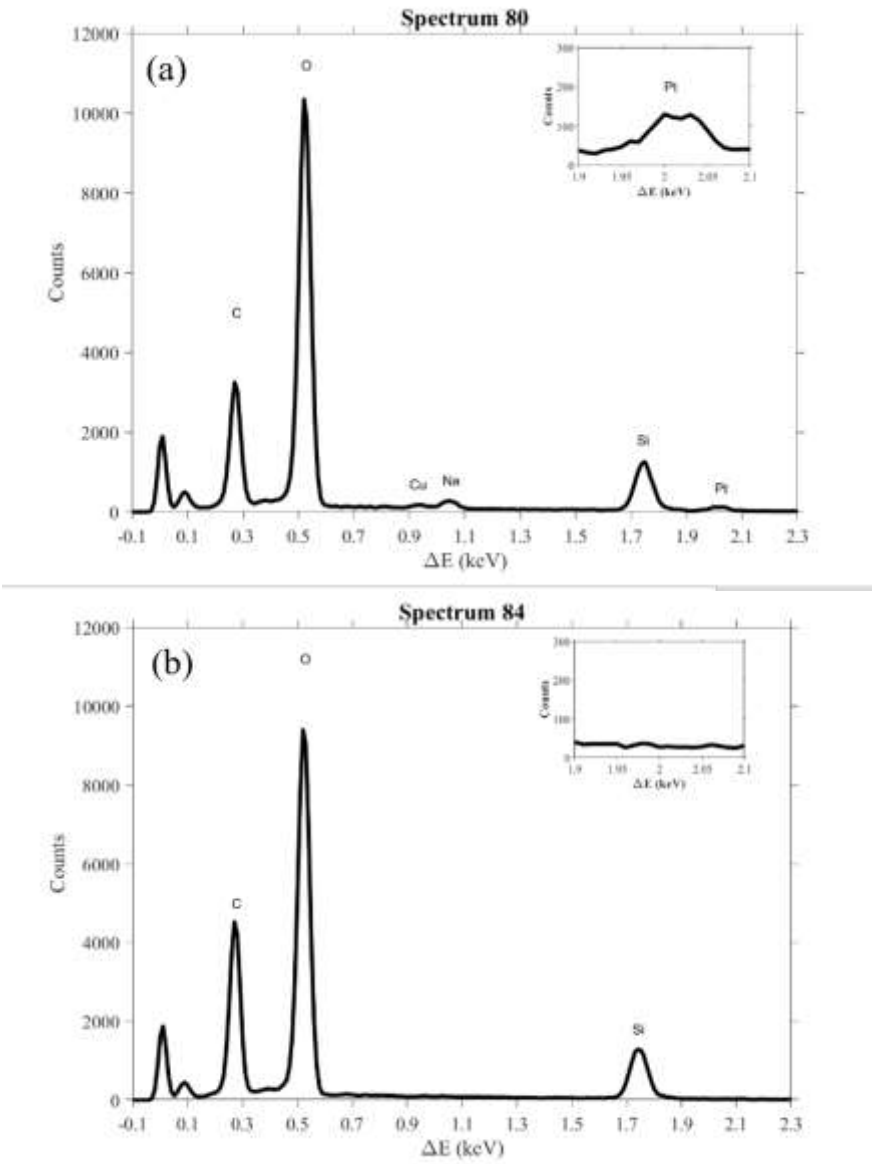

Figure 23: EDS spectrum of (a) point 80 (b) point 84 as labeled in Figure 22)

3.4 Summary

Sheets of ACS monolayer graphene pre-transferred to SiO_2/Si substrate were successfully modified with gold- and platinum nanoparticles, respectively using air-brush spraying method. Upon increasing numbers of solution deposition, both samples experience a decrease in hole concentration, increasing the sheet resistance of the

material. As ammonia is generally an electron donor, increasing the electron concentration with these solutions have similar effects on the sensing response. Due to previous successes of other groups, it is assumed that this technique for gold- and platinum-decoration may not be as beneficial for ammonia sensing.

After heating the sample to observe the material under SEM magnification, it was observed that organic residue may have contributed to the electronic response of the material. For this reason, it may be of interest to repeat the experiment with subsequent residue removal in-between measurements to eliminate the residue contributions. This will prove difficult as prolonged heating may also affect the material's electronic properties as is shown in the next chapter.

4 Characteristics of Graphene after Thermal Annealing

4.1 Experimental

4.1.1 Thermal Annealing Processing

Two 1-by-1 cm samples (NAE0013 and NAE0030) of monolayer CVD graphene on SiO_2/Si substrate samples (ACS Materials) were each split into 4 ~ 0.5-by-0.5 cm samples (NAE0013a-d and NAE0030a-d). Each sub sample was heated on a hotplate in ambient air at one temperature for two hours. A third sample (NAE0038a-d) was used to repeat the NAE0013a-d series and the data were later combined to form a complete set.

4.1.2 Raman Spectroscopic Analysis

Raman spectra were taken before and after the heat treatment to monitor any changes in the samples. The Raman microscope was a Renishaw InVia microscope with a 514 nm excitation laser and a 100x magnifying lens. Spectra were analyzed using the WiRE 4.1 built-in data analysis software. The baseline was removed using "intelligent polynomial" algorithms and peaks were fitted using a single Lorentzian line-shape.

4.1.3 Hall measurement and van der Pauw measurements

Hall measurement and van der Pauw measurements were performed using indium solder applied to the four corners of the sheet. For these measurements, a 3 kG magnetic field was applied at room temperature. Each sample was measured three consecutive times under the same conditions and the data were averaged upon confirmation that the measurements were repeatable.

4.1.4 SEM Imaging

SEM images were obtained using the secondary electron detector of a Zeiss Gemini SEM 500 operated at 5 kV to eliminate contrast reversal [68].

4.1.5 RF Impedance Characterization

To observe RF characteristics, a device was manufactured using ACS graphene on SiO_2/Si substrate and gold/chrome conducting layer. The complex reflection coefficient (Γ) of the device was measured using a virtual network analyzer (KEYSIGHT E5071C) such that changes in material properties could be observed. Γ was measured across a swept frequency range of 0.1-20 GHz for each annealing temperature. To eliminate changes due to processing, the annealing was performed on the same device. Heating was done in ambient air on a hotplate and in a sequential manner at 30 min. intervals for temperatures of: as-manufactured (25-), 100-, 200-, 250-, 300-, 350-, 400-, 450-, and 500°C. After each annealing session, the sample was allowed to cool in air for ~5 min. to eliminate any temperature effects during measurement.

4.2 Charge Transport Characteristics

While annealing was performed at 200-500°C in 50°C increments, one temperature per 0.5-by-0.5 cm piece, certain pieces were unable to be soldered for various reasons. Data at temperatures 200- and 300°C are not present in the following results. Further, the 400- and 500°C pieces were repeated with a new sample (no thermal history) so that the transport measurements could be performed. The data at 25°C represents an as-grown graphene sample with no thermal treatment as a reference. While

NAE0013d (heated at 540°C) showed a return to the original line, the data was not able to be repeated with NAE0038d and was therefore removed from the data.

Figure 24 shows the results of the Hall mobility measurements. The Hall mobility measurements appear to show a linear decline from ~1640 $cm^2\ V^{-1}s^{-1}$ in the as-grown sample to 1004 $cm^2\ V^{-1}s^{-1}$ in the sample annealed at 350°C. At 400°C, there is a rapid decline from 1004 to ~80 $cm^2\ V^{-1}s^{-1}$ and the mobility is not recovered in the 450-500°C measurements.

The van der Pauw measurements provide information on the material sheet resistance. The data are plotted in Figure 25. From 25°C to 300°C there is a drop from 568 Ω/□ to 310 Ω/□ and a further drop to 304 Ω/□ at 350°C. Beginning at 400°C, there is an increase peaking at 450°C with a value of 21.2 kΩ/□ after which the value drops to 3283 Ω/□. Again, data from NAE0013d (540°C) show a return to a sheet resistance of 452 Ω/□, but the heating process could not be repeated on NAE0038d. The van der Pauw method determined the charge carriers are holes.

From the mobility and sheet resistance, the hole concentration of the sheet can be calculated. Figure 26 shows the concentration of holes in the material as related to the annealing temperature. An increasing linear relationship is shown between 25°C and 350°C with a three-fold increase over that range. Again, 400°C marks a break in the linear trend with the beginning of a sharp decrease. The trough is at 450°C with a value of $6.77 \cdot 10^{12}\ cm^{-2}$, only $0.07 \cdot 10^{12}\ cm^{-2}$ higher than the pristine sample. There is a slight recovery to the trend-line at 500°C. Yet again, NAE0013d showed a complete recovery to the trend-line, however, the data could not be measured for NAE0038d and are removed due to irreproducibility.

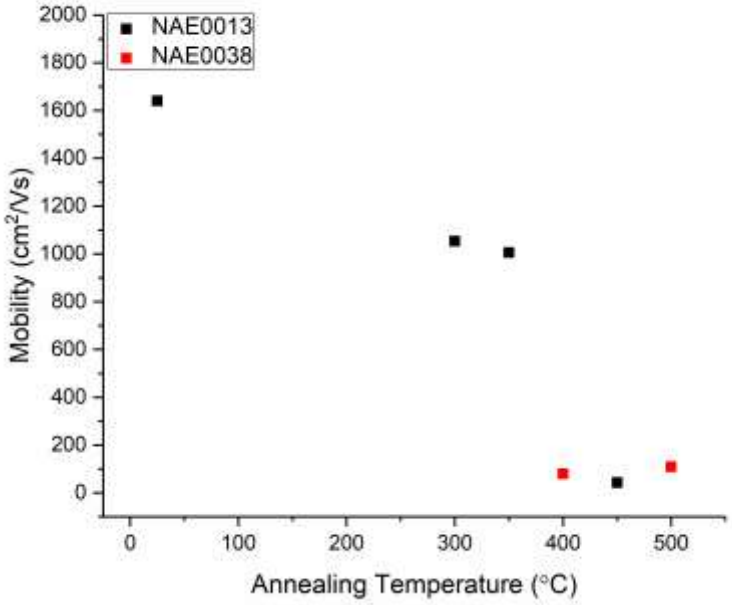

Figure 24: Mobility of annealed CVD monolayer graphene (measured at room temperature)

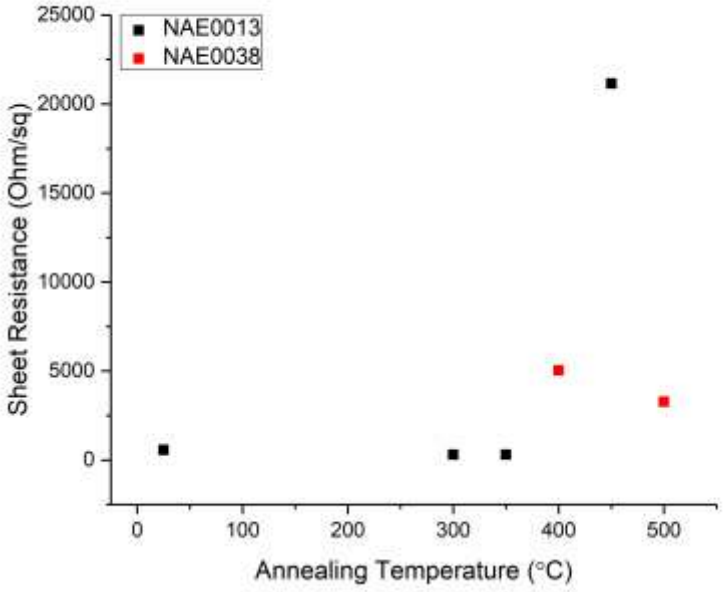

Figure 25: Sheet resistance of annealed CVD monolayer graphene (measured at room temperature)

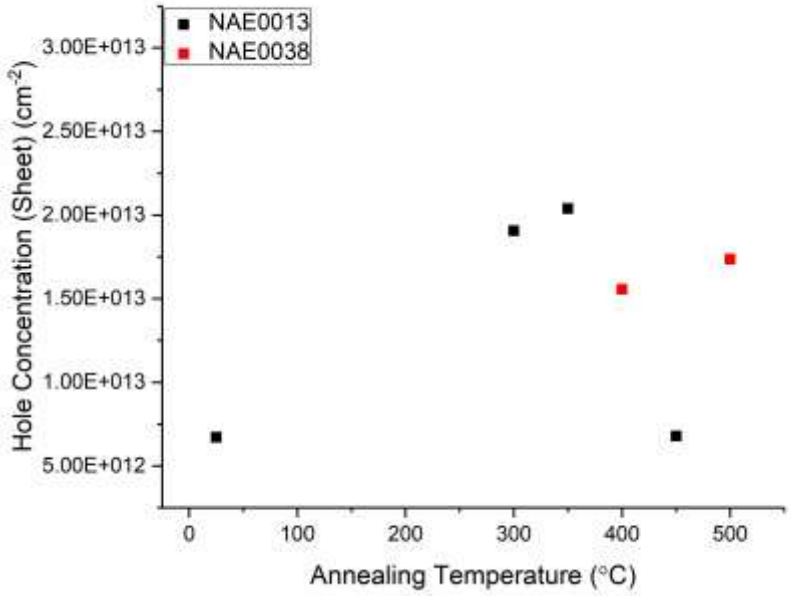

Figure 26: Sheet carrier concentration of annealed CVD monolayer graphene (measured at room temperature)

4.3 Raman Characteristics

For better visualization of the spectra, all spectra from the same sample were averaged together and normalized to the highest point so that relative peak heights can be compared between samples. The results are shown in Figure 27 with offset data to easily visualize the progression of the spectra with annealing temperature. The pristine graphene shows a very typical Raman spectrum with little or no D peak present. The 2D/G peak intensity ratio is nearly 3.5 indicating monolayer with high quality. Upon heating, the spectra show a broadened G peak and shoulders. Annealing at and above 400°C generates a strong D peak and a prominent D` peak.

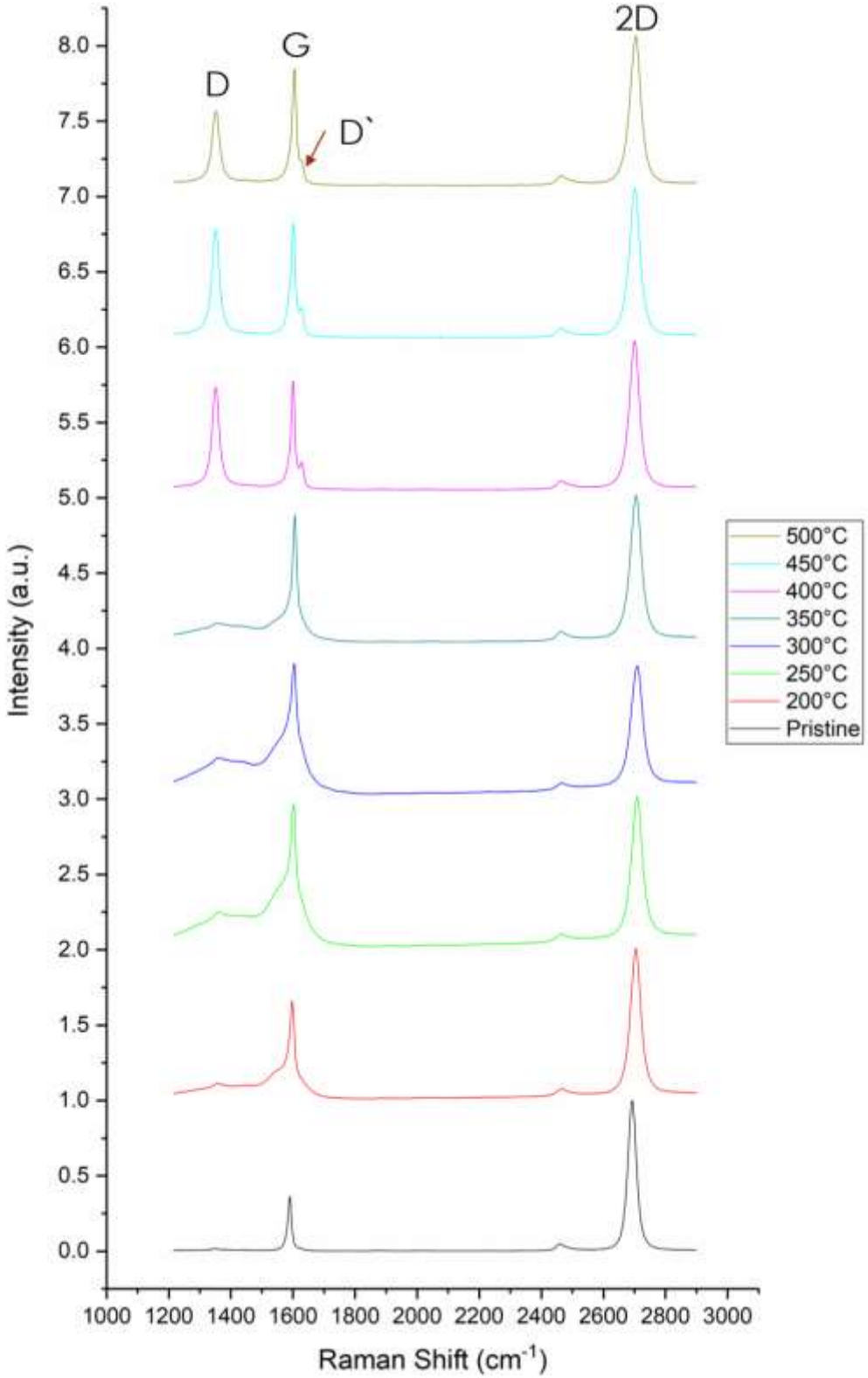

Figure 27: Averaged Raman spectra of annealed monolayer CVD graphene (measured at room temperature)

In general, the 2D/G ratio is lower in the annealed samples than the pristine graphene. However, one sample (NAE0038c) treated at 450°C showed certain locations where the 2D/G ratio was similar to that of pristine graphene (not shown.) Lower annealing temperatures provide a rather broad plateau between the D and G peaks. To analyze the D peak, this plateau was considered part of the baseline which was removed prior to fitting the D and G peaks. The presence of the D` peak near 1620 $cm^{-1}$ is made obvious at temperatures at and above 400°C as it protrudes into a noticeable unique peak. Below 400°C, when the D` is present, it is relatively weak and is hidden within the shoulder of the G peak. There is a noticeable upshift in the 2D peak position with increasing annealing temperature.

The position of the G peak and 2D peak can be useful in determining mechanisms of property changes in graphene [66], [71]. For temperatures below 350°C, there is a nearly linear relationship between the relative G position and relative 2D position (calculated as $[G - G_0]/G_0$ and $[2D - 2D_0]/2D_0$ where G_0 and $2D_0$ are the average pristine graphene peak positions) with increasing annealing temperature showing higher relative change in both 2D and G peak positions. At and above 350°C the data show a new linear trend, however, the temperatures are out of order (Figure 28.) Lines were fit using a bisquare[2] weighting technique which weighs severe outliers with no weight. The "As Received" data was not included in either fit and is given as reference only. Fitted lines are shown in blue representing the lower temperature range of 200-300°C (slope of 0.54) and in red representing the higher temperature range of 350-500°C (slope of0.48.)

[2] This was performed using MATLAB *robustfit* function with default parameters.

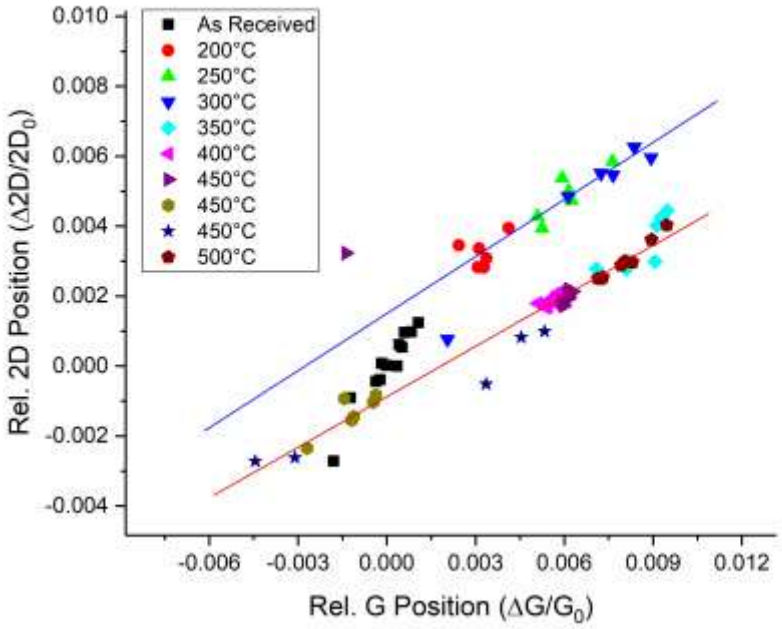

Figure 28: Relative 2D position vs. Relative G position for annealed monolayer CVD graphene (measured at room temperature)

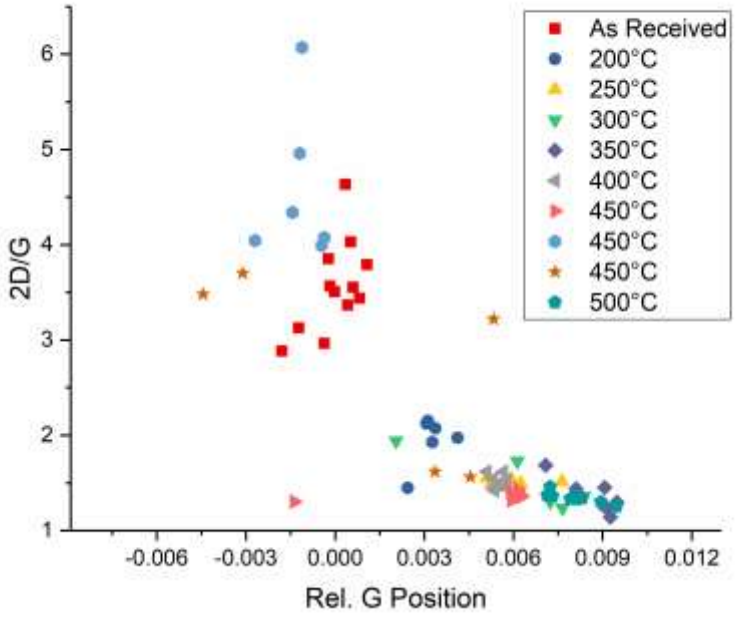

Figure 29: 2D/G intensity ratio for annealed monolayer CVD graphene (measured at room temperature)

As the 2D intensity (peak height) to G intensity ratio is typically used to describe the quality of the graphene, these values are also plotted as related to the relative G position. These results are shown in Figure 29. The 2D/G ratio declines from what ~3-4 in the as received graphene to ~2 at the lowest annealing temperature. Increased temperature seems to slightly decrease the ratio to ~1.5 for temperatures up to 350°C. At 400°C, the ratio appears to slightly increase and subsequently decrease for one sample at 450°C (pink triangles in Figure 29) and 500°C. Interestingly, one 450°C sample (light blue hexagons) shows a higher 2D/G ratio than the as-received samples. Yet another 450°C sample (orange stars) showed a mixed behavior, between the light blue hexagon and the pink triangle 450°C samples.

The D/D` ratio was plotted versus the G peak position. These data are shown in Figure 30. The D/D` value was obtained from the peak height of the fitted Raman data. This ratio can be used to identify the type of defect present in the graphene sheet. Higher values correspond to a more severe change in the lattice. From the as-received sample to 350°C annealing show very low values of D/D` indicating only low-level defects. Annealing at 400°C, however, shows an increase in the D/D` ratio. The data for the 450°C measurements are scattered between values of 5-6 and ~10. The sample annealed at 500°C show a value of ~6.

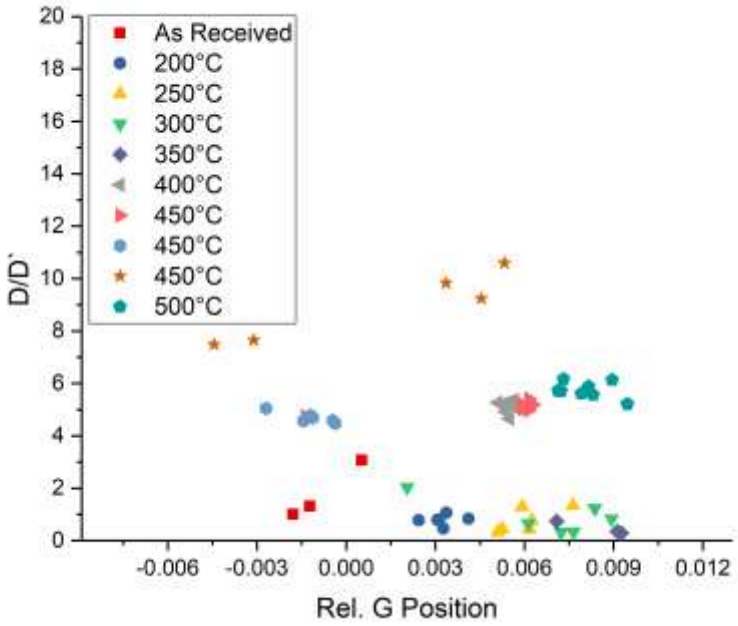

Figure 30: D/D` intensity ratio for annealed monolayer CVD graphene (measured at room temperature)

4.4 SEM Images

Pristine graphene (shown in Figure 31a) shows a few notable features. In general, the entirety of the image is expected to be single-layer graphene. The bright band to the bottom left of the image, along with the irregular region surrounding the bright round feature on the right of the image represent the substrate without graphene coverage. In-other-words, these are areas where graphene may have been damaged during some processing step. The border of these regions represents the edge of the graphene sheet. As expected from the secondary electron contrast, the edges of graphene are brighter. The bright round feature on the right is copper remaining from the growth of the graphene sheet. The high curvature of the copper particle is responsible for the high intensity in the image. The two darker stream-like features are expected to be domain boundaries (called

grain boundaries in bulk materials) [72]. These boundaries form during the growth process when graphene nucleation sites impinge on one another or from the underlying copper film. Any horizontal wave-like features near the top of the image represent corrugation of graphene on the substrate. Scalebars in Figure 31a-h are comparable.

When graphene is heated to 200°C for two hours, the SEM signal changes. One representative image of this type graphene is shown in Figure 31b. In this image, there is, by coincidence only, complete coverage of graphene on the substrate. There do not appear to be many regions related to high topography. Brighter regions in the image may correspond to electron dopants adsorbed to the surface. Oxygen is a known, and abundant in the environment, to be an electron donor. These excess electrons may repel the incident electrons in localized regions around doping sites, increasing the apparent secondary electrons in the image. Again, the darker regions appear to be the domain boundaries.

Upon 300°C heating for two hours in air, a new contrast arises. This new contrast is shown in Figure 31c. In the image, high contrast regions appear near domain boundaries. This high contrast is expected to be due to charging effects. Similar to the substrate removing electrons from graphene at low acceleration voltage leading to increased contrast due to electron-electron repulsion, doping of graphene by electron acceptors would cause increased intensity at doping locations. Interestingly, the number of domain boundaries also seem to increase. This observation will need further evidence by examining the full sample surface before and after annealing at 200°C and 300°C.

A noticeable increase of domain boundaries is shown upon a 350°C, two-hour annealing procedure shown in Figure 31d. Again, high intensity areas are expected to be

due to doping. This annealing procedure shows a larger area of doped graphene than lower temperatures and appears to affect areas within the domains. This would imply a higher level of doping and possibly oxidation. Oxidation could have a similar effect as doping on the image contrast due to a loss of conductivity and increased charging. The bright spherical regions are related to residual copper from the growth film. Areas around the copper seem to be surrounded by areas of high doping. This observation is consistent with adsorbed species being preferentially positioned near high defect regions. There also appears to be a corrugation-related contrast over the entire image. Due to the difference in corrugation angle with respect to the raster direction of the electron beam, this is not expected to be related to charging or averaging effects of the imaging process.

Figure 31e shows an interior portion of the graphene sheet annealed at 400°C. Based on this image, annealing at 400°C shows fewer domain boundaries than were found in the 350°C annealed sample, yet some finer boundaries are still present. There is also a smaller area associated with corrugations in the sheet: perhaps some are present on the right-hand side at ~45° angles to the horizontal. Darker areas in the image may be due to thicker growth. It is noted that the darker areas have formed around copper from the growth substrate. It is possible that nucleation sites on the copper film promoted thicker growth than the nominal monolayer graphene in most areas of the sample.

Two images are presented from the 450°C annealed graphene. In the first, Figure 31f, the image was taken in the interior portion of the graphene. In this image, most of the surface has a high intensity indicating doping. The dark circular regions may be due to oxidation [49]. Above 400°C, oxidation of graphene can be expected. Ref. [49] describes oxidation pits that result from the oxidation of graphene. Flake-like regions are thicker

regions of the graphene. This observation is based on the relative number of pits present in these areas. Two- and three-layer graphene does not show substantial pitting until >500°C [49]. The second image of the sample annealed at 450°C is shown in Figure 31g and shows the domain structure of the material. The domains are relatively large when compared to the sample annealed at 350°C. Again, the flake-like structure in the upper left corner is expected to be multilayer graphene based on the contrast and the relatively low number of oxidation pits present there.

The sample annealed at 500°C also has severe damage near the edge of the sample (not shown.) The interior of the sample, however, shows a high density of domain boundaries (Figure 31h.) The remainder of the surface appears to be completely covered by a dopant. While the surface appears rough, there do not seem to be any marks attributed to corrugation of the sheet. Unfortunately, it is unclear whether this sheet is continuous, or if it shows a separation as was seen at 400°C.

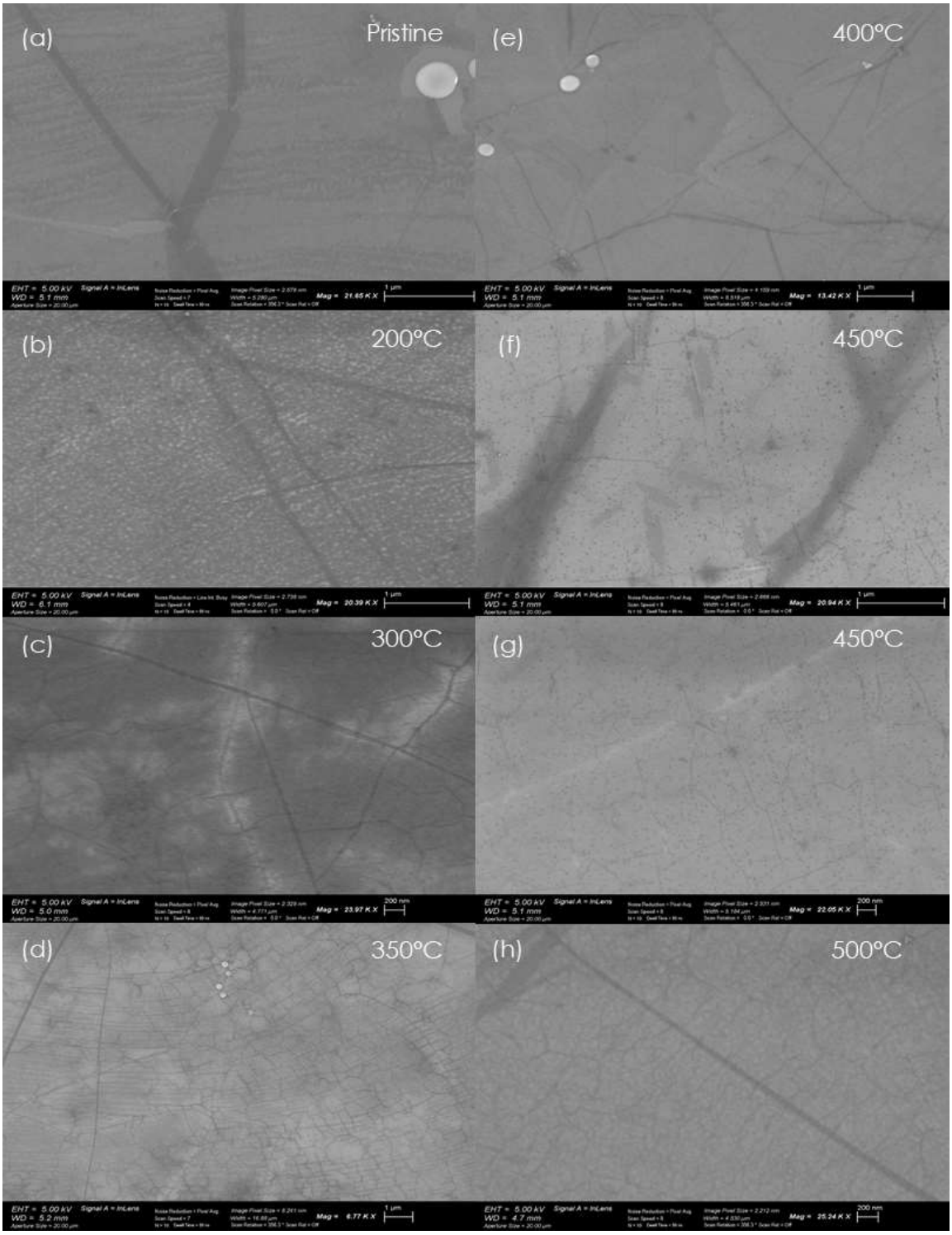

Figure 31: Progression of SEM images with annealing temperatures.

4.5 RF Impedance Characteristics

The normalized impedance of the device shows two unique regimes with a transition point over this set of temperature ranges. The Smith chart showing the impedance in given in Figure 32. These measurements were performed on one device to represent many devices on the same wafer. All twelve devices with the same configuration show the same trend. For this reason, these data are considered reliable and repeatable given that all processing and parameters are identical.

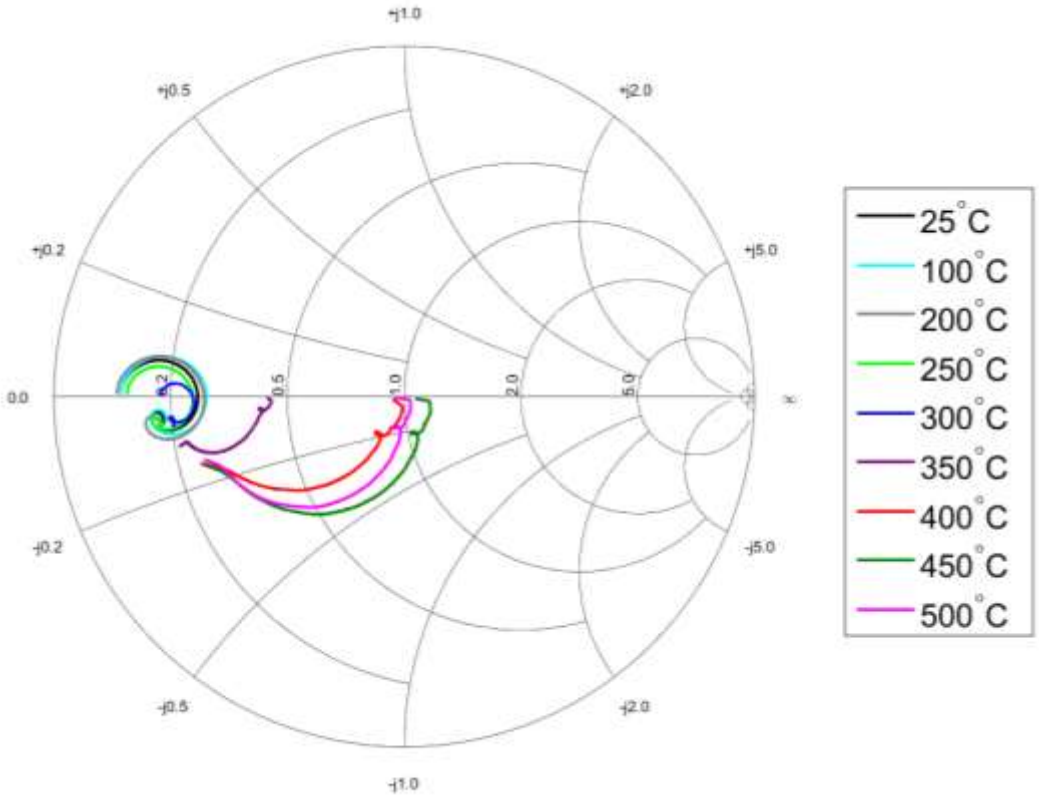

Figure 32: Smith chart of Γ for monolayer graphene at various (sequential low-to-high) annealing temperatures

Annealing temperatures at and below 300°C show similar profiles on the Smith chart. At low frequency, the device shows inductive behavior until a certain frequency

after which, the device shows capacitive behavior. The resistance in this range is relatively low. At 350°C, there is a change in behavior. At this temperature, the device shows only capacitive reactance (i.e. below the main horizontal) for all frequencies measured. Annealing at 400°C and above show similar behavior, but shifted to higher resistance. At 500°C there is a slight recovery of the resistance to lower values.

4.6 Discussion

Oxygen can dope graphene with additional holes (especially in the presence of water vapor [46].) This can be achieved in various ways based on the state of the material and the environment. Adsorption tends to occur near defect sites. In some cases, charge transfer is possible with oxygen accepting electrons from graphene. Some examples of oxygen position are shown schematically in Figure 33. In the figure, carbon is dark gray, oxygen is red, and hydrogen terminates the graphene edges (white). From the figure, it is apparent that the adsorption mechanism can be very complex. For this reason, adsorption will be discussed in a qualitative manner.

Experimentation shows the hole concentration increases with increased annealing temperature until 400°C, where a decrease begins. Further, there is a change in G peak and 2D peak positions with changes in doping, strain, and chemical changes to graphene. Each mechanism has a slightly different and independent effect on the G and 2D peak positions. Therefore, a parameter has been used to determine the primary source of the shift by plotting the 2D position as related to the G position and acquiring the slope. The slopes of the fitted lines in Figure 28 are quite similar 0.54 and 0.48 for the low and high temperature fitted lines respectively. This would indicate that the mechanism responsible

for the shift is similar. One important slope to rule out is that for strain. This typically occurs between 2.02 - 2.44 depending on the orientation of the lattice [73]. As neither of the slopes are within or near this range, the changes in the Raman signal are not likely due to strain. Large variations exist for the doping mechanism's slope. Ref. [73] states a slope of 0.75±0.2, while Ref. [66] finds a value of 0.6. Discrepancies in slope could be the result of the annealing process, namely, whether the annealing was performed in vacuum or in open-air. As the slope values obtained from the previous section are reasonably close to the value found in [66], it is appropriate to conclude that the change in the 2D and G positions are due to hole doping. This is also supported by the fact that oxygen in the air readily accepts electrons from the graphene and is aided by the presence of water [66]. This combination of data show that from 200-350°C comprise one regime of doping, likely caused by oxygen and water vapor doping of graphene.

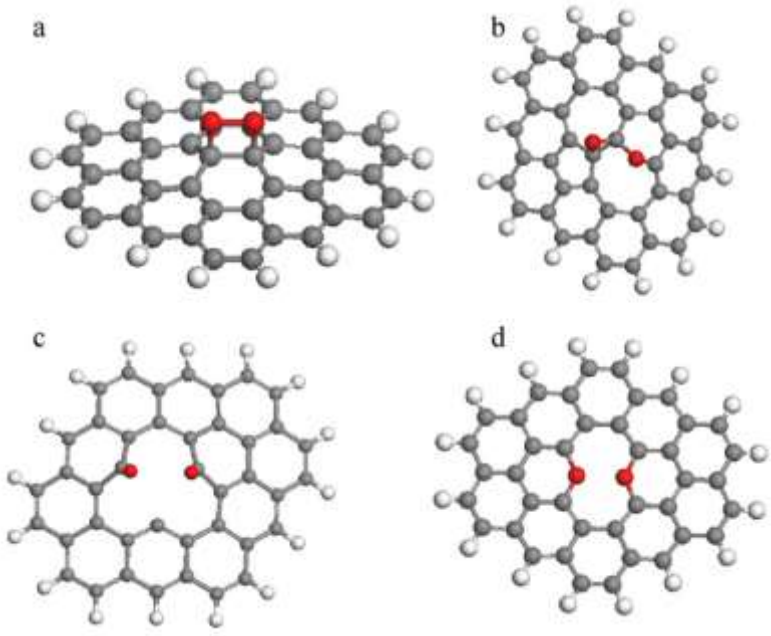

Figure 33: Adsorption of oxygen on pristine graphene (a), Stone-Waals site (b), single carbon vacancy (c), and double carbon vacancy (d [74]*).*

There is a dramatic electronic change in the material near 400°C based on the transport properties. For instance, the hole concentration decreases starting at 400°C and continues to decrease at 450°C. At temperatures at and below 350°C, the D/D` ratio is relatively low and constant, implying low-level defects. However, 400°C marks a change in the D/D` ratio as it increases to ~5.5 indicating a change in the graphene structure. The higher value of the D/D` ratio continues for temperatures above 400°C as-well. The higher values of the D/D` ratio correspond to the highest sheet resistance, lowest hole concentration, and lowest mobility samples. It is possible that oxygen adsorbed to the graphene is activated and attacks graphene at certain temperatures. The vacancy left behind by the etching of graphene could be the source of the high D/D` values.

SEM images support a fundamental change in the material based upon annealing temperatures. At annealing temperatures at and below 300°C, there appears to be an increased area of doping which progressively migrate and congregate near the high-energy domain boundaries. It is expected that these areas continue to grow to the interior of existing domains after the saturation of the existing domain boundaries. There is a dramatic change in the SEM images over this temperature range although the most change occurs in the 350-450°C. In this range, the number of domain boundaries has increased from the lower temperature range and the structure begins to change. This may be due to the concentration of the doping species on the surface. As the number of species increases, there may exist a localized stress in the graphene causing the sheet to form new domains in the structure. With temperatures reaching ~450°C, there begins to be a change in the conductivity of the sheet at certain pit-like locations. These pits could be related to a higher-degree of bonding, (i.e. more chemical character) than simple

doping or could even represent etching of the graphene by oxygen. The increase of domain boundaries and pitting could be responsible for the increase in sheet resistance as-well-as the large number of defects predicted from the Raman spectra.

The RF data supports a transition at or near 350°C based on the change in the reflection coefficient. While this data is not exactly comparable to the other results with the lower annealing time and sequential heating, it is apparent that the device becomes more capacitive. The only way to change the capacitance of this device is to change the permittivity of the graphene. A change in permittivity marks a fundamental change in the material.

4.7 Summary

Annealing temperatures (T) around 300-400°C show interesting changes in graphene's electronic response. This phenomenon was observed in transport measurements, Raman spectra, SEM images and RF characterization. In each case, observations point to minor doping effects for temperatures $T < 300$°C, transitioning in the 350-400°C range, and structural damage for $T > 450$°C. While the doping effects show only minor changes in the electronic properties, extreme changes occurred when the graphene structure was altered. Hall measurements may not be appropriate under the circumstances where structural damage has occurred. More evidence is needed to truly support the assumptions of uniform surface when performing the Hall measurements.

With reference to the sensing capability of the material, structural damage is not always detrimental to the sensitivity of the device. Higher energy defects can be locally stabilized via a gas molecule adsorbing to the surface. If defects are large enough to

destroy the electrical properties, the defect density may be too high to be of use. There must be an optimum density and distribution of defects such that the adsorption of gas is promoted while the electronic behavior of the material is predictable. The optimum defect density or distribution is not known for the current application. If the defects are able to be controlled, a study can be performed to identify the optimum distribution and density.

5 Characteristics of Graphene after Oxygen Plasma Etching

Graphene nanoribbons (GNR) show promising use in field-effect transistors (FET) due to the ability to engineer a bandgap. There can also be an enhancement in FET performance by placing GNRs in the trenches of the FET [75]. When sensors are developed in the FET configuration, graphene can be used to enhance the effect.

The strong dependency of the GNR width to the band-gap opening [76] has allowed a variety of techniques for GNR fabrication to develop. Use of oxygen plasma etching, combined with standard lithography, offers advantages in terms of large-scale integration. Experimentation reveals, however, that an electrically inactive layer (EIL) is created near GNR edges due to the generation of localized edge states at the edges of the graphene [77]–[81]. The focus of this work was to determine the width of the EIL of GNRs using Raman spectroscopy/mapping. These results were compared with scanning microwave microscopy (SMM.)

5.1 Experimental

Graphene grown on a 100 μm copper foil (Graphene Supermarket) was transferred to a SiO_2/Si and Au/SiO_2/Si substrates. Photolithography and oxygen plasma at 2 Watts was used to pattern the graphene into ribbons on each of the two substrates.

Raman spectra and maps were obtained using a Renishaw InVia confocal Raman microscope with a 514 nm laser operated by Renishaw WiRE 4.1 data collection and

analysis software. The spectrometer was set to 1800 mm^{-1} grating using x100 objective. Raman images were obtained where each pixel corresponds to one acquisition point on the sample. Using a motorized sample stage which moved autonomously in a raster pattern at each 0.1μm increment in each the x and y directions, acquiring signal for 3s at each position, a spatial Raman 2-D map was obtained. Upon completion of the 2-D map, all spectra corresponding to each (x,y) position were analyzed using the WiRE 4.1 built-in data analysis software. The baseline was removed using "intelligent polynomial" algorithms. Three prominent peaks are present with graphene. Each of these peaks is representative of a specific vibrational mode. A single Lorentzian peak was used to fit each of the three peaks in the spectra as is common practice for monolayer graphene [45], [57], [58]. The peaks were only constrained to have a positive intensity.

Atomic force microscopy (AFM) was used to visualize the graphene ribbons topologically. AFM and SMM were obtained using an Agilent 5420. SMM records the complex input reflection coefficients (Γ_{in}) through a different channel to assure complete de-coupling from the surface morphology. The sharp tip-induced enhancement on the local EM field makes Γ_{in} reflect mainly the EM properties of the sample underneath the probe. SMM has been recently applied to investigate the electrical properties and surface impedance of grain boundaries in ferrites [82], and micro-patterned graphene [83], [84]. To enhance the SMM imaging contrast, one graphene grating was fabricated on an $Au/SiO_2/Si$ substrate.

5.2 Results and Discussion

Figure 34a presents the topological image of the as-pattered graphene ribbons. The higher intensity areas correspond to the graphene locations, while lower intensity represent the substrate material. Figure 34b is a schematic representation of the grating structure where the dashed red lines indicate the EIL and the honeycomb pattern represents the graphene.

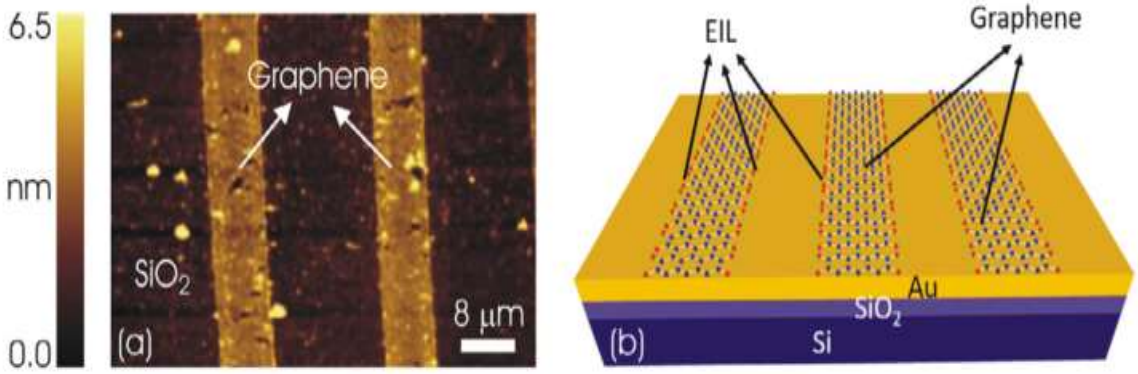

Figure 34: AFM topology of graphene ribbons on SiO_2/Si substrate (a) and schematic of graphene ribbons on Au/SiO_2/Si substrate (b) [85]

As mentioned in Chapter 2, the 2D/G intensity ratio from the Raman spectrum is commonly used to determine the graphene quality and is also used in this case to verify the location of the graphene (Figure 35). The 2D/G ratio map based on the intensity of the fitted peaks is a clear indicator of the spatial location of the graphene. This ratio is important as normalization to the G peak allows for better comparison between points. A 2D/G value of 1.5 is used to indicate the high-quality monolayer graphene. Since Raman signal can be given off by any location within the laser spot, it is assumed that the location where the signal is half of the nominal peak value is the location of the edge. The

2D/G value of 1.5 was chosen to represent the graphene edge because it is roughly between the maximum (3) and minimum (0) values for the 2D/G shown in Figure 35a.

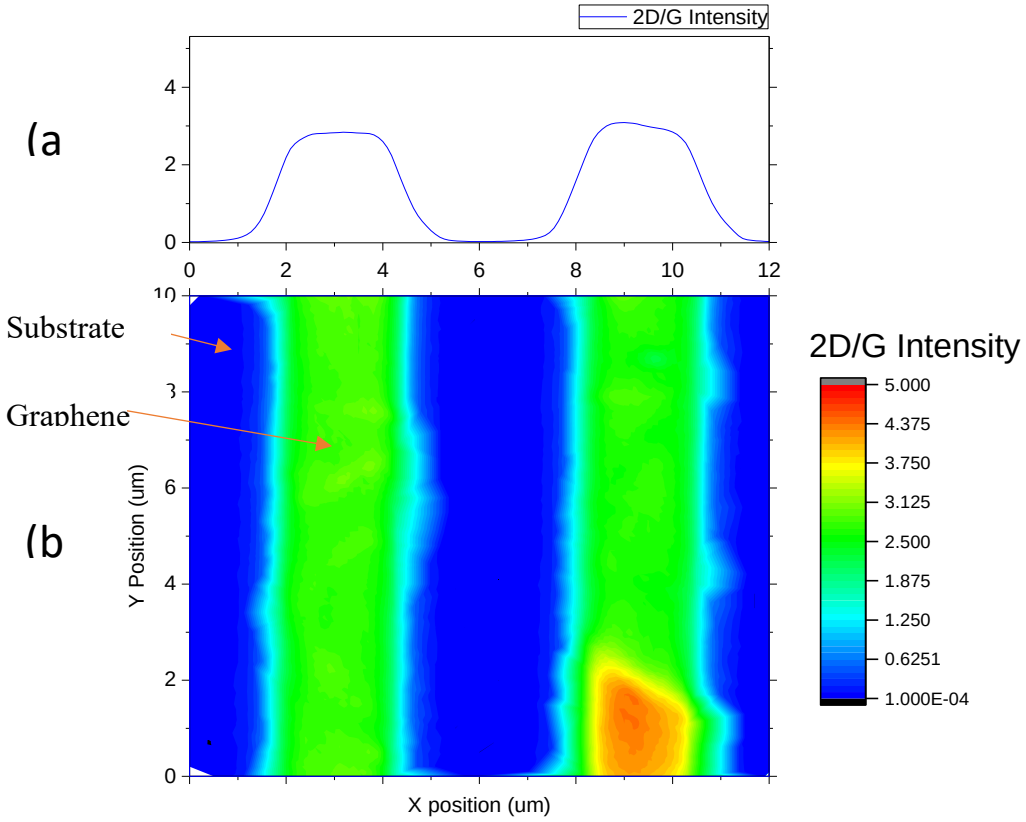

Figure 35: *(a) Profile of the average of all data at each x position as an aid in visualizing (b, a map representing spatial Raman intensity of the 2D/G peak in two graphene ribbons separated by bare SiO2/Si substrate.*

Figure 36 a and b present two point-spectra, one at the edge of a ribbon and one at the center of a ribbon for better visualization. There is a noticeable increase in the D intensity and noticeable decrease in the 2D/G intensity ratio in the spectrum taken at the edge relative to the center of the ribbon. These observations are consistent with an increase in defect density near the edge of the ribbon. The D peak intensity line profile

and map are shown in Figure 37. An important note is the higher D intensity near the edges of the graphene ribbons, which is expected due to the broken symmetry and either dangling bonds or defects resulting from oxygen plasma etching.

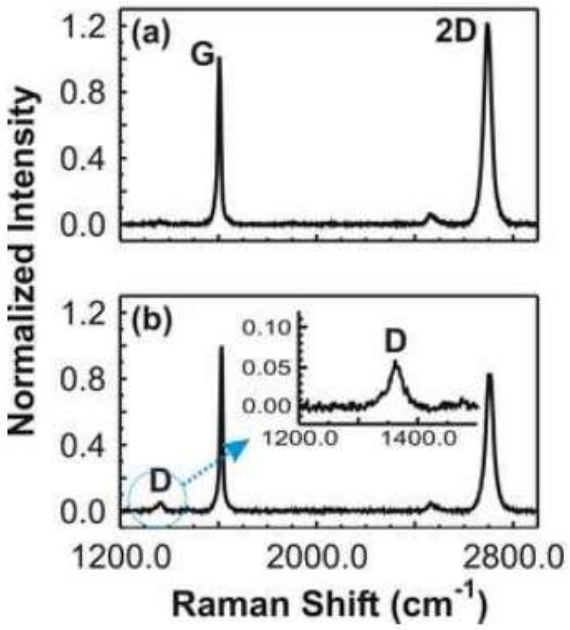

Figure 36: Raman spectrum obtained (a) near center of graphene ribbon. (b) near edge of ribbon.

The D/G ratio map is shown in Figure 38c and -d. The normalization of the D peak to the G peak shows where the highest defect concentration (spatially) is located. Due to the lack of a G peak in the substrate, the D/G ratio had a threshold such that only values in locations which corresponded to 2D/G ≥1.5 are present, effectively masking all "non-graphene" locations. The images clearly show that the highest defect concentration occurs on the edges of the graphene stripes.

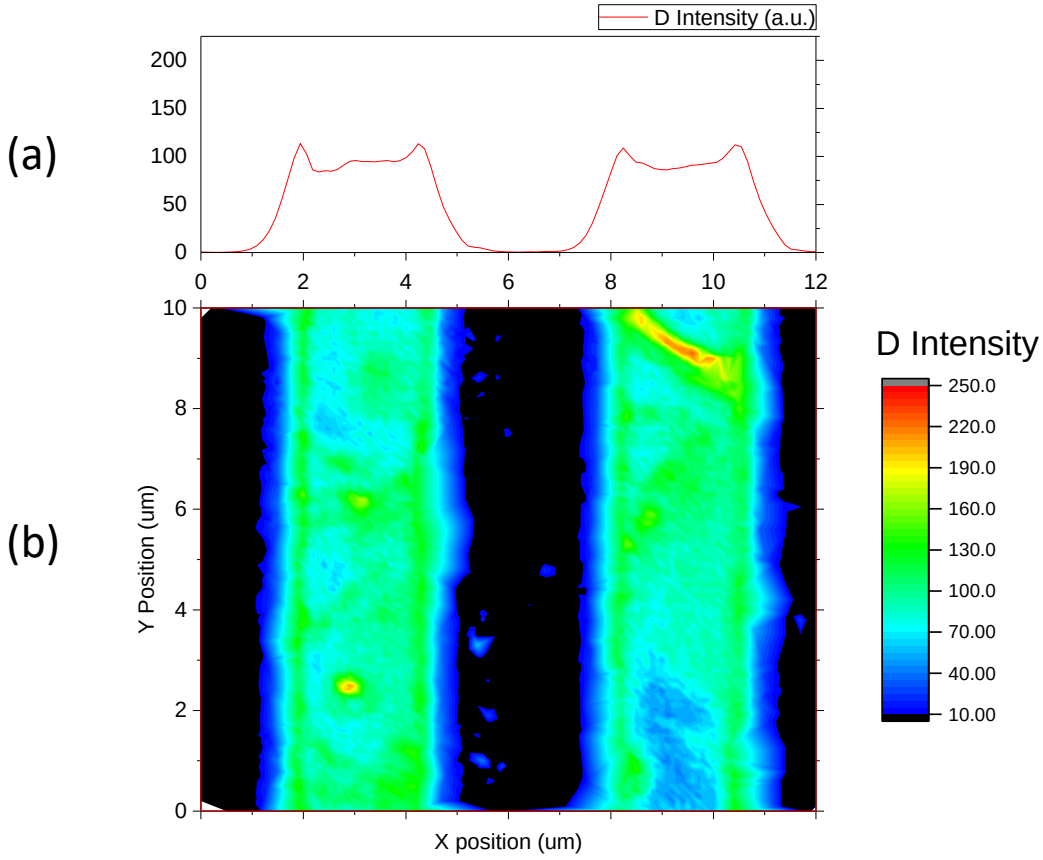

Figure 37: (a) Profile of the average of all data at each x position as an aid in visualizing (b), a map of Raman D peak intensity on two graphene on SiO2/Si substrate.

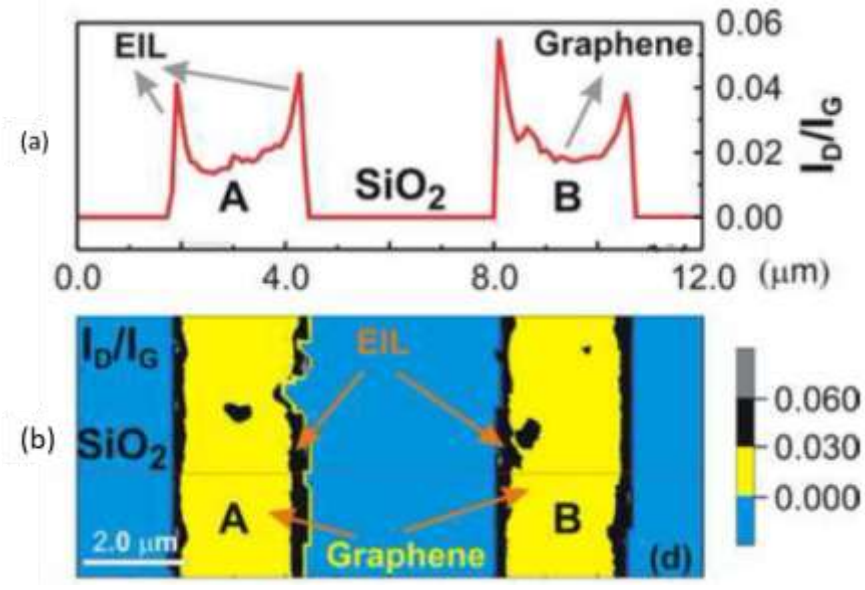

Figure 38: (a) line-scan and spatial map (b) of the I_D/I_G Raman signal [85].

A ratio between the D peak and the G peak can be used to approximate the defect-defect distances [54], [57], [58], [86]. When the average inter-defect distance is high, the D/G ratio is small. As defects are introduced, the average inter-defect distance decreases and D/G ratio increases. It was reported that the D/G ratio increases to a maximum at inter-defect distance ~4 nm [55], [57], [58], [86] and then decreases with smaller inter-defect distance due to increase in amorphous carbon phase [55], [57]. Assuming the average defect distance is greater than 4 nm, increase in the D/G intensity ratio is attributed to higher defect concentration and is approximated using Equation (5)

$$\frac{I_D}{I_G} = \frac{C(\lambda)}{{L_d}^2} \tag{5}$$

where $C(\lambda)$ is a parameter which depends on the laser excitation energy, L_d is the inter-defect distance, and I_D and I_G are the intensities of the D and G peaks respectively. For 514 nm excitation, $C(\lambda)$ is 102 nm^2 [55]. The L_d values were calculated using Equation (5) and are plotted in Figure 39. The masked D/G ratio was used to ensure that only graphene areas were analyzed. In this case, the lower L_d values correspond to higher defect concentration. For this reason, the color scale in Figure 39 uses red as high defect concentration rather than high L_d values.

The G peak full width at half maximum (FWHM) is also reported to increase with defect concentration [57]. For this reason, it is viewed both the D/G intensity ratio along with the FWHM(G) to ensure the defects are truly present. This analysis was performed using the masking of data below 2D/G =1.5 (in the same manner as the D/G ratio) and is thus, only performed on graphene regions. The result of the masked FWHM(G) is shown

in Figure 40. The FWHM(G) is somewhat larger near the edges of the graphene which is again expected due to the processing methods used and the lack of symmetry.

See from the above Raman point spectra, line-scan profiles, and mapping images, the existence of the EIL due to the presence of defects (introduced by the oxygen plasma etching) is consistently observed. The width is in the range of hundreds of nanometers. Raman imaging has been the primary technique to probe the EIL, but is limited by its poor spatial resolution (~ 800 nm) [80].

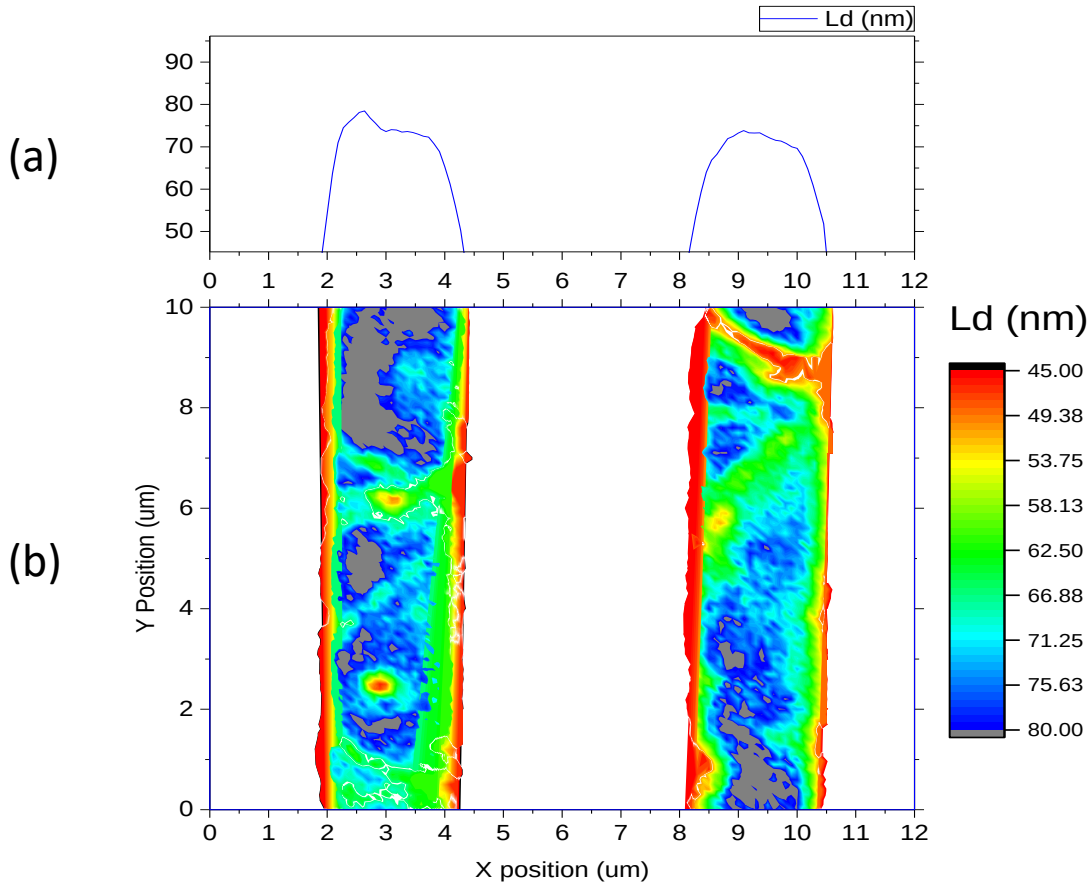

Figure 39: (a) Profile of the average of all data at each x position as an aid in visualizing (b), a map representing calculated inter-defect distance in the graphene regions

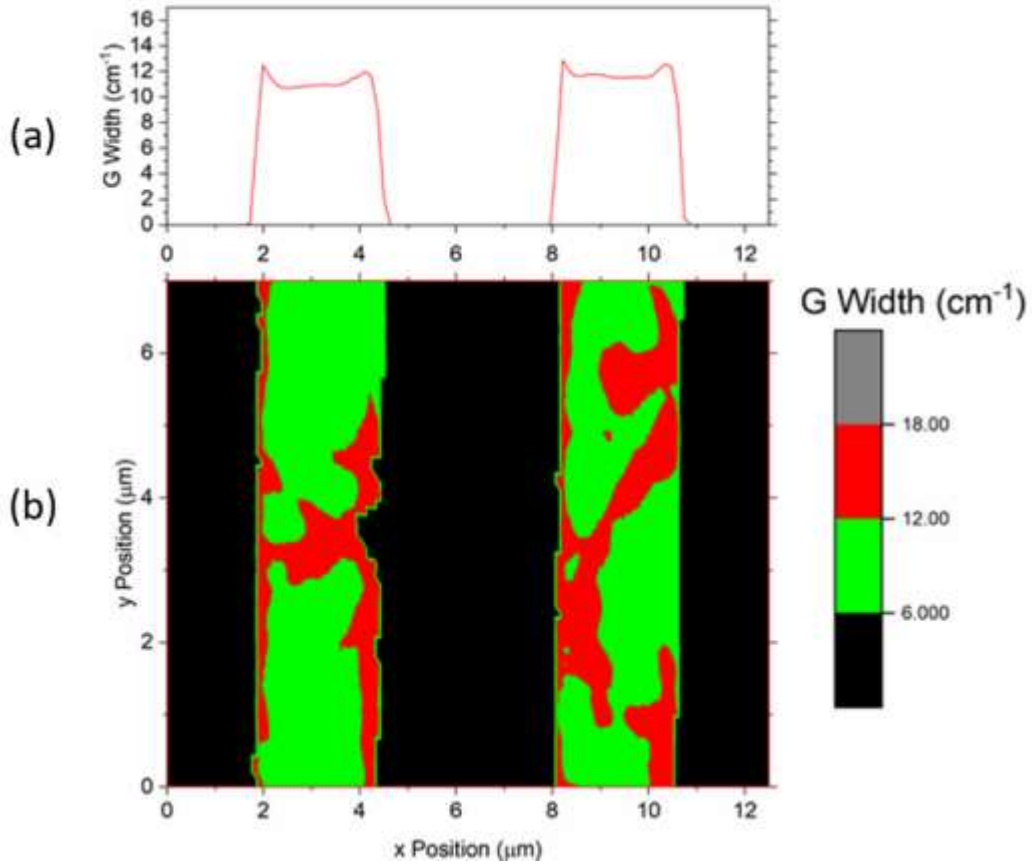

Figure 40: (a) Profile of the average of all data at each x position as an aid in visualizing (b), FWHM of Raman G peak in two graphene ribbons separated by SiO2/Si substrate.

The lateral spatial resolution of an optical microscope can be calculated by Equation (6)

$$\delta = 0.61 \cdot \frac{\lambda}{NA} \tag{6}$$

where δ is the diffraction limited spatial resolution, λ is the laser wavelength, and NA is the numerical aperture for the objective. With a λ=514nm and NA=0.85, the δ is approximately 369 nm. However, the value for Raman spectroscopy is typically quoted as

a few hundreds of nanometers to 1 μm due to scattering effects that are not accounted for in Equation (6).

Direct measurement using the SMM is shown in Figure 41. The half- and quarter-wavelength resonances were used to visualize the spatial maps. The magnitude of the complex reflection coefficient is plotted in Figure 41a (Figure 41c) and the phase angle is plotted in Figure 41b (Figure 41d) for the half- (quarter-) wavelength resonances respectively. The width of the EIL was measured using these images and the distribution is shown in Figure 41e. The EIL shows a lower conductivity than CVD-grown graphene and its width is estimated about 0.17 μm in this work.

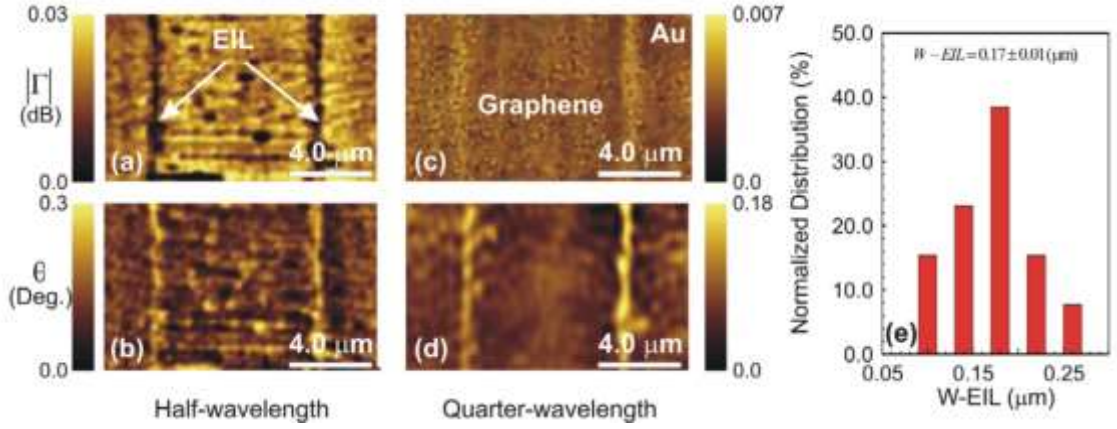

Figure 41: SMM images of reflection coefficient in half- (quarter-) wavelength resonances (a-d). Distribution of EIL width (e) [85].

5.3 Summary

Graphene etched using oxygen plasma was patterned in a grating structure. The edges of patterned graphene ribbons are known to have higher defect density than the bulk sheet, but a good measurement technique had not been developed. Raman

spectroscopy was used to determine the validity of a new measurement technique using SMM [85].

Even graphene covered by photoresist can be damaged through the side-wall of the photoresist by ultraviolet (UV) radiation. The photon energy of the oxygen plasma (9.5 eV) is sufficient to break the C-C bonds (4.9 eV), forming the EIL near the edges of the graphene pattern [87]. The reasons the resolution of Raman spectroscopy is limited are limits of the laser spot size and laser scattering at the surface of the material. This resolution is further reduced when the lifetimes of excitons, generated by photons, are sufficient to reach probed defect sites during the Raman process [63].

Alternatively, SMM allows very high spatial resolution compared to Raman spectroscopy. Since this EIL is measurable, it may be possible to optimize the processing to make use of the EIL, or mitigate its effects on sensing. More research is needed to determine the effects of the EIL on actual sensing properties.

6 Conclusions

The two-dimensional material, graphene, has been studied for its use in chemical vapor sensors. Since graphene requires an effective filter to allow certain species and block others from its surface, functionalization must be used. This paper proposes three methods for modification of the surface. The application of gold and platinum nanoparticles does show a change in material properties which may compete with the adsorption of ammonia. For this reason, the exact technique used does not show a promising outlook for the application of ammonia sensing. This is not to say that parts of this technique (namely the deposition technique) are not of potential use. Alternate methods may include pre-formed nanoparticles as-well-as optimized solutions to decrease possible contamination and to increase homogeneity.

High-temperature annealing ($T \geq 350°C$) may also be used to change the structure and capacitance of the graphene sheet. Changing the chemical structure may functionalize the graphene directly and/or act as a means to attach functional groups. This could be used as a method to make the manufactured graphene sensor more selective to specific gases. Additionally, based on the Raman data, one could argue that there is a de-doping process that occurs at high temperatures. These two processes may have different contributions at different temperatures resulting in the discrepancies in the Raman and electrical properties in this temperature range. Low-temperature annealing ($T < 350°C$) may act as a means to improve the sensitivity of the material or the detectable

concentration range. The doping observed at these lower temperatures is consistent with *p*-type doping, increasing the number of charge carriers. Ammonia acts as an electron donor which may more readily donate to a material with higher concentration of holes.

Raman spectroscopy is a very useful tool for the characterization graphene and has been used to track changes in the material during annealing and oxygen plasma etching. This technique helped verify the width of the EIL in graphene oxygen plasma-patterned nanoribbons along with SMM. These inactive layers show unique properties that may be tailorable for improved graphene sensor technology.

Future work of interest includes the implementation of sensing ammonia. This will allow a direct comparison for the sensing capabilities as related to the modification. Further research into decoration methods should be done to verify the results obtained and to eliminate the organic residue as a contributing factor to the electronic changes with respect to the gold and platinum deposition technique. Further work on the effects of annealing temperature on either or both of the following: the direct sensing capabilities of the device, the use of annealing to facilitate adhesion of functional groups to further modify the properties. The electrically inactive layer should be explored for the ability to be tailored to specific applications. If proper widths can be obtained by modifying process parameters, sensing capabilities can increase. Exploring the possible uses of the methods and techniques used to modify the graphene sheets may have significant contributions to the current sensing capabilities of graphene, allowing for a safer environment and improved monitoring for public health.

7 Bibliography

[1] I. Karaduman, E. Er, H. Çelikkan, N. Erk, and S. Acar, “Room-temperature ammonia gas sensor based on reduced graphene oxide nanocomposites decorated by Ag, Au and Pt nanoparticles,” *J. Alloys Compd.*, vol. 722, pp. 569–578, 2017.

[2] Y. Sun and K. Y. Ong, *Detection Technologies for Chemical Warfare Agents and Toxic Vapors*. Boca Ratan: CRC Press, 2005.

[3] B. Timmer, W. Olthuis, and A. Van Den Berg, “Ammonia sensors and their applications - A review,” *Sensors Actuators, B Chem.*, vol. 107, no. 2, pp. 666–677, 2005.

[4] D. J. Wilkinson, N. J. Smeeton, and P. W. Watt, “Ammonia metabolism, the brain and fatigue; Revisiting the link,” *Prog. Neurobiol.*, vol. 91, no. 3, pp. 200–219, 2010.

[5] S. M. Silva, J. D. Gamarra, C. A. Hernández, and J. F. Osma, “Design and fabrication of a sensor for explosives as a first step to an IED detection device,” *2014 IEEE 9th Iberoam. Congr. Sensors, IBERSENSOR 2014 - Conf. Proc.*, pp. 7–10, 2014.

[6] M. O’Hara, “Detection of IED Emplacements in Urban Environments,” Naval Postgraduate School, 2008.

[7] US EPA, “Chemical Advisory : Safe Storage, Handling, and Management of Ammonium Nitrate,” 2013.

[8] J. Romano, B. Lukey, and H. Salem, “Brief History and Use of Chemical Warfare Agents in Warfare and Terrorism,” in *Chemical Warfare Agents: Chemistry, Pharmacology, Toxicology, and Therapeutics*, Second., J. A. Romano Jr., B. J. Lukey, and H. Salem, Eds. Boca Raton, FL: CRC Press, 2008, pp. 1–20.

[9] F. Schmaltz, “Neurosciences and research on chemical weapons of mass destruction in Nazi Germany.,” *J. Hist. Neurosci.*, vol. 15, no. 3, pp. 186–209, 2006.

[10] A. L. Kikilo, Petr; Fedorenko, Vitaly; Ternay Jr., “Chemistry of Chemical Warfare Agents,” in *Chemical Warfare Agents: Chemistry, Pharmacology, Toxicology, and Therapeutics*, Second., J. A. Romano Jr., B. J. Lukey, and H. Salem, Eds. Boca Raton, FL: CRC Press, 2008, pp. 21–50.

[11] P. A. Dabisch, S. W. Hulet, R. Kristovich, and R. J. Mioduszewski, “Inhalatio toxicology of Nerve Agents,” in *Chemical Warfare Agents: Chemistry, Pharmacology, Toxicology, and Therapeutics*, 2nd ed., R. J. J. A., B. J. Lukey, and H. Salem, Eds. Boca Raton, FL: CRC Press, 2008, pp. 233–246.

[12] S. Gundavarapu, J. Zhuang, E. G. Barrett, F. Xu, R. G. Russell, and M. L. Sopori, “A critical role of acute bronchoconstriction in the mortality associated with high-dose sarin inhalation: Effects of epinephrine and oxygen therapies,” *Toxicol. Appl. Pharmacol.*, vol. 274, no. 2, pp. 200–208, 2014.

[13] Centers for Disease Control and Prevention, “Nerve Agent: SARIN,” *The Emergency Response Safety and Health Database*, 2013. [Online]. Available: http://www.cdc.gov/niosh/ershdb/EmergencyResponseCard_29750001.html. [Accessed: 02-Aug-2017].

[14] C. S. Gray, *Another Bloody Century: Furture Warfare*. Weidenfeld & Nicolson, 2005.

[15] D. E. Lenz, C. A. Broomfield, D. M. Maxwell, and D. M. Cerasoli, “Nerve Agent Bioscavengers: Protection against High- and Low-Dose Organophosphorus Exposure,” in *Chemical Warfare Agents: Toxicity at Low Levels*, S. M. Somani and J. A. Romano Jr., Eds. Boca Raton, FL: CRC Press, 2001, pp. 215–243.

[16] D. H. Moore and S. M. Alexander, “Emergency Response to a Chemical Warfare Agent Incident,” in *Chemical Warfare Agents: Toxicity at Low Levels*, S. M. Somani and J. A. Romano Jr., Eds. Boca Ratan: CRC Press, 2001, pp. 409–435.

[17] N. R. C. (US) C. on Toxicology, “Review of Acute Human-Toxicity Estimates for Selected Chemical-Warfare Agents,” *National Academies Press (US)*, 1997. [Online]. Available: https://www.ncbi.nlm.nih.gov/books/NBK233733/. [Accessed: 02-Aug-2017].

[18] B. R. Capacio, J. R. Smith, R. K. Gordon, J. R. Haigh, J. R. Barr, and B. J. Lukey, “Clinical Detection of Exposure to Chemical Warfare Agents,” in *Chemical Warfare Agents: Chemistry, Pharmacology, Toxicology, and Therapeutics*, 2nd ed., J. A. Romano Jr., B. J. Lukey, and H. Salem, Eds. Boca Raton, FL: CRC Press, 2008, pp. 501–548.

[19] E. Akbari, V. K. Arora, A. Enzevaee, M. T. Ahmadi, M. Saeidmanesh, M. Khaledian, H. Karimi, and R. Yusof, “An analytical approach to evaluate the performance of graphene and carbon nanotubes for NH_3 gas sensor applications,” *Beilstein J. Nanotechnol.*, vol. 5, no. May, pp. 726–734, 2014.

[20] V. Saxena and D. K. Aswal, “Conducting Polymers in Sensor Applications,” in *Organic Sensors: Materials and Applications*, E. Garcia-Breijo, B. Perez, and P. Cosseddu, Eds. Croydon: CPI Group, 2017, pp. 1–70.

[21] O. S. Kwon, S. J. Park, J. S. Lee, E. Park, T. Kim, H. W. Park, S. A. You, H. Yoon, and J. Jang, "Multidimensional conducting polymer nanotubes for ultrasensitive chemical nerve agent sensing," *Nano Lett.*, vol. 12, no. 6, pp. 2797–2802, 2012.

[22] C. O. Park and S. A. Akbar, "Ceramics for chemical sensing," *J. Mater. Sci.*, vol. 38, no. 23, pp. 4611–4637, 2003.

[23] J. S. Camino and R. B. Prats, "Organic Gas Sensors and Electronic Noses," in *Organic Sensors: Materials and Applications*, E. Garcia-Breijo, B. Perez, and P. Cosseddu, Eds. Croydon, 2017, pp. 219–255.

[24] J. Lee, Jun Seop; Shin, Dong Hoon; Jun, Jaemoon; Jang, "Multidimensional Polypyrrole / Iron Oxyhydroxide Hybrid Nanoparticles for Chemical Nerve Gas Agent Sensing Application," *ACS Nano*, vol. 7, no. 11, pp. 10139–10147, 2013.

[25] A. Peigney, C. Laurent, E. Flahaut, R. R. Bacsa, and A. Rousset, "Specific surface area of carbon nanotubes and bundles of carbon nanotubes," *Carbon N. Y.*, vol. 39, no. 4, pp. 507–514, 2001.

[26] A. H. Castro Neto, N. M. R. Peres, K. S. Novoselov, A. K. Geim, and F. Guinea, "The electronic properties of graphene," *Rev. Mod. Phys.*, vol. 81, no. 1, pp. 109–162, 2009.

[27] A. K. Geim and K. S. Novoselov, "The rise of graphene.," *Nat. Mater.*, pp. 183–191, 2007.

[28] B. Gharekhanlou and S. Khorasani, *Graphene: Properties Synthesis and Applications*. 2011.

[29] 1 A K Geim K. S. Novoselov 1* S. V. Morozov,2 D. Jiang,1 Y. Zhang,1 S. V. Dubonos,2 I. V. Grigorieva,1 A. A. Firsov2, "Electric Field Effect in Atomically Thin Carbon Films," *Science (80-.).*, vol. 306, no. October, pp. 666–670, 2004.

[30] F. Schedin, A. K. Geim, S. V. Morozov, E. W. Hill, P. Blake, M. I. Katsnelson, and K. S. Novoselov, "Detection of individual gas molecules adsorbed on graphene," *Nat. Mater.*, vol. 6, no. 9, pp. 652–655, 2007.

[31] S. Novikov, N. Lebedeva, and a Satrapinski, "Ultrasensitive NO 2 Gas Sensor Based on Epitaxial Graphene," *Ultrasensitive NO 2 Gas Sens. Based Ep. Graphene*, vol. 2015, p. 108581, 7 pages, 2015.

[32] W. Yuan and G. Shi, "Graphene-based gas sensors," *J. Mater. Chem. A*, vol. 1, no. 35, p. 10078, 2013.

[33] F. Perreault, A. Fonseca de Faria, and M. Elimelech, "Environmental applications of graphene-based nanomaterials," *Chem. Soc. Rev.*, vol. 44, no. 16, pp. 5861–5896, 2015.

[34] K. R. Nemade and S. A. Waghuley, “Chemiresistive gas sensing by few-layered graphene,” *J. Electron. Mater.*, vol. 42, no. 10, pp. 2857–2866, 2013.

[35] F. Yavari, E. Castillo, H. Gullapalli, P. M. Ajayan, and N. Koratkar, “High sensitivity detection of NO2 and NH3 in air using chemical vapor deposition grown graphene,” *Appl. Phys. Lett.*, vol. 100, no. 20, p. 203120, 2012.

[36] U. Latif and F. Dickert, “Graphene Hybrid Materials in Gas Sensing Applications,” *Sensors*, vol. 15, no. 12, pp. 30504–30524, 2015.

[37] G. Chen, T. M. Paronyan, and A. R. Harutyunyan, “Sub-ppt gas detection with pristine graphene,” *Appl. Phys. Lett.*, vol. 101, no. 5, 2012.

[38] G. Chen, T. M. Paronyan, and A. R. Harutyunyan, “Sub ppt gas detection with pristine graphene - Supplemental Material,” *Appl. Phys. Lett.*, vol. 101, no. 5, 2012.

[39] M. Gautam and A. H. Jayatissa, “Graphene based field effect transistor for the detection of ammonia,” vol. 064304, no. 2012, 2012.

[40] Y. Dan, Y. Lu, N. J. Kybert, Z. Luo, and A. T. C. Johnson, “Intrinsic response of graphene vapor sensors,” *Nano Lett.*, vol. 9, no. 4, pp. 1472–1475, 2009.

[41] J. H. Warner, “Chemical Properties of Graphene,” in *Graphene - Fundamentals and emergent applications*, Elsevier Inc., 2013, pp. 73–85.

[42] S. Alwarappan, S. Pillai, S. Singh, and A. Kumar, “Graphene-Based Biosensors and Gas Sensors,” in *Graphene Synthesis and Applications*, W. Choi and J. Lee, Eds. Boca Raton, FL: CRC Press, 2012, pp. 233–262.

[43] X. Li, Y. Wu, H. Song, S. Yoo, W. Liu, and X. Wang, “Controllable decoration of CVD-grown graphene with Au NP as a promising ammonia sensing platform,” *J. Mater. Sci. Mater. Electron.*, vol. 26, no. 3, pp. 1500–1506, 2015.

[44] M. Gautam and A. H. Jayatissa, “Ammonia gas sensing behavior of graphene surface decorated with gold nanoparticles,” *Solid. State. Electron.*, vol. 78, pp. 159–165, 2012.

[45] M. Gautam and A. H. Jayatissa, “Adsorption kinetics of ammonia sensing by graphene films decorated with platinum nanoparticles,” *J. Appl. Phys.*, vol. 111, no. 9, 2012.

[46] H. Sojoudi, J. Baltazar, C. Henderson, and S. Graham, “Impact of post-growth thermal annealing and environmental exposure on the unintentional doping of CVD graphene films,” *J. Vac. Sci. Technol. B, Nanotechnol. Microelectron. Mater. Process. Meas. Phenom.*, vol. 30, no. 4, p. 041213, 2012.

[47] Y. L. Shen, P. Zhou, L. H. Wang, Q. Q. Sun, Q. Q. Tao, P. F. Wang, S. J. Ding, and D. W. Zhang, "The Annealing Effect of Chemical Vapor Deposited Graphene," pp. 1–4, 2013.

[48] H. Y. Nan, Z. H. Ni, J. Wang, Z. Zafar, Z. X. Shi, and Y. Y. Wang, "The thermal stability of graphene in air investigated by Raman spectroscopy," *J. Raman Spectrosc.*, vol. 44, no. 7, pp. 1018–1021, 2013.

[49] L. Liu, S. Ryu, M. R. Tomasik, E. Stolyarova, N. Jung, M. S. Hybertsen, M. L. Steigerwald, L. E. Brus, and G. W. Flynn, "Graphene oxidation: Thickness-dependent etching and strong chemical doping," *Nano Lett.*, vol. 8, no. 7, pp. 1965–1970, 2008.

[50] J. H. Warner, F. Schäffel, A. Bachmatiuk, and M. H. Rümmeli, *Applications of Graphene*. 2013.

[51] National Institute of Standards and Technology, "The Hall Effect," 2010. [Online]. Available: https://www.nist.gov/pml/engineering-physics-division/popular-links/hall-effect/hall-effect.

[52] M. Integrated, "Impedance Matching and the Smith Chart: The Fundamentals," 2016. [Online]. Available: https://www.maximintegrated.com/en/app-notes/index.mvp/id/742. [Accessed: 04-Nov-2018].

[53] M. S. Amer, *Raman Spectroscopy, Fullerenes and Nanotechnology*. Cambridge: Royal Society of Chemistry, 2010.

[54] A. C. Ferrari, "Raman spectroscopy of graphene and graphite: Disorder, electron–phonon coupling, doping and nonadiabatic effects," *Solid State Commun.*, vol. 143, no. 1–2, pp. 47–57, Jul. 2007.

[55] I. Childres, L. Jauregui, W. Park, H. Cao, and Y. Chen, "Raman Spectroscopy of Graphene and Related Materials," *New Dev. Phot. Mater. Res.*, pp. 1–20, 2013.

[56] D. Graf, F. Molitor, K. Ensslin, C. Stampfer, a. Jungen, C. Hierold, and L. Wirtz, "Raman imaging of graphene," *Solid State Commun.*, vol. 143, no. 1–2, pp. 44–46, 2007.

[57] A. C. Ferrari and D. M. Basko, "Raman spectroscopy as a versatile tool for studying the properties of graphene," *Nat Nanotechnol*, vol. 8, no. 4, pp. 235–246, 2013.

[58] A. Eckmann, A. Felten, A. Mishchenko, L. Britnell, R. Krupke, K. S. Novoselov, and C. Casiraghi, "Probing the nature of defects in graphene by Raman spectroscopy," *Nano Lett.*, vol. 12, no. 8, pp. 3925–3930, 2012.

[59] L. M. Malard, M. A. Pimenta, G. Dresselhaus, and M. S. Dresselhaus, "Raman spectroscopy in graphene," *Phys. Rep.*, vol. 473, no. 5–6, pp. 51–87, 2009.

[60] D. Graf, F. Molitor, K. Ensslin, C. Stampfer, A. Jungen, C. Hierold, and L. Wirtz, "Spatially Resolved Raman Spectroscopy of Single- and Few-Layer Graphene," *Cond-mat*, p. 607562, 2006.

[61] N. Kharche, Y. Zhou, K. P. O. Brien, S. Kar, and S. K. Nayak, "Effect of Layer Stacking on the Electronic Structure of Graphene Nanoribbons," no. 8, pp. 6096–6101, 2011.

[62] M. Wall, "The Raman Spectroscopy of Graphene and the Determination of Layer Thickness," *Thermo Sci.*, p. 5, 2011.

[63] R. Beams, L. G. Cançado, and L. Novotny, "Raman characterization of defects and dopants in graphene," *J. Phys. Condens. Matter*, vol. 27, p. 083002, 2015.

[64] Z. Ni, Y. Wang, T. Yu, and Z. Shen, "Raman spectroscopy and imaging of graphene," *Nano Res.*, vol. 1, no. 4, pp. 273–291, 2008.

[65] A. C. Ferrari, J. C. Meyer, V. Scardaci, C. Casiraghi, M. Lazzeri, F. Mauri, S. Piscanec, D. Jiang, K. S. Novoselov, S. Roth, and A. K. Geim, "Raman Spectrum of Graphene and Graphene Layers," *Phys. Rev. Lett.*, vol. 97, no. 18, p. 187401, 2006.

[66] S. Suzuki, C. M. Orofeo, S. Wang, F. Maeda, M. Takamura, and H. Hibino, "Structural instability of transferred graphene grown by chemical vapor deposition against heating," *J. Phys. Chem. C*, vol. 117, no. 42, pp. 22123–22130, 2013.

[67] ETH Zurich, "SEM: Imaging with Secondary Electrons," 2018. [Online]. Available: http://www.microscopy.ethz.ch/se.htm. [Accessed: 27-Mar-2018].

[68] J. X. and J. P. Spallas, "Different Contrast Mechanisms in SEM Imaging of Graphene," *Agil. Technol.*, pp. 1–8, 2012.

[69] V. Kochat, A. Nath Pal, E. S. Sneha, A. Sampathkumar, A. Gairola, S. A. Shivashankar, S. Raghavan, and A. Ghosh, "High contrast imaging and thickness determination of graphene with in-column secondary electron microscopy," *J. Appl. Phys.*, vol. 110, no. 1, 2011.

[70] A. Nanakoudis, "How EDX analysis with a scanning electron microcope (SEM) works," 2017. [Online]. Available: http://blog.phenom-world.com/edx-analysis-scanning-electron-micrscope-sem. [Accessed: 04-Sep-2018].

[71] H. Komurasaki, T. Tsukamoto, K. Yamazaki, and T. Ogino, "Layered structures of interfacial water and their effects on raman spectra in graphene-on-sapphire systems," *J. Phys. Chem. C*, vol. 116, no. 18, pp. 10084–10089, 2012.

[72] Y. Ogawa, B. Hu, C. M. Orofeo, M. Tsuji, K. I. Ikeda, S. Mizuno, H. Hibino, and H. Ago, "Domain structure and boundary in single-layer graphene grown on Cu(111) and Cu(100) films," *J. Phys. Chem. Lett.*, vol. 3, no. 2, pp. 219–226, 2012.

[73] J. E. Lee, G. Ahn, J. Shim, Y. S. Lee, and S. Ryu, "Optical separation of mechanical strain from charge doping in graphene," *Nat. Commun.*, vol. 3, no. May, pp. 1024–1028, 2012.

[74] X. Qi, X. Guo, and C. Zheng, "Density functional study the interaction of oxygen molecule with defect sites of graphene," *Appl. Surf. Sci.*, vol. 259, pp. 195–200, 2012.

[75] T. Otsuji, T. Suemitsu, A. Satou, M. Suemitsu, E. Sano, M. Ryzhii, and V. Ryzhii, "Electronic and Photonic Applications for Ultrahigh-Frequency Graphene-Based Devices," in *Graphene Synthesis and Applications*, W. Choi and J. Lee, Eds. Boca Raton, FL: CRC Press, 2012, pp. 85–116.

[76] K. M. Milaninia, M. A. Baldo, A. Reina, and J. Kong, "All graphene electromechanical switch fabricated by chemical vapor deposition," *Appl. Phys. Lett.*, vol. 95, no. 18, p. 183105, 2009.

[77] C. Berger, Z. Song, X. Li, X. Wu, N. Brown, C. Naud, D. Mayou, T. Li, J. Hass, A. N. Marchenkov, E. H. Conrad, P. N. First, and W. A. De Heer, "Electronic confinement and coherence in patterned epitaxial graphene," *Science (80-.).*, vol. 312, no. 5777, pp. 1191–1196, 2006.

[78] D. Bischoff, A. Varlet, P. Simonet, M. Eich, H. C. Overweg, T. Ihn, and K. Ensslin, "Localized charge carriers in graphene nanodevices," *Appl. Phys. Rev.*, vol. 2, p. 031301, 2015.

[79] D. C. Abeysinghe, J. Myers, N. Nader Esfahani, J. R. Hendrickson, J. W. Cleary, D. E. Walker, K.-H. Chen, L.-C. Chen, and S. Mou, "Plasmonic resonance absorption spectra in mid-infrared in an array of graphene nanoresonators," *SPIE Photonics West 2014-OPTO Optoelectron. Devices Mater.*, vol. 8993, p. 89932B, 2014.

[80] C. Casiraghi, A. Hartschuh, H. Qian, S. Pliscanec, C. Georgia, A. Fasoli, K. S. Novoselov, D. M. Basko, and A. C. Ferrari, "Raman spectroscopy of graphene edges," *Nano Lett.*, vol. 9, no. 4, pp. 1433–1441, 2009.

[81] M. Y. Han, B. Özyilmaz, Y. Zhang, and P. Kim, "Energy band-gap engineering of graphene nanoribbons," *Phys. Rev. Lett.*, vol. 98, no. 20, 2007.

[82] A. Tselev, N. V. Lavrik, I. Vlassiouk, D. P. Briggs, M. Rutgers, R. Proksch, and S. V. Kalinin, "Near-field microwave scanning probe imaging of conductivity inhomogeneities in CVD graphene," *Nanotechnology*, vol. 23, no. 38, 2012.

[83] J. Myers, T. Nicodemus, Y. Zhuang, T. Watanabe, N. Matsushita, and M. Yamaguchi, “Characterization of grain boundary conductivity of spin-sprayed ferrites using scanning microwave microscope,” *J. Appl. Phys.*, vol. 115, no. 17, p. 17A506, 2014.

[84] J. Myers, S. Mou, K.-H. Chen, and Y. Zhuang, “Scanning microwave microscope imaging of micro-patterned monolayer graphene grown by chemical vapor deposition,” *Appl. Phys. Lett.*, vol. 108, no. 5, p. 053101, 2016.

[85] K. Brockdorf, Z. Ji, N. Engel, J. Myers, S. Mou, H. Huang, and Y. Zhuang, “Imaging of edge inactive layer in micro-patterned graphene monolayer,” *Mater. Lett.*, vol. 211, pp. 183–186, 2018.

[86] M. M. Lucchese, F. Stavale, E. H. M. Ferreira, C. Vilani, M. V. O. Moutinho, R. B. Capaz, C. A. Achete, and A. Jorio, “Quantifying ion-induced defects and Raman relaxation length in graphene,” *Carbon N. Y.*, vol. 48, no. 5, pp. 1592–1597, 2010.

[87] C. H. Huang, C. Y. Su, T. Okada, L. J. Li, K. I. Ho, P. W. Li, I. H. Chen, C. Chou, C. S. Lai, and S. Samukawa, “Ultra-low-edge-defect graphene nanoribbons patterned by neutral beam,” *Carbon N. Y.*, vol. 61, pp. 229–235, 2013.

8 Appendix A

8.1 Response vs. Time Plot

Most vapor sensing experiments show a plot of response vs. time where response is the change in the detectable variable divided by the unexposed value. There is generally a short period of time used to determine the baseline, after which the exposure begins. Once the response has started to stabilize (at about 90% of the saturation point), the gas is turned off and a recovery period begins. Some plots will include exposures at different concentrations to determine the lowest detectable concentration. These plots are used to define the response time, recovery time, and sensitivity. Some plots will include exposures at different concentrations to determine the lowest detectable concentration. One such plot is shown in Figure 42 where the first regime (I) is the non-exposed time, (II) is the exposure to designated gas, (III) is post exposure which shows almost no recovery, and (IV) is the sample under a 150°C forced recovery.

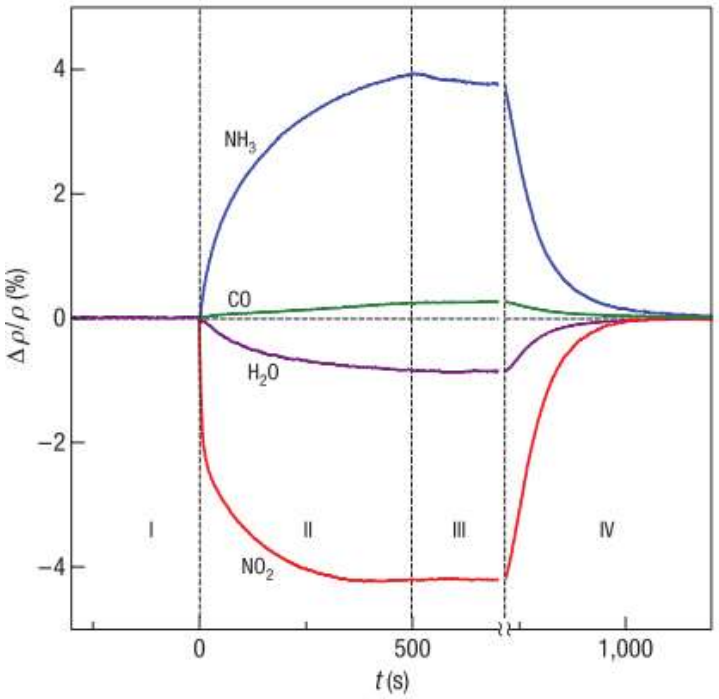

Figure 42: Schematic of Response vs. time plot [20]

9 Appendix B

9.1 PtNP Coverage Calculations

A secondary electron SEM image was obtained from the highest concentration PtNP decoration of graphene (Figure 43.) Using built-in MATLAB functions, the image was segmented with a threshold intensity value >105 (with 255 being pure white and 0 being black in a grayscale colormap) to show the highest intensity regions after a noise removal algorithm (*imgaussfilt* using default settings.) MATLAB's *bwconncomp* function was used to index each feature over 5 pixels large (<5 pixels was interpreted as residual noise) shown in Figure 44 after which, *regionprops* was used to find the major/minor axis length (of equivalent ellipse), equivalent diameter (diameter of circle with same area as the feature) and centroid of each feature. The major and minor axis were averaged to obtain the average diameter of the features (PtNPs) and are plotted in Figure 45. The equivalent diameter distribution of PtNP is also given in Figure 46. Coverage was calculated by the sum of feature area over image area (i.e. sum of true pixels in Figure 44 divided by the total number of pixels.) With the assumption of circular profiles, the mode diameter is between 3-5 nm for the PtNPs.

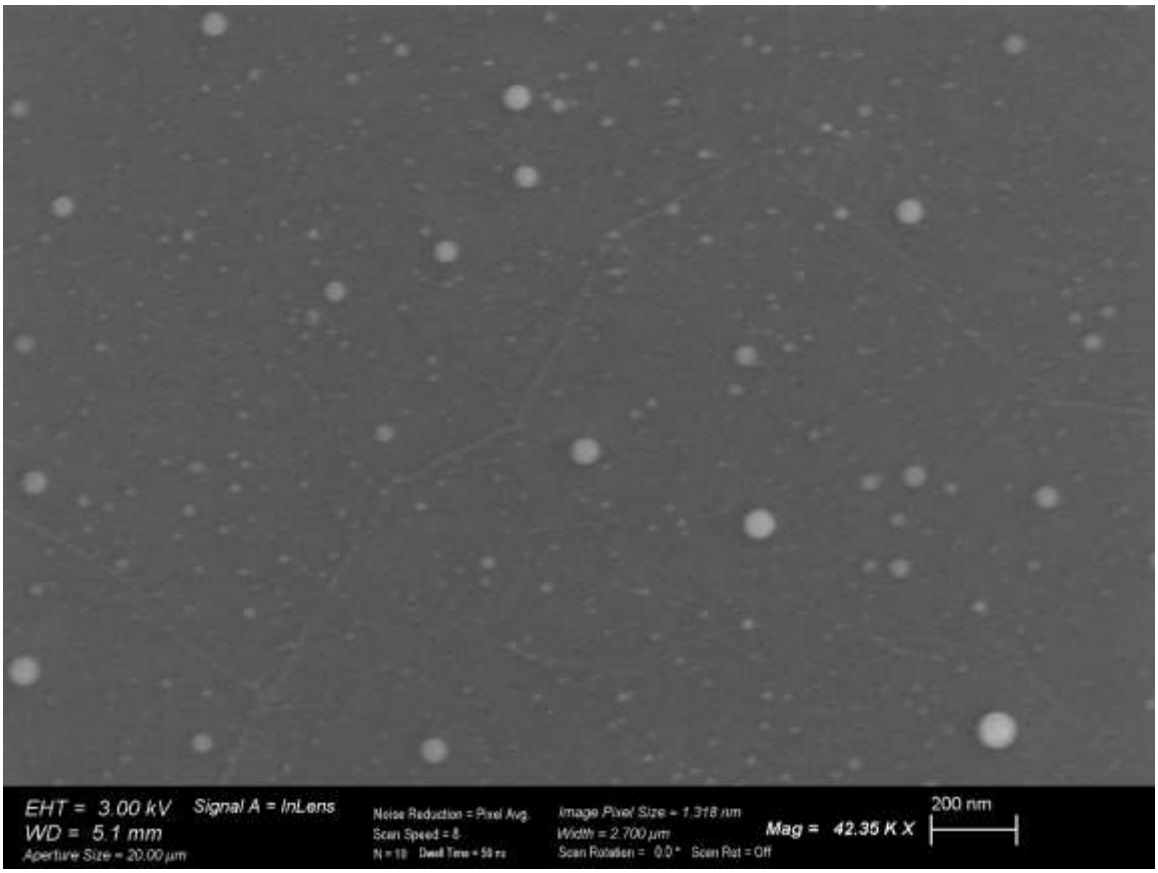

Figure 43: Representative PtNP (highest concentration) on graphene image.

Figure 44: Image from Figure 43 with applied filters

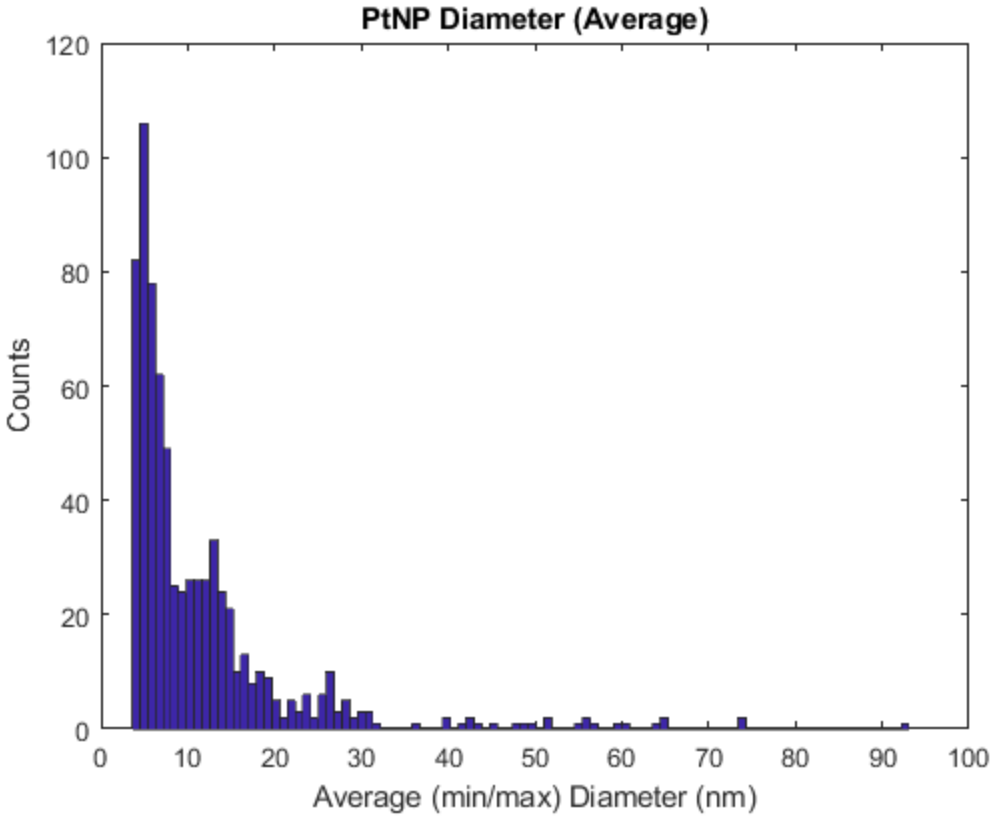

Figure 45: Size distribution of PtNP on graphene (max concentration) based on Figure 43 using average diameter of objects in Figure 44

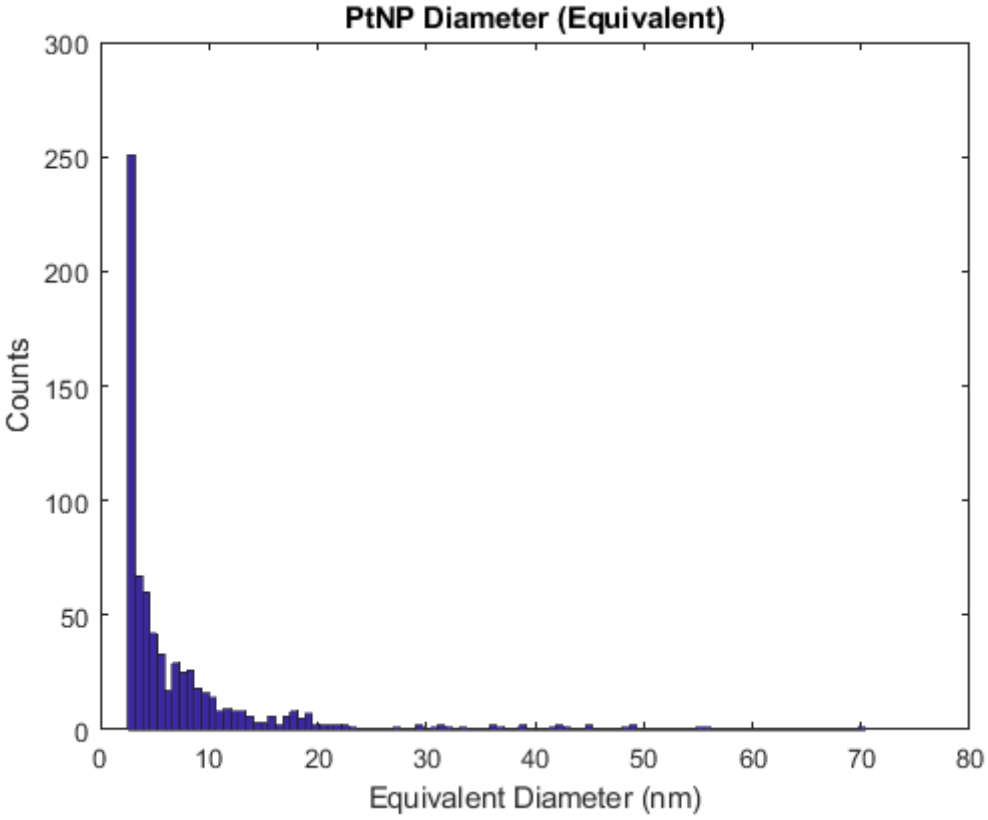

Figure 46: Size distribution of PtNP on graphene (max concentration) based on Figure 43 using equivalent diameter of objects in Figure 44

9.2 EDS spectra from Figure 22

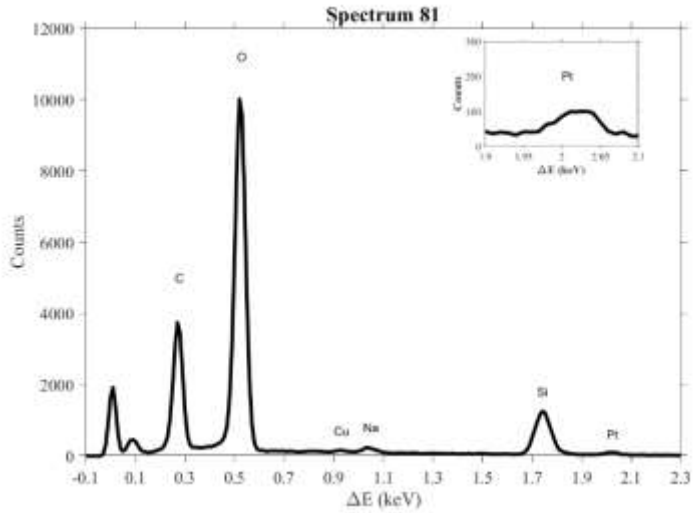

Figure 47: EDS Spectrum 81 from Figure 22

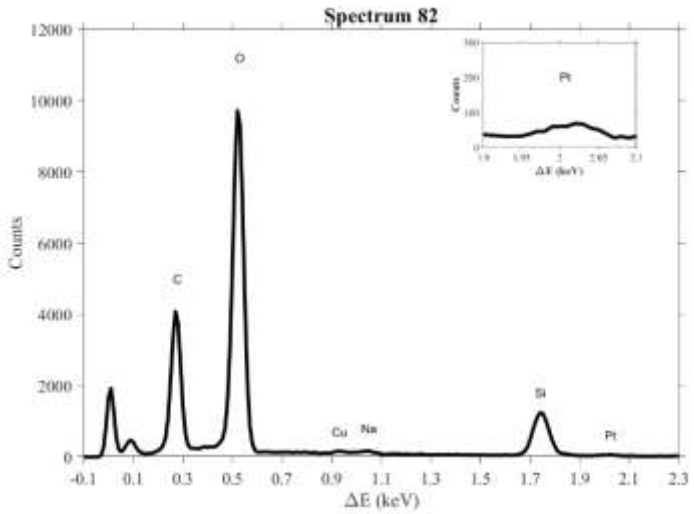

Figure 48: EDS Spectrum 82 from Figure 22

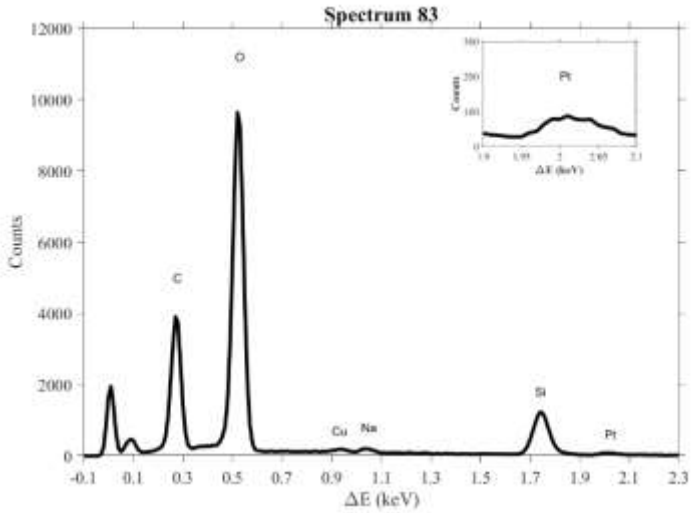

Figure 49: EDS Spectrum 83 from Figure 22